Seismic prediction and imaging of geological structures ahead of a tunnel using surface waves

Zur Erlangung des akademischen Grades eines
DOKTORS DER NATURWISSENSCHAFTEN
von der Fakultät Physik des
Karlsruher Instituts für Technologie (KIT)

genehmigte

DISSERTATION

von

Dipl.-Geophys. Stefan Jetschny
aus Dresden

Tag der mündlichen Prüfung:	30.April 2010
Referent:	Prof. Dr. Thomas Bohlen
Korreferent:	Prof. Dr. Wolfgang Rabbel

"…time takes too much time…"
Rósín Marie Murphy (1973 -)

für
Jörg “diddie” Dietrich
“Gruß und Frieden”

Abstract

To increase safety and efficiency of tunnel constructions, online seismic exploration ahead of a tunnel can become a valuable tool. By correlating predicted geological structures, such as weak or water bearing zones and lithological interfaces, with the known geological situation, the tunneling process can be optimized. Time consuming and thus expensive downtime can be avoided and the construction site as well as the surface is less exposed to safety threads. This is especially important for the tunneling in urban areas, which mainly involves the utilization of tunnel construction machines (TBMs) below the water table.

We developed a new forward looking seismic imaging technique that implies less interference with the mechanical tunneling. Our approach is based on the excitation and registration of tunnel surface waves (TS-waves). These waves are excited at the tunnel wall behind the cutter head of a TBM and travel into drilling direction. When arriving at the front face, they generate body waves (mainly S-waves) propagating further ahead. Reflected S-waves are back-converted into tunnel surface waves ("TSST"-waves) and can be recorded by geophones mounted on the tunnel wall. Using 3-D Finite Difference modeling, an analytical solution of the wave equation in cylindrical coordinates and field data acquired at tunneling sites, we investigated the propagation characteristics of tunnel surface waves in terms of dispersion and polarization. It could be shown that at higher frequencies, i.e., if the tunnel-diameter is significantly larger than the wavelength of surface waves, these surface waves can be regarded as Rayleigh-waves confined to the tunnel wall and following helical paths along the tunnel surface. For lower frequencies, i.e., when the tunnel surface wavelength approaches the tunnel diameter, the propagation characteristics of these surface waves are similar to S-waves. Understanding the excitation and propagation of TS-waves is the key for developing processing and imaging techniques for our seismic look ahead prediction in tunnel constructions.

Synthetic case studies have been used to investigate single propagation effects that occur under tunneling conditions. For example, both the excavation damage zone and the lining of the tunnel wall significantly alters the dispersion characteristics of TS-waves. Furthermore, the excitation and propagation of tunnel surface wave for the seismic look-ahead prediction in soft rock and hard rock formations depends on the constraint of the resulting TS-wave wavelength with respect to the tunnel diameter. At the same time, these studies have been used to identify modeling strategies and limitations of various finite difference modeling codes as well as semi-analytical solutions. Depending on the given problem, we can reduce the dimensionality of the model and thus neglect certain wave propagation phenomena (e.g., 3-D geometrical spreading and tunnel related dispersion) in order save computational time.

On the basis of a complex tunnel model that accounts for a typical tunneling survey through hard rock, we created a comprehensive synthetic tunnel seismic data set. Only a subset of this data has been used to develop a processing scheme to predict the position of a reflector ahead of the tunnel, which can be a dipping plane interface with a significant impedance contrast or a smaller scale inclusion. The sequence of common seismic processing steps can operate automatically and without any a priori information. This way, we can estimate the distance between tunnel face and a geological structure ahead, being a first step toward a reliable and automatic seismic imaging in the underground. The applicability of the prediction method has been successfully tested on field data acquired at the Gotthard base tunnel, Switzerland, and during the construction of the “Neuer Schlüchterner” railroad tunnel close to Fulda, Germany. In case of reflection signals present in recorded seismogram sections and due to a litholocical interface, theses arrivals could be isolated and interpreted to reconstruct the distance to the reflector. The results are confirmed by geological mapping and exploratory drilling, respectively.

Contents

List of Tables

List of Figures

List of Symbols and Abbreviations

A_ϕ, A_r, A_x	peak amplitude regarding the ϕ, r and x coordinate axis
CRG	common-receiver gather, measurement layout that uses one receiver and generally multiple shot positions
CSG	common-source gather, measurement layout that uses one shot and generally multiple receiver positions
d	diameter and tunnel diameter, respectively
dt	time difference between the update of elastic parameters, time step length
dh	distance between two neighboring grid points, grid spacing
f	frequency
f_c	source center frequency
FD	finite difference, usually the finite difference time domain (FDTD) method is referred
FDTD	finite difference time domain
n	source orders (e.g., monopole, dipole) and order of the Hankel function, respectively
P-wave	compressional wave, primary wave
Q	quality factor, measure for the seismic wave attenuation
r	radius and tunnel radius, respectively
S-wave	shear wave, secondary wave
t, T	time
TBM	tunnel boring machine
TS-wave	tunnel surface wave
TSST-wave	wave reflected from formation heterogeneities, named according to its wavepath as a TS-wave, converted S-wave, reflected S-wave as well as a back-converted TS-wave
u	displacement
v_a	apparent TSST-wave velocity
v_p	compressional wave velocity
v_r	Rayleigh surface wave velocity
v_red	reduction velocity, i.e., seismogram traces are shifted by a time delay of $\frac{s}{v_\mathrm{red}}$ where s is the distance to the source
v_s	shear wave velocity
v_ts	tunnel surface wave velocity
v_x, v_y, v_z	particle velocity regarding the x, y and z coordinate axis

w	. . . wavelength-to-tunnel-diameter ratio
w_{e}	. . . wavelength-to-earth-diameter ratio
x, y, z	. . . coordinates of the Cartesian reference system
λ	. . . wavelength
ν	. . . Poisson's ratio, $\nu = \frac{1}{2} \cdot \frac{v_{\mathrm{p}}^2 - 2v_{\mathrm{s}}^2}{v_{\mathrm{p}}^2 - v_2^2}$
ρ	. . . bulk density
ϕ, r, x	. . . coordinates of the cylindrical reference system
φ	. . . inclination angle (dip) of a geological structure with respect to the tunnel axis

CHAPTER I

Introduction

Infrastructure projects worldwide often face the same demands of creating short cuts in order to keep up with the increase in public traffic and transportation. Especially in urban areas the widening or adding of roads is no longer an option. One feasible solution is to go underground. At traffic junctions limited by the landscape, e.g., by rivers, sounds or mountains, building tunnels is sometimes the only approach to create faster and safer pathways. With the increasing number and dimensions of such tunneling projects, the use of tunnel boring machines (TBMs) becomes more prevalent. Tunnel boring machines have the potential for automated and continuous drilling of tunnels with low employment of workers at high performance. Even though tunnel boring machines can drill tunnels through almost any kind of rock formation, a TBM is usually custom designed for a specific tunnel construction project in terms of encountered geology and tunnel diameter. The geologic situation along the tunnel trajectory is less predictable in urban areas due to the limited access for geological probing and geophysical measurements. Surveying construction sites for the tunneling of mountains and sounds is possible, but field campaigns of any kind are expensive and often lack the necessary vertical resolution to safely predict the geological situation. This can results in uncertainties regarding the actual rock type and the spatial location of structures encountered during the tunnel construction. Sudden changes in the geological and geotechnical properties, i.e., at lithological boundaries, fracture zones or ground water bearing soil can be a serious safety threat to the TBM and usually requires specially designed TBMs. Safely predicting geological structures ahead of the tunnel construction can therefore significantly reduce safety risks and prevent expensive down times of the tunnel boring machine.

1.1. Tunnel constructions basics

Since the dawn of civilization, people have been building tunnels to access ores, underground quarries or tombs. Starting with the industrial revolution in the 18th century, a huge demand for the exploitation of resources arose. Wood, coal and ores, etc., had to be transported from remote regions to urban areas for further use and processing. Where bridges span rivers and valleys, tunnels had to be constructed under hills or mountains. The mining knowledge gained through hundreds of years could be utilized for such infrastructural projects. Nowadays, demands of public traffic in urban areas and creating fast pathways for transportation becomes the driving force for building tunnels. Also, tunneling sometimes substitutes for bridge construction due to esthetic reasons (www.welterbe-erhalten.de, 2009), limitations on high-clearance water ways or real estate prices on each shore.

All host rock formations encountered during the tunneling can be summarized by one single measure of paramount importance: the stand-up time, which is the time period the ground will safely stand by itself at the point of excavation. Stand-up time in sediment environments like clay, silt, sand, gravel or mud, e.g., is usually low (hours, days). Cave-ins are consequently a constant threat to the tunnel and necessitates a shielding, casing or tubing to stabilize the tunnel. In the tunneling business, sediment rocks are therefore commonly addressed as *soft rocks*. In contrast, stand-up time of tunnels in metamorphic or igneous rocks can measure in centuries. If these so called *hard rocks* are fractured or disturbed in any way, further support of the tunnel wall is necessary, e.g., by bolts, sprayed concrete (shotcrete), steel beams or permanent concrete rings (Harris, 2009).

Active support of the tunnel wall is a development from the last century. Before that, tunnels could mostly be drilled through hard rock only. Commonly this has been performed using explosives or other equipment (hammers, diggers, roadheading machines, etc.) that partially loosen the rock. These methods are termed *conventional tunneling* and do not necessarily excavate the full cross section of the tunnel at the same time. Tunnel boring machines overcome these limitations of flexible use in hard and soft rock and the full excavation of the tunnel diameter. A brief comparison of both pros and cons of conventional and TBM tunneling is provided by Table 1.1. Conventional tunneling with the focus of drilling and blasting and mechanical tunneling using a tunnel boring machine is described in more detail in the following chapters.

	conventional tunneling	**TBM tunneling**
advantages	• variable tunnel cross section • equipment are universally usable • easy replacement of failing equipment • low costs prior to the construction • variable response to fracture zones	• handling of difficult geological situation • high level of safety due to support of the tunnel face • high accuracy of the tunnel diameter • high performance of tunneling (up to 8 $\frac{(m)}{(day)}$ in hard rocks, up to 20 $\frac{m}{day}$ in soft rocks) • low lining effort after the tunneling • low construction costs during long tunneling
disadvantages	• low safety at work close to the tunnel face • tunneling progress is limited to about 5 $\frac{m}{day}$ • tunneling in soft rock is almost impossible • scaling of the tunnel wall required • intensive effort in lining	• fixed circular cross section • high costs prior to the tunneling • TBM is custom designed for single tunnel diameter and encountered geology • high training efforts of staff • damage to the TBM results in total stands of construction • elaborate maintenance stops • limited accessibility of the tunnel face

Table 1.1.: Pros and cons of TBM and conventional tunneling

1.2. Conventional tunneling

Conventional tunneling, also commonly known as drilling and blasting, is by far the oldest method of tunneling still in use and a subject to ongoing improvements. Based on the crushing of the host rock using explosive charges in boreholes, basically five sequencing steps can be subdivided (Figure 1.1): drilling, loading, blasting, ventilating and hauling. First, the boreholes are drilled by a so called jumbo, which is a mounted platform for carrying one or more drilling carriages (Figure 1.2). One or more boreholes with a diameter of up to 52 mm can be drilled simultaneously and are placed according to a specific pattern (Figure 1.3). Boreholes placed in the center of the tunnel face are usually utilized for decreasing the host rock tension and creating a targeted spot for the soil to collapse into. Radial distributed boreholes crush the rock across the tunnel face (Girmscheid, 2000). The closer the boreholes are placed to each other, the less explosive charges are needed in order to gain a constructive superposition of the explosive effects. Less explosives are therefore needed and the size of the debris can be controlled more effectively. Also, the borehole diameter itself affects the tunneling process. Blastings of larger holes can effectively improve the cutting, fewer explosives are required and shocks are reduced at the same time. However, drilling in general and drilling of larger boreholes is expensive. Even though the theoretical drilling performance is about 300 $\frac{\mathrm{m}}{\mathrm{h}}$ in hard rock (Bösch, 1998) more boreholes imply longer drilling time. This is due to the number of wells or the increased diameter, which consequently reduce the overall tunneling performance (Hustrulid, 1999). After the drilling is complete, the boreholes are loaded with explosive charges. In order to optimize the explosive effects and reduce the use of explosives, the boreholes are not necessarily completely filled with explosives like gelatinous explosives, ANC explosives or emulsion explosives (Bösch, 1998). With respect to the properties of the surrounding host rock and the spatial location of the borehole, the amount and the position of the employed explosive charges can vary. Ring trimmer shot holes (Figure 1.3) for leveling the contour of the tunnel, for example, usually employ less but continuously distributed explosives, while the center shots are heavily loaded at discrete positions. In modern conventional tunneling, the explosive charges are ignited by electrical detonators, which enable up to 54 time stages. By controlling the exact detonation time, the optimal explosive effect is gained, which ideally results in a smoother tunnel wall and well crushed debris (required for proper hauling). Because of dust and explosive fumes from the blasting, the debris and the working front are inaccessible for a certain time. After ventilation of the fumes the loosened rock can be hauled using mining excavators and conveyor belts (Figure 1.2).

Historically, tunneling using roadheading machines (Figure 1.4) is addressed as conventional tunneling, too. Roadheaders are mounted platforms carrying a huge drill bit, which is highly mobile and can partially carve the tunnel at the tunnel face. Due to its low performance but reasonable construction costs, these machines are usually employed to carve cavities and shorter tunnels like cross tunnels.

In general, conventional tunneling is a safe, reliable and well researched method of tunnel construction. Still, there are certain disadvantages (see Table 1.1). First, due to the blasting the contour of the tunnel is quite rough and needs further effort in lining. Among others, break outs have to be compensated and remaining overhangs have to be removed. Second, even though continuous improvements have been introduced (Bösch, 1998), the overall tunneling performance of up to 5 $\frac{m}{day}$ is still below the performance of up to 8 $\frac{m}{day}$ of mechanical tunneling, e.g., using a tunnel boring machine (Kolymbas, 1998). Third, the tunneling in urban areas

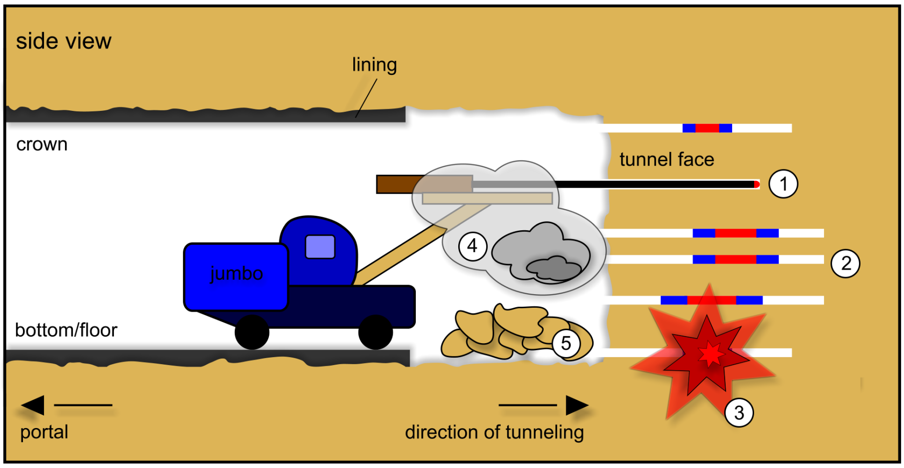

Figure 1.1.: Conventional tunneling scheme: 1) drilling of boreholes, 2) loading the boreholes with explosives, 3) blasting, 4) ventilating fumes, 5) hauling and removing of debris.

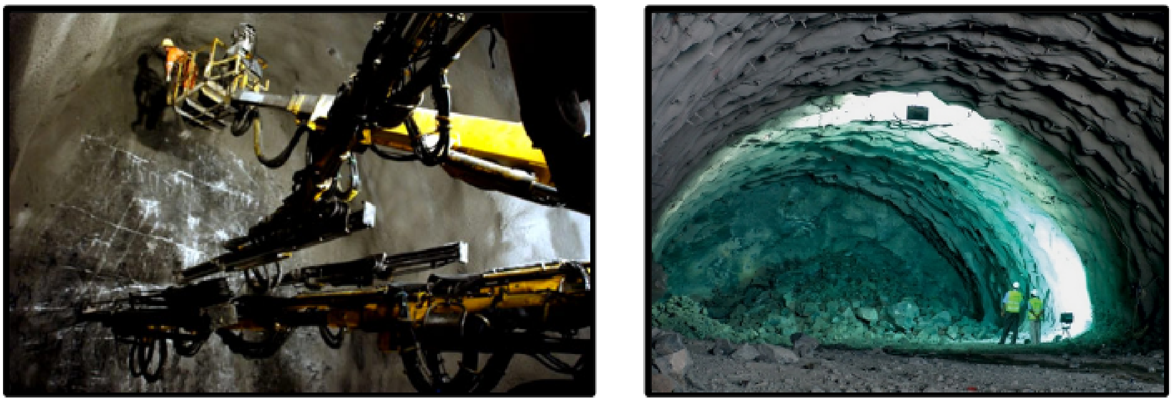

Figure 1.2.: Conventional tunneling: drilling of the boreholes (left image, taken from www.bls.ch, 2009) and rock debris in front of the tunnel face after blasting (right image, taken from Rogers, 2009).

prohibits the general use of explosive charges as the emitted shocks can cause damage to buildings at the surface. Also, as the tunnel construction process consists of different steps, a variety of highly specialized machines and operators are needed. Furthermore, conventional tunneling is limited to hard rock formations because no active support of the tunnel face can be provided, and drilling and blasting within clay or silt is naturally less effective. However, conventional tunneling is superior when constructing reasonably short tunnels due to its low costs. More detailed information on conventional tunnel construction is provided by Kolymbas (1998), Girmscheid (2000) or Singh and Goel (2006).

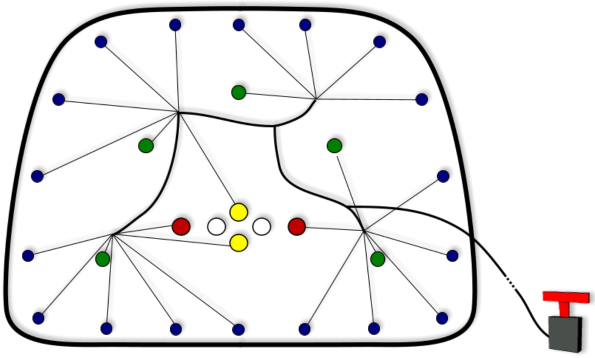

Figure 1.3.: Schematic drilling pattern at the tunnel face. Drilling locations are marked by circles and color coded with respect to the detonation stages: 1. yellow, 2. red, 3. green, 4. blue. Center shots (yellow, red, green circles) contain more explosive charges than ring trimmer shots (blue circles). Unloaded boreholes (white circles) can be used to decrease the formation tension. The explosive charges are wired electrically or by detonation fuses.

Figure 1.4.: Roadheading machine inside and outside a tunnel construction site (taken from www.pitsch.ch, 2009).

1.3. Mechanical tunneling

In contrast to conventional tunneling, mechanical tunneling utilizes machines that can - in theory - continuously drill a tunnel. That is why, mechanical tunneling is often addressed as automated tunneling, too. Tunnel boring machines are huge machines with gigantic proportions (see Figure 1.5). They can measure more than hundred meters in length, fill out the whole tunnel and can weigh more than 400 t. The world's largest TBM has an effective excavation diameter of more than 15 m (Herrenknecht EPB Shield S-300 used in the M-30 Madrid project). Since TBMs bear a giant drill bit (cutting wheel) at the front, they can excavate the entire tunnel diameter at the same time (full face method). With additional support of the tunnel face in soft rock environments, TBMs are not limited to specific host rock formations. With its flexibility regarding the geological situation, the ability of more or less continuous tunneling and its low disturbance of the host rock, i.e., less shocks emitted to the surrounding

Figure 1.5.: Hard rock tunnel boring machine (TBM) at the Herrenknecht AG headquarter, Schwanau, Germany: 13.3 m diameter TBM build for tunneling the Brenner railroad track Munich - Verona (left picture), detailed view on the TBM cutting wheel (right picture).

soil, tunneling using TBMs became the first choice in urban tunneling and tunneling in mixed geological situations. Besides, only a few workers are necessary to operate the machine. On the other side, a tunnel boring machine is a very expensive device, and since it is custom designed with respect to the purpose of the tunnel and encountered geology, a TBM is basically a one way product only.

In general, tunnel boring machines (TBMs) consist of two major sections. Together with the cutting wheel, the excavation chamber and the drivetrain, the first section both excavates and removes the soil and - if necessary - stabilizes the tunnel face. The backup train as a second section is located inside the finished part of the tunnel and carries all the supporting mechanisms, e.g., pumps, generators, control rooms, dirt removal or lining devices (Figure 1.6). With respect to the condition of the surrounding rock, there are several types of TBMs differing in their basic locomotion, support of the tunnel face and their dirt removal. In hard rock formations, reliable cracking, crushing and removing of the ground is a major issue. In contrast, stabilizing the tunnel and the tunnel face is more important under soft and unstable rock conditions. In the following, a brief overview of different TBM types is given. An additional list providing single facts and examples of tunnel constructions using different type of TBMs can be found in Table 1.2.

Igneous or metamorphic rocks (commonly addressed as hard rocks) usually handle and distribute the main load around a tunnel. The stand-up time of the tunnel can measure in decades or even centuries. Therefore, less effort has to be invested to stabilize the tunnel wall. The drivetrain of a *Gripper TBM*, a typical hard rock TBM, is braced against the tunnel wall by extendable gripper shoes and utilizes actuators (hydraulic cylinders) to push the cutting wheel against the tunnel face. Cutter rings (disks) mounted on the cutter head roll over the tunnel face under high pressure and loosen the native rock. The excavated rock (chips) are collected in openings in the cutterhead and removed by hoppers onto a conveyor belt. The finished tunnel is finally lined by rock anchors, meshes and shotcrete or precasted lining segments (Herrenknecht, 2003a; Girmscheid and Schexnayder, 2003).

In case of a less stable rock environment or disturbed sections along the tunnel trajectory, the tunnel wall needs to be protected from collapsing. Hence, the drivetrain is equipped with a large metal cylinder (shield) sealing the TBM from the surrounding ground and stabilizing the formation until tubing segments can be installed along the tunnel wall. Since the rock is not stable enough to sustain the pressure of the gripper shoes, so called *shield TBMs* move forward by extending hydraulic cylinders supported on the tunnel lining ring (see Figure 1.6). The excavating and removing of the soil is similar to that of a gripper TBM. If the actuators are extended to a maximum, the tunnel construction then halts for the installation of a new ring of lining segments. Tunneling using a single shield TBM is consequently called *discontinuous tunneling*. Next, the hydraulic cylinders are contracted and a pivotable erector picks up the tubing segments (precasted steel reinforced concrete elements) and places them along the tunnel wall. Afterwards, the actuators are extended again onto the newly constructed ring and continue pushing the drivetrain and the cutting wheel against the tunnel face. The remaining gap between lining and formation is filled with mortar. Double shield TBMs combine the concepts of both gripper shoes and hydraulic cylinders supported on the tubing segments and are therefore much more expensive but enable a virtually continuous tunnel construction in mostly stable rock environments encountering weaker fault zones.

Tunneling in soft and unstable sediments (commonly addressed as soft rocks) especially below the water table needs far more stabilization effort. Not only the roof of the tunnel but also the tunnel face requires active support. In addition to a shield, the formation pressure at the tunnel face is balanced by the excavated soil or by a secondary medium like air or a bentonite suspension. Shielded TBMs can be thus classified as *earth pressure balance TBMs* (EPB TBMs, Herrenknecht (2003b)) and *slurry TBMs* (Herrenknecht, 2003c). The excavation chamber of both TBM types is separated from the drivetrain by a pressure bulkhead. By the continuous supply of excavated soil, the material within the excavation chamber of an EPB TBM is compacted up to an equilibrium with the formation pressure at the tunnel face. The pressure within the chamber is controlled by the removal of soil through a screw conveyor. In contrast, the excavation chamber of a slurry TBM is filled with a bentonite suspension. After being loosened by the cutter head, the soil mix with the suspension fluid and can be later separated by filtering units located at the backup train. The support pressure is regulated by the suspension feeding circuit, i.e., the inflow and outflow of the suspension fluid through slurry pipes. For an indirect but more reliable control of suspension pressure and thus the tunnel face, a compressible air cushion in a separate pressure chamber next to the excavation chamber can be used. This way, pressure fluctuations due to irregularities in the suspension circuit can be compensated.

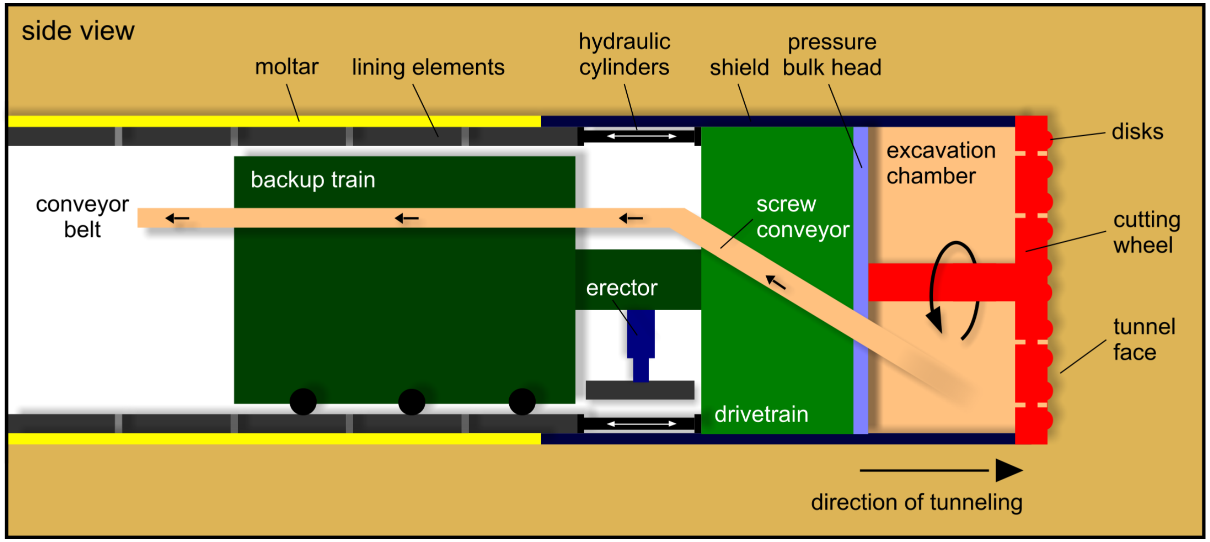

Figure 1.6.: General sketch of a single shield TBM.

TBM type	**ground condition**	**face control**	**lining**	**tunneling examples**
EPB	soft rock, wet, unstable	compressed excavated soil in excavation chamber	precasted lining segments (reinforced concrete tube segments)	Channel tunnel; most Metro tunnels (London, Barcelona, Los Angeles, Singapore); Katzenbergtunnel, Germany
Slurry	soft rock, wet, unstable, mixed geological conditions	bentonite suspension in excavation chamber	precasted lining segments	4th Elbe tunnel, Hambug; Cairo Metro; main railway station tunnel, Berlin; city tunnel, Leipzig
Single shield	soft rock, brittle, less stable geological conditions	no closed system for tunnel face pressure compensation	precasted lining segments	Adler railway tunnel, Switzerland; Perschling railway tunnel, Austria; Dublin port tunnel
Double shield	disturbed hard rock, unstable sections, chances of fault zones	no closed system for tunnel face pressure compensation	rock anchors, meshes and shotcrete, precasted lining segments	Brisbane North-South bypass tunnel, Guadarrama tunnel, Spain
Gripper	hard rock, low water ingress	no closed system for tunnel face pressure compensation	rock anchors, meshes and shotcrete, precasted lining segments	Gotthard base tunnel, Switzerland; Lötschberg tunnel, Germany; Glendoe hydro scheme, Scotland

Table 1.2.: Overview of tunnel boring machines

1.4. Why look-ahead?

For planning, performance and safety reasons, the site for a future tunnel track is well designed prior to the construction process. Extrapolating the results of a geological mapping at the surface is usually the basis for a geological cross section of the tunnel trajectory. Additional geophysical measurements can reveal more details on the structure below. However, extrapolating geological information does not necessarily predict the underground structure correctly. The dipping of a fault zone apparent at the surface can change with the depth or lithological changes may occur without traces visible at the surface. Moreover, the application of geophysical measurements in urban areas is very limited. Additionally, the vertical resolution of the obtained data decreases by the depth, which prevents a high resolution characterization of the tunnel geology ahead, especially during tunneling of mountains. Thus, a detailed cross section of the underground structure is obtained by geological and geophysical measurements that does not necessarily correlate with the actual geology encountered during the tunnel construction. The only completely reliable sources of information are core samples derived from exploratory drillings. Unfortunately, these drillings are expensive and time consuming, which limits these samplings to discrete measurements only.

Tunneling using tunnel boring machines is considered to be one of the most safe tunneling methods with regard to security in the workplace. The worst case scenario of a TBM drilling into unexpected geology can comprise of water leakage, break outs of the tunnel wall, a partly collapse of the working front or blocking of the cutting wheel. Eventually this causes the tunnel construction to be interrupted for a significant period of time (days) in order to get special equipment, e.g., pumps and digging tools on site. Further constructional changes to the TBM may have to be performed to adapt to the new formation properties. Since the TBM is filling the whole tunnel diameter, the total collapse of a tunnel is almost impossible and the workers are rarely exposed to danger. However, safety issues are not limited to the direct tunnel environment but also deal with the surface above. Drilling vibrations can activate critical fault zones and ground water flow into the tunnel can result in drawdown of the water table and even the surface. This can cause serious damage to buildings and objects on the surface (Curry, 2009).

Real time measurements to predict the geological structures ahead of the tunnel construction can be a useful tool to prevent such threats from happening. They can be used to correlate a priori information gained during surface surveys with the actual spatial location ahead of the tunnel. Also, unknown structures can be imaged before the TBM heads into them. The goal and demands of every look-ahead prediction method is to safely identify possible changes in the rock properties due to fractures, faults, ground water, or lithology. Depending on the rate of penetration (up to 20 $\frac{m}{day}$ in soft rock and less than 10 $\frac{m}{day}$ in hard rock, Kolymbas (1998)), predicting the geology within a minimum range of single meters (approximately one day of drilling time) can be sufficient to react accordingly.

Faults, fracture zones, changes in lithology, etc., usually go along with significant changes in seismic properties, i.e., bulk density, compressional wave (P-wave) and shear wave (S-wave) velocity. Since seismic methods are widely accepted in exploration geophysics due to their large depth of penetration and their flexible and robust measurement geometry, they are therefore the method of choice in tunnel environments. Efforts have been made to apply other geophysical methods (e.g., ground penetrating radar, Blümling et al. (1992); Hiroshi and Naomitsu (2004)). However, most methods failed commercially because of their low resolution, low penetration depths and constructional or physical interference with the tunnel construction. Again, underground exploratory drillings can contribute valuable information. Unfortunately, the drilling carriages can only be placed on the backup train (see Figure 1.6). Consequently, this method requires direct access to the tunnel face through the drivetrain and the cutting wheel. Additionally, the tunneling process has to pause for a couple of hours. For these reasons, exploratory wells are drilled only if explicitly required and do not provide continuous information. In the following, the prediction ahead of the tunnel construction therefore focuses on seismic methods only.

1.5. Seismic tunnel look-ahead prediction systems

Present seismic look-ahead prediction systems can be subdivided by the answer to the simple question: Where can the source and receiver devices be deployed? The most logical location is the tunnel face, since this is as close as possible to structures ahead of the tunnel construction. A seismic wave field excited at the tunnel face is already propagating ahead of the construction and therefore carrying a lot of energy in the favored direction. Reflection signals can be easily recorded by seismic receivers mounted on the working front. Also, seismic processing steps common in surface seismic measurements can be applied due to a similar measurement geometry. Unfortunately, the accessibility of the tunnel face is usually very limited due to the presence of the cutting wheel of the tunnel boring machine. One possible solution is the integration of the source and receiver groups in the cutting wheel (Kneib et al., 2000, Figure 1.7). The Sonic Softground Probing (SSP) system utilizes a shaker included in the cutting wheel to excite a sweep of seismic energy into the rock ahead of the tunnel construction (Figure 1.8, red star and triangle). Reflection signals are recorded by accelerometers. A high engineering effort was invested in order to enable a stable and reliable integration of the measurement and communication devices. Failures in the source and receiver units as well as in the data transfer to the computer system located in control room will automatically and permanently disable the prediction method. Maintenance during the tunneling process is usually not possible. Another prerequisite of the SSP concept is the coupling of both source and receiver to the tunnel face. This is enabled by the highly pressurized material (soil or bentonite suspension) in the excavation chamber in EPB and slurry TBMs (see Chapter 1.3) but limits the application of SSP to tunneling in soft rock. The interpretation focuses on the detection and isolation of reflected P-wave signals. After the determination of the velocity field and the 3-D migration, a volumetric image processing is applied to assist in the interpretation of the data. Even though the measurements devices are an integral part of the TBM, acoustical decoupling from the noise of the cutting wheel enables a continuous prediction during tunneling. Recent surveys using the Sonic Softground Probing system were carried out during the construction of the fourth road tunnel under the river Elbe in Hamburg (Kneib et al., 2000) and the construction of the Leipzig city tunnel (Gehrig et al., 2008).

A second class of seismic tunnel look-ahead prediction systems avoids the mechanical interference of measurement devices and the tunneling machine by using the TBM noise as a source and placing receivers behind the cutting wheel at the location of the backup train or even far behind in the finished section of the tunnel (Figure 1.8, green highlighted cutting wheel and green triangle, Petronio and Poletto (2002); Ashida (2001)). Since a tunnel boring machine is well coupled to the surrounding ground by either gripper shoes or the cutting wheel, the TBM vibration continuously emits seismic waves and thus can be treated as a continuous source.

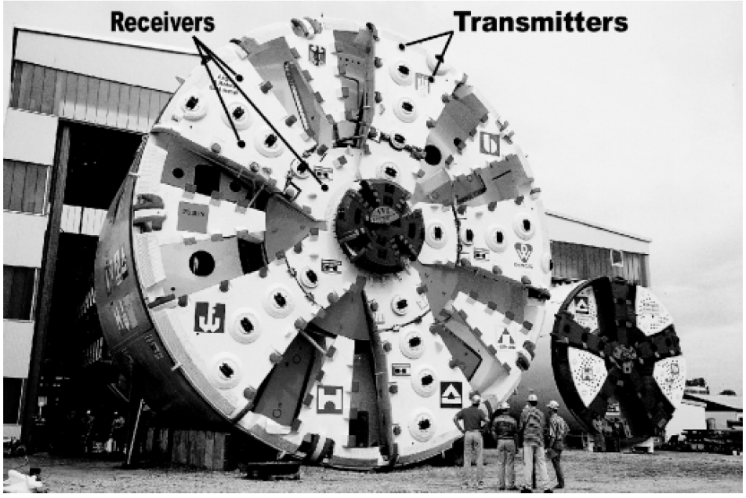

Figure 1.7.: Source and receiver (transmitter) according to the SSP method, integrated in the cutting wheel (taken from Kneib et al., 2000).

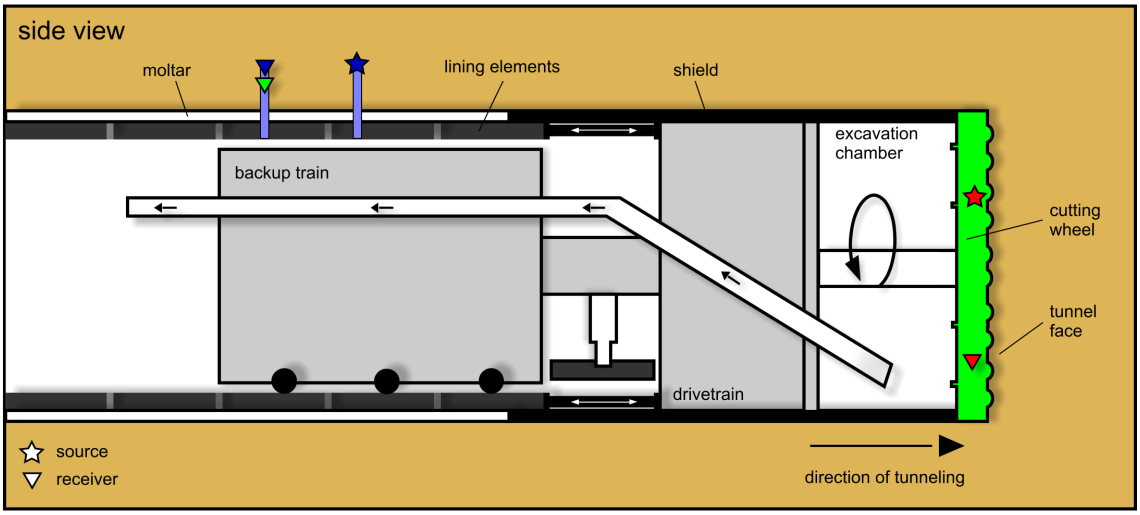

Figure 1.8.: Source and receiver locations of different tunnel look-ahead prediction approaches: SSP (red star and triangle), TSWD (cutting wheel highlighted in green and green triangle), TSP/HSP (blue star and triangle).

Three-component receivers are placed decades of meters behind the tunnel face in boreholes a few meters behind the tunnel wall. Similar to seismic surface measurements using sweeps instead of a single explosion or force source, the pilot source signal is recorded by a receiver mounted close to the cutter head. Cross correlation of the pilot trace with the signal response recorded by the deployed receivers along the tunnel wall provides interpretable data. By analyzing the polarization information gained from the three components of the seismic receiver, P- and S-waves can be distinguished and the incidence of the incoming wave can be detected in order to decrease the imaging ambiguities. Surface waves and other noise originated from, e.g., generators and pumps are suppressed by the distance of the receiver anchors to the tunnel wall. The reflected body wave signals are interpreted by either equi-travel time planes (Ashida, 2001) or migration. The most recent measurements using Tunnel Seismic While Drilling (TSWD) has been performed in the Hieflau Gallery, Austria (Brückl et al., 2008).

The comparison of TBM noise after cross correlation with the pilot trace and small blasting in boreholes behind the TBM has been shown by Ashida (2001) and leads to the third major class of tunnel seismic prediction concepts. Having control of the source can increase the signal-to-noise ratio and supersede cross correlation. However, the seismic source has to be placed behind the TBM instead of close to the tunnel face to minimize interference with the tunnel construction (Figure 1.8, blue star and triangle). Two prediction methods using small explosive charges (less than 200 g) and receiver anchors a few meters behind the tunnel wall are described by Dickmann and Sander (1996) (Tunnel Seismic Prediction, TSP) and Inazaki et al. (1999) (Horizontal Seismic Profiling, HSP). Both approaches utilize 3-component receivers in order to separate and interpret P- and S-waves and gain additional information on the wave incidence. Since the explosive source is placed along the tunnel wall, it predominantly emits body wave energy radial to the tunnel wall. This way, the detection of fault zones focuses to the side rather than ahead of the tunnel construction. However, lithological boundaries with low to moderate dipping angles with respect to the tunnel axis can be predicted. In most cases, the expected intersection of a geological structure with the tunnel axis has to be extrapolated from the migrated data. The potential for imaging structures using the TSP method has been recently shown during the construction of the Zuckerberg gallery, Germany, and the Cheshmeh Langan Water Supply Tunnel project, Iran (Dickmann, 2005). The HSP approach has been successfully tested at the Tsukui conduit tunnel, Kanagawa, Japan (Inazaki et al., 1999).

All the measurement approaches focus on the registration of body waves. Either by picking only the first arrivals of P- and S-waves or by placing the receivers away from the tunnel wall, the surface wave information is neglected. Also, the interpretation of the reflection signals is mostly based on a standard seismic migration. The most sophisticated prediction methods in terms of field test, measurement device development, automatic interpretation, data visualization and commercial use seem to follow the Sonic Soft ground Probing (SSP) or Tunnel Seismic Prediction (TSP) concept.

CHAPTER II

Tunnel look-ahead prediction using surface waves

All of the seismic prediction methods described in the previous chapter focus on the excitation and registration of body waves, respectively. Remarkably, the utilization of explosive charges and the cutting wheel noise as a seismic source predominantly excites surface waves (Yang et al., 2007). Nevertheless, most interpretation schemes base on the detection of the direct and reflected P-wave. Surface waves are treated as unwanted signals. If 3-component receivers are available, S-wave arrivals are registered and interpreted as well. In most cases, the final processing step is the migration of the detected P- and S-wave arrivals in order to image geological structures ahead of the tunnel. More sophisticated approaches apply an additional volumetric image processing to highlight structures within the migrated section.

Since 1999, an alternative Integrated Seismic Imaging System (ISIS) has been developed (Borm et al., 2003a,b). A repetitive pneumatic hammer is directly applied to the tunnel wall and excites not only body waves but surface waves, which travel along the tunnel wall and are neglected or even suppressed in common seismic prediction systems. These waves are called *tunnel surface waves* (*TS-waves*). Previous publications address these tunnel surface waves as *tunnel waves* (*T-waves*) (Lüth et al., 2005) or *Rayleigh-waves* (*R-waves*) (Bohlen et al., 2007). In this thesis, the term *TS-waves* is used instead to emphasize the character of waves traveling along the tunnel wall surface. The seismic response is recorded by 3-component receivers anchored in the tunnel wall. Considerable advantages arise from this approach:

- Since source and receiver are placed behind the tunnel boring machine along the tunnel wall, there is no significant interference with the tunneling operation.
- No boreholes have to be drilled in order to deploy explosive charges resulting in less possible threads to the surrounding rock and the lining of the tunnel.
- A large number of shot points can be realized without much effort.
- In the majority of cases, the surface waves carry the most excitation energy when the source is placed close to the tunnel wall.
- The surface wave amplitude decay can be expected to be significantly smaller than the amplitude decay of body waves as they suffer from less geometrical spreading.

The research on the tunnel look-ahead prediction method using tunnel surface waves is the result of ongoing research and includes collaboration/contribution of many scientists. Some material presented in this thesis has been published or will be published in scientific journals.

Therefore, I generally use the term ‘we’ instead of ‘I’ to refer to the originators throughout the following chapters.

The thesis is organized as follows. Chapter 2.1 provides a detailed description of the prediction method on the basis of snapshots and seismograms gained from finite difference time domain (FDTD) modeling. The measurement scheme and some aspects like the difference of body waves and tunnel surface waves are described. Most results have been published in Bohlen et al. (2007) with contributions from me as a co-author. Since this paper deals with the introduction of the prediction method and therefore covers aspects, which are investigated in more detail within this thesis, the method description illustrated by finite difference (FD) modeling has been rewritten here. In Chapter 2.2, we briefly review the interpretation approaches that have been developed initially to adopt the prediction scheme using TS-waves to image structures ahead of the tunnel. A more detailed description of the measurement devices is given in Chapter 2.3.

Measurements of tunnel surface waves and related effects in real tunnel environments are usually time consuming and require technical, logistical as well as human resources. In contrast, the computational power of modern computer system enables the true modeling of wave propagation around a tunnel with respect to a given model. Therefore, most of the investigation in this thesis are performed first on synthetic modeling data. Afterwards, tunnel measurement data is used to validate the results. Naturally, a model used for the wave simulation cannot cover all aspects occurring in nature. However, the separate consideration of aspects that might influence the excitation and propagation of tunnel surface waves can isolate possible disturbances and highlight optimization strategies. Consequently, Chapter 3 deals with the possibilities and limitation of the seismic wave simulation and includes the research on the following items:

- the modeling methods, i.e., coordinate systems, modeling in two and more dimensions,
- the discretization of the tunnel grid for modeling,
- the TSST-prediction in hard and soft rock formations,
- the excavation damage zone (EDZ) and its influence on the TS-wave dispersion,
- the lining of the tunnel and its implications for the excitation of the TS-waves.

By an analytic solution of the wave equation in cylindrical coordinates, finite difference modeling and field data acquired at the Gotthard Base Tunnel (GBT), we then investigate the excitation and propagation characteristics of tunnel surface waves in terms of particle motion and propagation velocity. Chapter 4 introduces fundamental aspects of the nature of these tunnel surface waves, which can be described by both S-wave and Rayleigh wave properties. The content of this chapter has been submitted and accepted for publishing in the journal *Geophysical Prospecting* (Jetschny et al., 2010) with me as the first author (doi: 10.1111/j.1365-2478.2009.0823.x).

In Chapter 5, we finally propose a processing scheme to isolate and interpret the TS-wave reflection events originated from geological inhomogeneities. Thereby, a structures ahead of the tunnel face is automatically detected and its distance to the tunnel face is calculated without a priori information. The content of this chapter has been prepared for publication in the journal *Geophysical Prospecting* with me as the first author. A discussion that covers the propagation, excitation and registration of tunnel surface waves in order to map geological structures ahead of the tunnel construction can be found in Chapter 6.

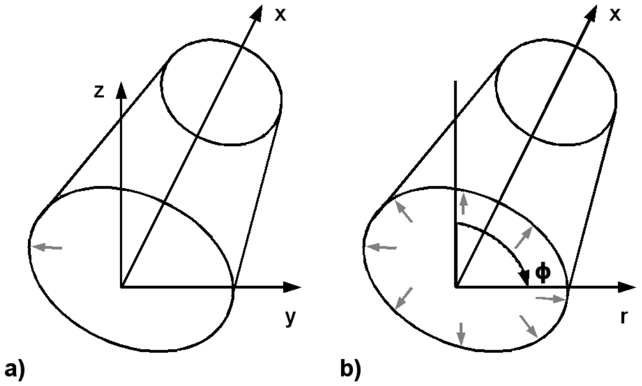

Figure 2.1.: Coordinate systems used in this thesis. a) The Cartesian coordinate system is used for the 3-D modeling (*fdmpi*). x is parallel to the tunnel axis, y is normal to the right and left tunnel wall and z denotes the vertical axis (normal to the top and bottom tunnel wall). The light gray arrow indicates a single force source applied to the tunnel wall in y direction. b) The cylindrical coordinate system is used for the 2.5-D modeling (*fdbh*). r describes the radial, ϕ the azimuthal and x the longitudinal coordinate. Due to the azimuthal symmetry of the source, single forces are applied at every point normal to the tunnel wall (ring source).

2.1. TSST concept

Our seismic prediction method using tunnel surface waves (TS-waves) was primarily developed by the help of wave field simulations (Bohlen et al., 2007) and there are only few available field data sets. Therefore, wave field modeling is our primary method to research and illustrate aspects of the prediction system. For most of our wave field simulations, we use a 3-D parallelized viscoelastic finite difference code *fdmpi* that can simulate the seismic wave response according to various given models in the time domain. As an output, snapshots of the wave field at specified time intervals and seismogram traces of receivers at variable locations are given. The 3-D time domain simulation code uses a Cartesian coordinate system according to Figure 2.1a. For more detailed information on the FD modeling code, we refer the reader to (Bohlen, 2002). A brief introduction to the wave simulation using the finite difference method an their capability is given in Chapter 3.1.

A basic prediction scheme is displayed in Figure 2.2, which combines snapshots of the finite difference simulation of the wave field with the sketch of a TBM (Figure 1.6). According to this Figure, the seismic prediction concept comprises of the following steps:

1. the excitation of both body waves (P- and S-waves) and TS-waves,
2. the propagation of body waves into formation and TS-waves along the tunnel wall,
3. the conversion of TS-wave into mainly S-waves at the tunnel face,
4. the propagation of converted S-waves ahead of the tunnel,
5. the back-propagation of converted S-waves after reflection at structures ahead of tunnel,
6. the back-conversion of converted S-waves into TS-waves and the propagation along the tunnel wall.

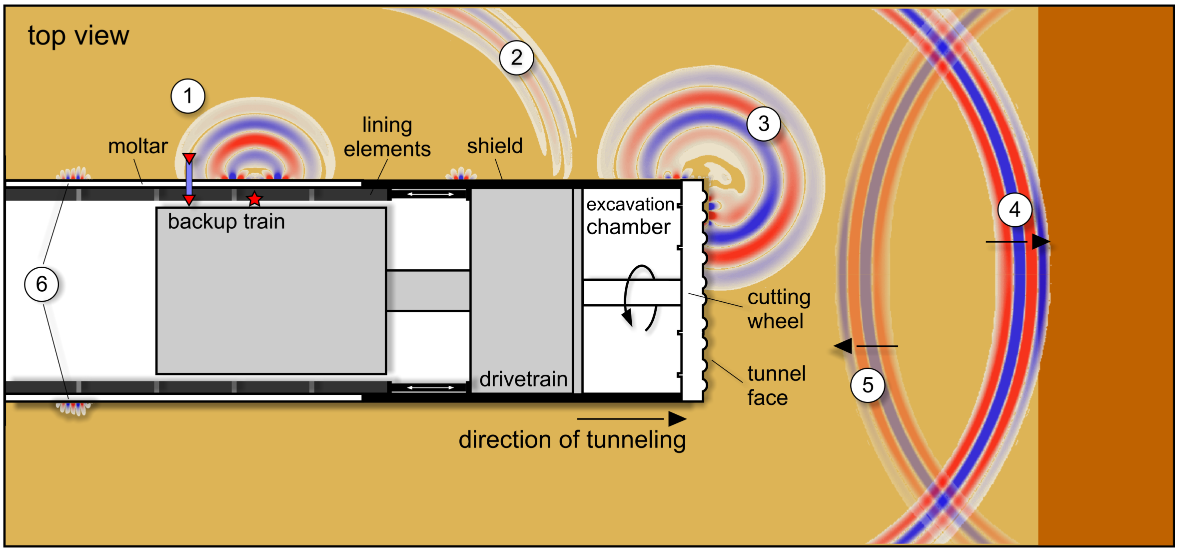

Figure 2.2.: Scheme of the seismic tunnel look-ahead prediction using TSST-waves (top view). The source position and the receiver location either on top or anchored behind the tunnel wall are marked by a red star and red triangles, respectively. 1) the excitation of the wave field by a point force source, 2) the propagation of direct TS- and S-wave along the tunnel wall, 3) the conversion of the TS-wave at the tunnel face, 4) the forward propagation of the converted S-wave, 5) the backward propagation of the reflected S-wave, 6) the TS-wave propagation along the tunnel wall after back-conversion.

As can be seen, the wave of interest is the back-converted TS-wave, which can give information on the spatial location of the reflecting structure ahead of the tunnel. According to its wavepath as a direct TS-wave, converted S-wave, reflected S-wave as well as back-converted TS-wave, we call it *TSST-wave*. For simplification, we also refer to the introduced look-ahead approach as *TSST prediction*. Note that previous publications, e.g., Bohlen et al. (2007), assumed that tunnel surface waves can be fully described by Rayleigh wave properties. Therefore, they call these converted, reflected and back-converted waves RSSR-waves. Later in the thesis, it is demonstrated that TS-waves can be described by both shear wave and Rayleigh wave properties.

A more comprehensive build-up of FD wave field snapshots can be found in Figure 2.3. Here, the synthetic wave field for a simple tunnel model is separated into P-wave (div) and S-wave components (curl) by calculating the divergence and the magnitude of the curl of the particle velocity field (Dougherty and Stephen, 1988). In our simple model, an evacuated tunnel tube (10 m diameter) has been inserted into a homogeneous crystalline hard rock. Ahead of the tunnel face, there is a fault zone representing a geological structure with a significant contrast in elastic properties. The seismic properties for the tunnel, the rock formation and the fault zone are listed in Table 2.1.

In our simulation, a point force source is applied normal to the tunnel wall, which simulates a pneumatic hammer source (Figure 2.2, red star; Figure 2.1, gray arrow). The source wavelet is a Ricker signal with a center frequency of 500 Hz and a maximum frequency of approximately 1000 Hz. 3-component receivers parallel to the tunnel wall at the same side of the source

parameter	tunnel	hard rock	soft rock
ρ [kg/m^3]	1.25	2200.0	1200.0
v_p [m/s]	0.0	5100.0	2000.0
v_s [m/s]	10^{-6}	3100.0	800.0
Q_p	∞	500.0	100.0
Q_s	∞	500.0	100.0
ν	–	0.2	0.4

Table 2.1.: Material properties used in the simulation of the TSST-wave look-ahead prediction in soft rock and hard rock. Given are the values for bulk density ρ, the seismic velocities v_p and v_s, the quality factors Q_p and Q_s for compressional waves (P-waves) and shear waves (S-waves), respectively, and the Poisson's ratio ν (modified from Bohlen et al., 2007).

record the particle velocity (Figure 2.3, $T = 1$ ms, white dotted line; Figure 2.2, red triangle), which can be outputted as seismogram traces. In the following, we concentrate on Figure 2.3 and refer to single pictures by the propagation time.

The point force source excites a wave field comprising of direct P-waves, S-waves and TS-waves ($T = 1$ ms). The direct P-wave propagates predominantly normal to the tunnel wall into formation and is therefore of limited use for the prediction of the geology ahead of the tunnel face. In contrast, the S-wave propagates parallel to the tunnel wall. The TS-wave is the strongest signal and visible in both the curl and div snapshots due to both compressional and shear components, which is typical for surface waves ($T = 5 - 7$ ms). Since the TS-wave velocity and the S-wave velocity is close together and the modeled tunnel is short, S-wave and TS-wave do not significantly separate. When reaching the edges of the tunnel, the direct TS-wave is both reflected and converts into body waves. The tunnel edges can be thus treated as new source positions. From the snapshot at $T = 10$ ms and at $T = 12$ ms we see that mainly S-waves are emitted ahead of the tunnel face with a maximum of amplitude close to the tunnel axis. These converted S-waves (TS-S-waves) are approaching the fault zone ahead of the tunnel face and are reflected back to the tunnel ($T = 15 - 25$ ms). When the reflected S-waves reach the tunnel face, they are back-converted into TS-waves ($T = 30$ ms), which propagate along the tunnel wall ($T = 35$ ms). Even though P-waves are generated during the conversion of the direct TS-wave and the reflection at the fault zone, they do not significantly contribute to the seismic response recorded at the receiver line. The TSST-wave is the most dominant reflection event.

As can be seen from the wave field snapshots, the tunnel surface wave bears most of the energy when deploying a force source normal to the tunnel wall. Also, the energy loss of the TS-wave propagating along the tunnel wall is small by comparison to the body wave propagation. Even if the source is placed decades of meters behind the tunnel face, there is still a significant amount of excitation energy converted into body S-waves traveling ahead of the tunnel. This way, waves are propagating in the favored direction without placing a source at the tunnel face and thereby interfering with the tunnel boring machine. The synthetic seismograms recorded by 3-component receivers parallel to the tunnel wall show that the TSST-wave is the strongest reflection event from the fault zone (see Figure 2.4). The dominant wave amplitudes can be observed on the y-component normal to the tunnel wall. The seismograms also show the direct

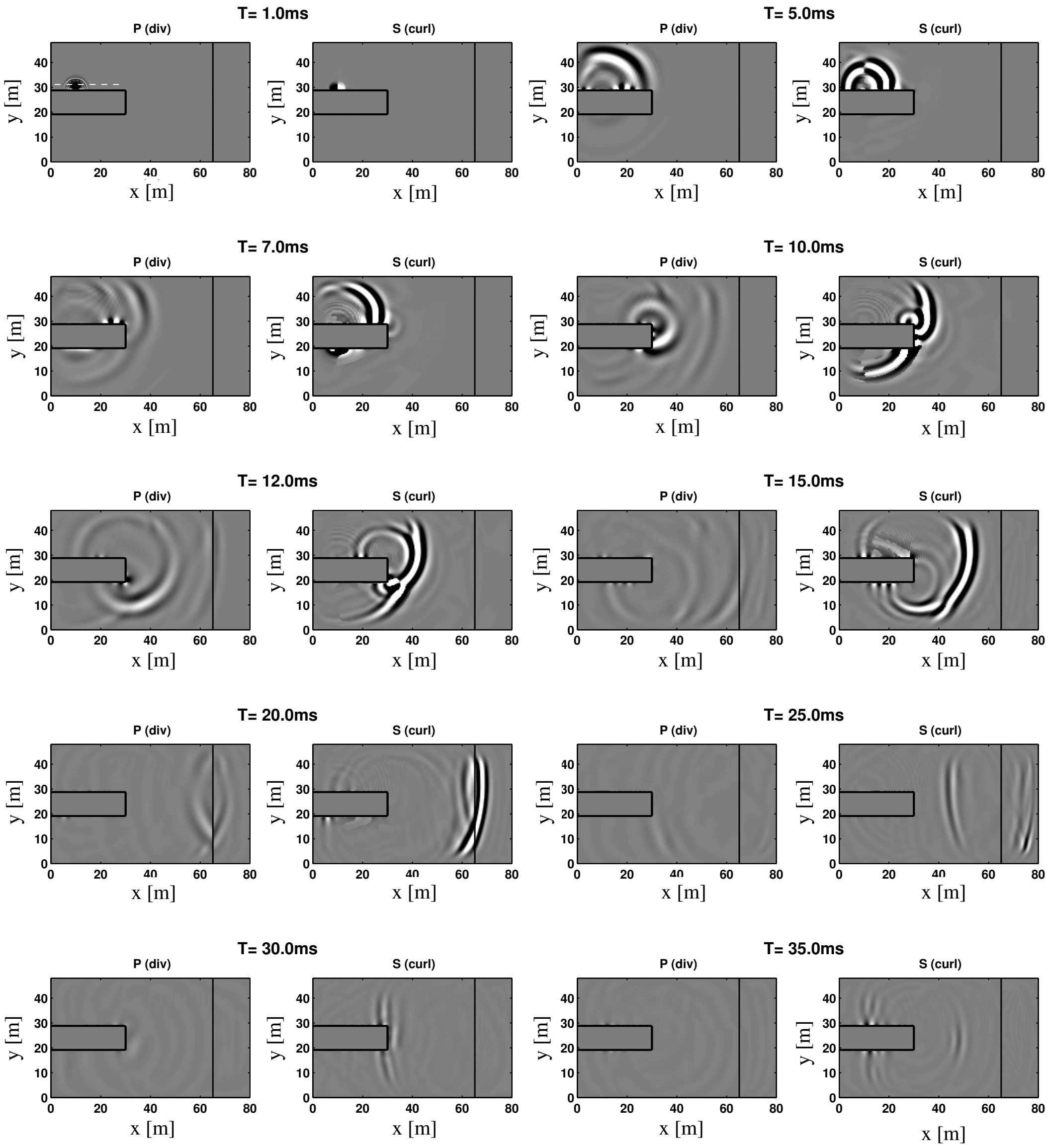

Figure 2.3.: Finite difference modeling snapshots illustrating the look-ahead prediction method using tunnel surface waves. P-wave (divergence) and S-wave (curl) components have been separated (modified from Bohlen et al., 2007).

tunnel surface wave (TS) and the TS-wave circulating the tunnel (cTS). Both waves are not only converted to body S-waves but also reflected as they reach the tunnel face (reflected TS and reflected cTS).

To illustrate the separation of S-wave and TS-wave, we simulated the wave propagation for another simple model with an extended tunnel. The snapshots for this simulation are displayed in Figure 2.5. Similar to Rayleigh surface waves propagating at gaseous-solid interfaces, the TS-wave velocity is expected to be in the range of 0.87 - 0.96 times the S-wave velocity (Ingard, 1988). For a longer tunnel, S-wave and TS-wave clearly separate by time ($T = 38$ ms). Also,

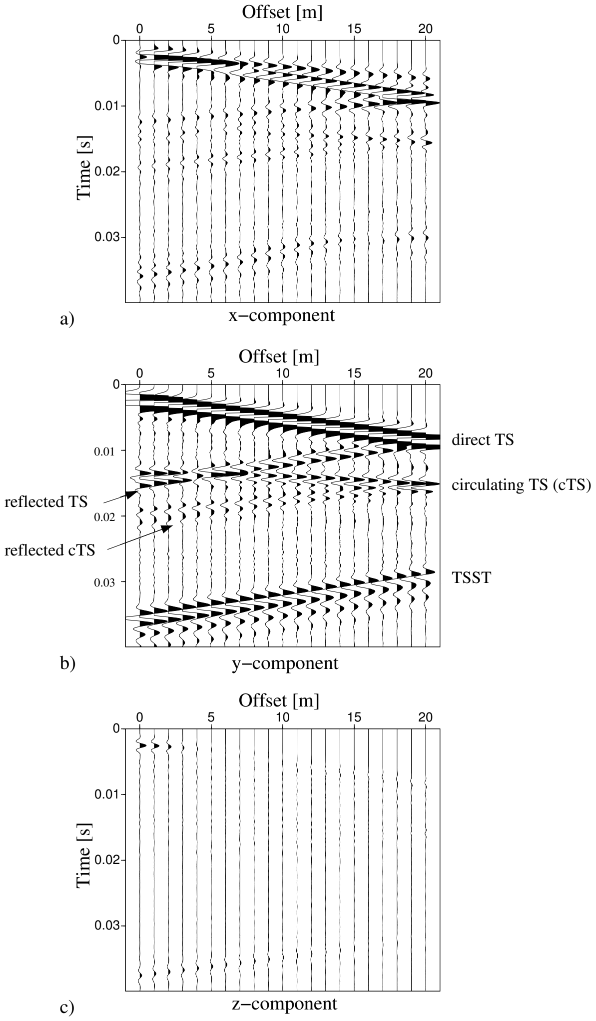

Figure 2.4.: Seismograms according to the snapshots in Figure 2.3. The components are labeled with respect to the coordinate system in Figure 2.1 (modified from Bohlen et al., 2007). Major wave types are marked in the y-component seismogram section.

the amplitude of the S-wave decays toward the tunnel wall. No interaction (e.g., conversion, scattering) of any kind takes place once the S-wave passes by the tunnel face. In contrast, the TS-wave converts to mainly S-waves (TS-S) with a maximum of wave amplitude almost in the tunnel axis ($T = 48$ ms). Most of the S-wave energy propagating toward the fault zone is originated from this TS-wave conversion with minor contribution from the direct S-wave. The converted P-wave (TS-P) exhibits much smaller amplitudes and can be neglected.

In addition to the wave field snapshots and the synthetic seismograms, hodograms of the direct TS-wave are derived from a time window of a seismic trace from Figure 2.4. As can be seen from Figure 2.6, the dominant particle motion occurs in the x-y plane, i.e., in the plane normal to the tunnel axis and the tunnel wall. An elliptical particle motion is visible, while there is only very small movement perpendicular to this plane (x-z plane), which is typical for

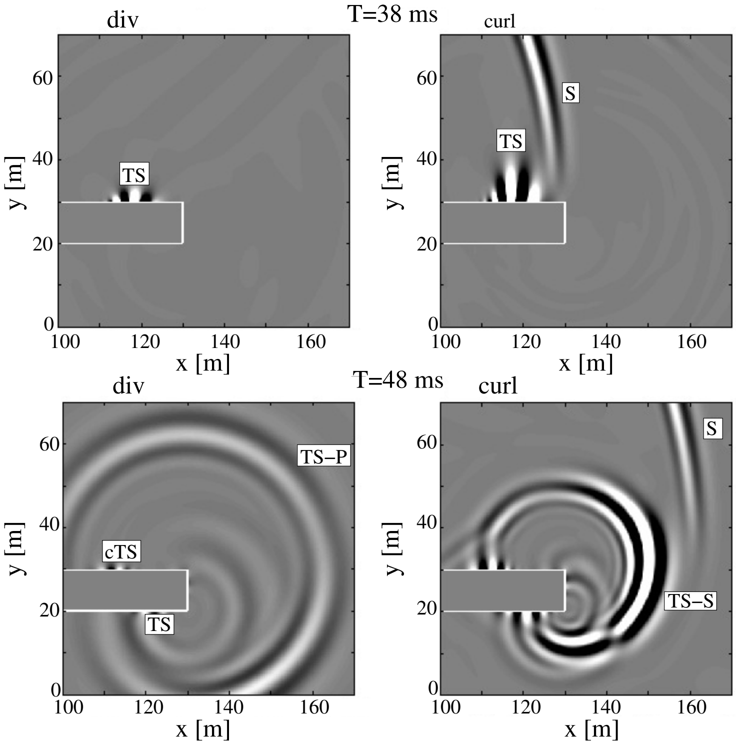

Figure 2.5.: Top view section of finite difference modeling snapshots illustrating the separation of direct S-wave and TS-wave excited by the point force source. P-wave (divergence) and S-wave (curl) components have been separated (modified from Bohlen et al., 2007).

Rayleigh waves. From both the characteristic propagation velocity smaller than the S-wave velocity and the elliptical particle motion normal to the tunnel wall, we can conclude that the TS-wave - for our model geometry and the considered source frequency range - has propagation characteristics similar to that of Rayleigh waves. In Chapter 4, we investigate the excitation and propagation characteristics of tunnel surface waves in detail.

2.2. Basic interpretation

A basic interpretation scheme utilizing TSST-waves to image geological structures ahead of the tunnel is presented in Bohlen et al. (2007). First, the traces recorded by receivers parallel to the tunnel axis are corrected, if necessary, for the dispersion properties of the surrounding excavation damage zone (see Chapter 3.4). Then, we shift each seismogram trace by a time delay of $\frac{s}{v_{\mathrm{ts}}}$, where s is the distance to the source. This way, we compensate for the wave velocity v_{ts} of the TS-waves back-propagating from the tunnel face. Finally, the original seismogram (Figure 2.4, y-component) after correcting and muting of the direct TS-wave is displayed in Figure 2.7a. Both the TSST-wave and the reflected TS-waves originated from the direct and circulating TS-wave arrive at a constant time independent of the receiver offset. Therefore, these arrivals stack constructively, while other waves recorded by the receivers do not. From Figure 2.7b we see that the stacked TSST-wave signal is the most dominant reflected

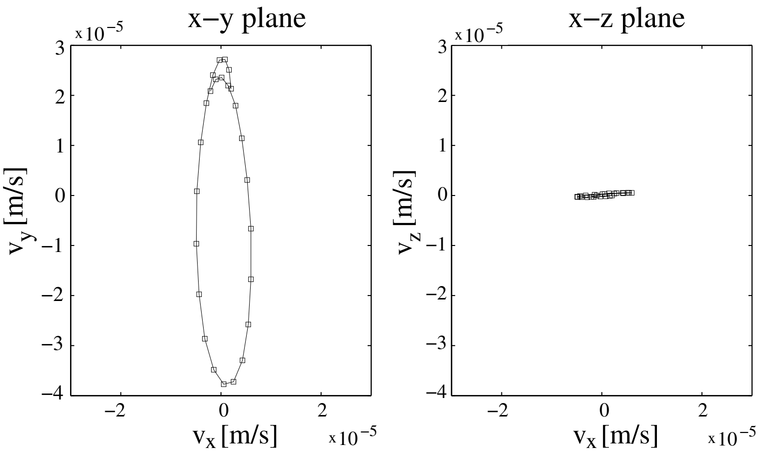

Figure 2.6.: Hodogram of particle velocity of the TS-wave in the x-y plane and x-z plane (modified from Bohlen et al., 2007).

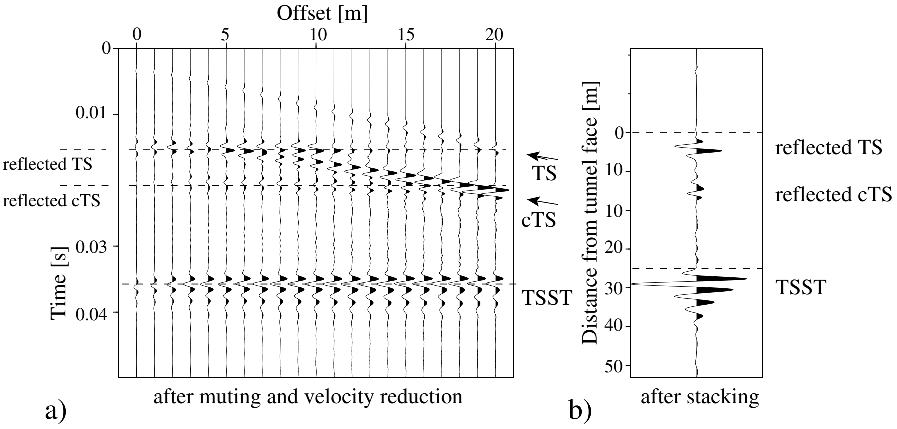

Figure 2.7.: Basic processing of tunnel seismic data shown in Figure 2.4 (y-component) for the imaging of a fault zone ahead of the tunnel face. a) Data after muting of the direct TS-wave and applying a reduction velocity and b) after stacking and conversion of the arrival times to distances (modified from Bohlen et al., 2007).

signal. With the knowledge of the formation S-wave propagation velocity, the distance toward a reflector can be calculated. Further information on the spatial orientation of the reflector with respect to the tunnel axis can be derived, too. This basic interpretation scheme has shown its potential for detecting structures ahead the tunnel in both a synthetic and a field dataset. There is, however, manual input needed, e.g., for the determination of the dispersion properties and the TS-wave velocity.

Another imaging approach using a TSST-wave migration was introduced in Giese et al. (2005). By a first arrival tomography of the tunnel seismic data the velocity field around the tunnel is gained. The seismic response of the 3-component receiver along the tunnel wall

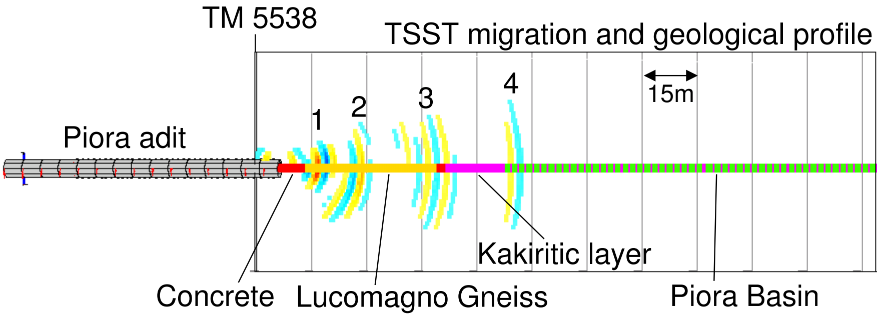

Figure 2.8.: Migrated section of tunnel data acquired during a tomographic survey along the tunnel wall of the Piora adit, near the roadway of the Gotthard Base tunnel, Switzerland. Four distinct events can be identified that correlate with data obtained from an exploratory well (taken from Lüth et al., 2006).

enables the separation of P- and S-wave as well as deriving the incidence of the incoming wave. This way, the polarization information can decrease imaging ambiguities and therefore improve the migration result (Lüth et al., 2005). However, the migration algorithm is a build-in component of the ISIS-software package and is of limited accessibility. Besides, the migrated section still lacks of a clear result and has to be interpreted by a skilled geophysicist or requires further image processing (see Figure 2.7).

2.3. Measurement layout and devices

The measurement layout for predicting the geology ahead of the tunnel construction is fairly simple and consists of standard geophones by Oyo Geometrics and a self-developed pneumatic hammer as a seismic source. Both the computer equipment and the pneumatic hammer source are mounted at the TBM backup train and remain there (Figure 2.9). In contrast, the 3-component receivers can be placed at variable positions along the tunnel wall. Usually, the receivers are either screwed in maintenance holes if the tunnel wall is stabilized by concrete lining elements (Figure 2.10) or mounted on top of a rock anchor behind the tunnel wall. Installation of the hammer, set up of computer equipment and wiring takes a few hours prior to the first measurement. The pneumatic hammer has been developed by the GFZ German Research Centre for Geoscience, Potsdam, Germany, and incorporates a pneumatic cylinder that enables pre-stressing the hammer toward the tunnel wall for good coupling of hammer and rock (Giese et al., 2005). Each impact is powered by a moving mass, takes about 1 ms and is controlled by a programmable steering unit. The hammer transmits seismic pulses of frequencies up to 2000 Hz. With a high degree in accurate and reliable repeatability the signal-to-noise ratio can be significantly improved. 3-component GS-14-L3 geophones by Oyo Geospace are used as receivers. These miniature geophones have been designed for a rugged environment and operate in any position from vertical to horizontal. With a low natural frequency of 28 Hz and a bandwidth between 24 Hz and 3000 Hz, they have been selected for recording tunnel seismic data. Further specifications can be found in www.oyogeospace.com (2009). Limitations of laying out the receivers and applying the source in presence of a tunnel wall lining in soft rock formations can be found in Chapter 3.5.

The actual look-ahead measurement is triggered by the pneumatic hammer blow during frequent TBM maintenance stops. In soft rock formations, every couple of hours (depending on the rock properties) the tunnel construction has advanced by the width of a lining segment (single meters). The tunneling then stops for the construction of a new tubing ring. Thereby the noise level for seismic measurement is low. In hard rock formation, similar kinds of regular stops (e.g., maintenance of the cutter head disks, repositioning of the gripper shoes) can be used for optimal look-ahead measurements. Since the hammer source is fixed on the TBM backup train, the shot location moves at the TBM penetration velocity, while the receivers are spatially fixed in the tunnel wall by either the rock anchor or screwed in a maintenance hole. Occasionally, the position of the receivers are shifted toward the tunnel face to minimize the receiver-to-tunnel face distance and therefore increase the signal-to-noise-ratio. Nevertheless, with a source and receiver position moving at different velocities, the source-to-receiver offsets are very irregular. At every shot, the spatial location of both receiver and the hammer source are thus manually recorded for later reconstruction of the actual measurement geometry.

Up to now, the setup of the measurement devices, wiring, shifting of the receivers and operating the measurement is performed by field technicians. However, it is planned to integrate the measurement devices into the TBM backup train as well as the steering units into the TBM control room. This way, no additional operators are needed in order to perform the measurements. To enable an automatic and real time look-ahead prediction system, the data interpretation has to perform without additional human input, too. Therefore, an automatic imaging approach for tunnel seismic data is introduced in Chapter 5.

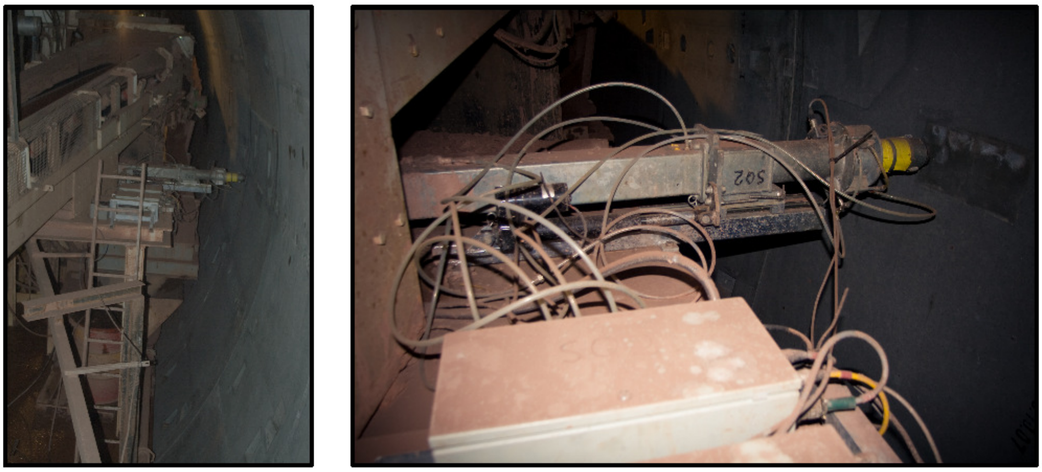

Figure 2.9.: Pneumatic hammer source applied at the tubing segment. These picture have been taken during a seismic survey conducted in the *Neuer Schlüchterner Tunnel* close to Fulda, Germany.

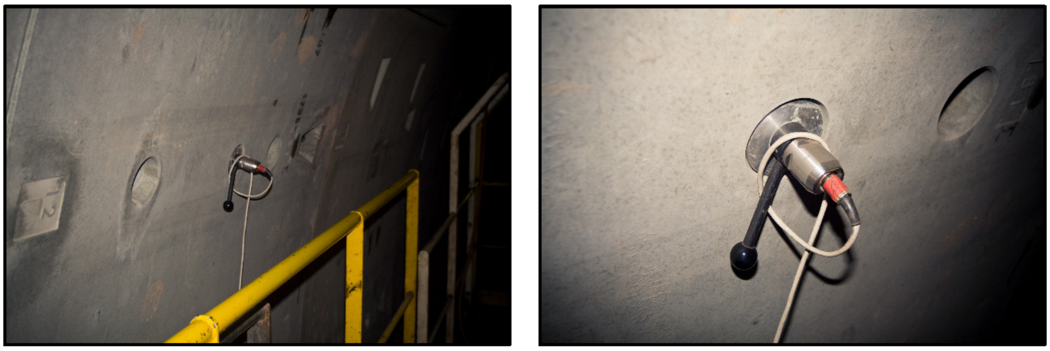

Figure 2.10.: 3-component receiver screwed into a maintenance hole of a tubing segment. These picture have been taken during a seismic survey conducted in the *Neuer Schlüchterner Tunnel* close to Fulda, Germany.

CHAPTER III

Modeling of tunnel effects

Previous modeling studies have already investigated some general material properties, modeling methods or tunnel related wave propagation effects that occur under tunnel conditions or influence the propagation of tunnel surface waves. Bohlen et al. (2007) is the most comprehensive study with respect to the look-ahead prediction using tunnel surface wave and describes among others:

- the modeling strategies in 2-D and 3-D,
- the conversion and the radiation characteristics of S-waves triggered by the arrival of TS-wave at the tunnel face,
- the basic influence of an excavation damage zone (EDZ) around the tunnel in terms of wave dispersion,
- the shape of the tunnel edges and the presence of a simple TBM model.

Other studies concentrate on the investigation of single phenomena like the EDZ properties from seismic tomography surveys without explicitly drawing conclusion for the propagation of TS-waves (Schuster et al., 2001; Borm et al., 2003b). However, at new tunnel construction sites and with modifications to the original measurement layout, new question arise, which can be answered by modeling studies. Conducted seismic surveys parallel to the tunneling progress confirm the TSST prediction approach to be applicable to field data. Nevertheless, there are differences in the modeling response and the acquired field data, since we can only model effects, we already know and understand. In this chapter, we further investigate modeling methods and their limitations, tunnel effects with respect to the TS-wave propagation in more detail (e.g., EDZ properties) and we study new parameters (e.g., lining of the tunnel wall). This way, we can add some puzzle pieces to help interpret field data and improve realistic seismic tunnel simulations. In the following, we concentrate on synthetic case studies only, whose results are addressed in Chapter 4 and 5 when dealing with field data.

3.1. Modeling in 2-D, 2.5-D and 3-D

The modeling of the seismic wave propagation using the finite difference time domain (FDTD) method bases on the approximation of the spatial and time derivation of the wave equation by finite differences. Spatial derivatives of a variable, e.g., the displacement u with respect to a coordinate x like $\frac{\delta u}{\delta x} = \delta_x u$ can be replaced by a finite difference $\frac{u(x_1)-u(x_2)}{x_1-x_2}$ (using second-order finite difference operators). Time derivations such as $\frac{\delta u}{\delta t} = \delta_t u$ are likewise approximated by $\frac{u(t_1)-u(t_2)}{t_1-t_2}$. First, a continuous model is approximated by a grid where elastic properties are assigned to each grid points (Lamé parameters). In equidistant finite difference (FD) schemes, the spatial distance of neighboring grid points dh is constant and controls the smallest occurring structure effective for the wave simulation. After applying a source function to a grid point, the elastic fields of the wave propagation (e.g., stress, particle velocity) are updated for each grid point at discrete time steps dt. In order to save computational time (less updates of elastic parameters for a propagation time considered), dt is meant to be large. However, dt as a function of the initially given dh strongly effects the numerical stability of the finite difference scheme (see Equation 3.3). In return, a coarse spatial discretization (large dh) can cause numerical artifacts (*grid dispersion*) - even in homogeneous media (see Chapter 3.3). For a finite difference wave modeling on a staggered scheme of second order accuracy in time and fourth order accuracy in space within an elastic medium, Robertsson et al. (1994) propose 8 grid points inside the minimum body wave wavelength in order to tolerate less than 2% numerical dispersion error (grid dispersion). That means:

$$\frac{\lambda_{\text{min}}}{dh} \geq 8 \quad \text{with} \quad \lambda_{\text{min}} = \frac{c_{\text{min}}(f_{\text{max}})}{f_{\text{max}}}, \tag{3.1}$$

and $c_{\text{min}}(f_{\text{max}})$ the smallest phase velocity occurring in the model (usually the shear wave velocity) at the largest source signal frequency f_{max}. With $f_{\text{max}} \approx 2 \cdot f_{\text{c}}$ it follows that

$$\frac{\lambda}{dh} \geq 16, \tag{3.2}$$

where λ is the dominant wavelength associated to the source center frequency. This relation seems more applicable for FD modelings, since we directly input f_{c} as a parameter for the wave simulation. The recommended wavelength-to-discretization ratio will increase to about $\frac{\lambda}{dh} > 20$ when using second order accuracy in space. The numerical stability is given by

$$dt \leq \frac{6}{7\sqrt{D}} \cdot \frac{dh}{c_{\text{max}}(f_{\text{max}})} \tag{3.3}$$

with $D \in \{1,2,3\}$ the dimensional order of the FD scheme (Blanch et al., 1995).

By applying simplifications and by choosing a reference coordinate system, derived FD modeling codes can differ significantly with respect to the modeling performance, the underlying model and of course the results of the wave simulations. Figure 3.1 illustrates the modeling in multiple dimensions. In 2-D, only a vertical slice of the model cube has to be generated and this slice is extended infinitely in the y-direction. This way, the influence of the third dimension is neglected and so are 3-D wave propagation effects like geometrical spreading. A tunnel becomes a plane layer intersecting a full space and other modeled structure within the volume extend to, e.g., infinite layers or tubes. However, the 2-D finite difference approximation of the wave equation has to consider spatial derivations in only two dimensions, which significantly decreases the memory consumption and the computational time.

Seismic modeling in three dimensions using a Cartesian coordinate system overcomes any limitations regarding the design of the model. By the spatial discretization, every continuous structure within a model geometry can be recreated as a discrete model grid. Nevertheless, refining of the model discretization (decrease of the spatial distance between two neighboring grid points) is strongly affecting the computational performance. If only the spatial discretization of a 3-D model is halved in each dimension, the memory consumption is cubed and the computational time increases by a factor of $2^4 = 16$. Therefore, the fine Cartesian discretization of variable structures can be problematic if non-Cartesian structures (e.g., a tube) are modeled. Possible effects of the discretization with respect to the TS-wave simulation are investigated in Chapter 3.3.

A compromise between the modeling in 2-D (low computational effort, plane wave propagation) and 3-D (high computational effort, discretization limits) is provided by an approximation of the wave equation in cylindrical coordinates with a rotational symmetry regarding the x-axis (Figure 3.1b). This way, a realistic 3-D wave simulation only limited by the rotational symmetry of the model, can be performed at the approximate computational effort of a 2-D modeling (Randall, 1991). We therefore call this method 2.5-D modeling. As a consequence of the rotational symmetry, a point source off the symmetry axis automatically turns into a ring source. Furthermore, a modeled fault zone ahead of the tunnel with an inclination angle relative to the x-axis rotates into a circular cone rather than a plane interface.

Further basic simplification to the FDTD algorithm can be applied. *Acoustic* modeling codes neglect the elastic properties of media and can only model the propagation of compressional waves, e.g., the P-wave propagation in the ocean. *Elastic* codes can model compressional, shear as well as surface waves by taking elastic model properties into account. Additional attenuation properties are considered in *viscoelastic* simulation codes. Even more sophisticated codes can also handle *anisotropic* media. The FDTD modeling codes used in this studies are *fdveps* (2-D), *fdbh* (2.5-D) and *fdmpi* (3-D), which can all simulate the viscoelastic wave propagation in isotropic media. Both the 2-D and 3-D finite difference modeling code have been presented in Bohlen (2002).

The FD modeling of wave propagation considering three dimensions can be defined as a “reference” due to the fact that this modeling method neglects the fewest wave propagation effects and implies more freedom in the design of the model grid. However, this method is also demanding high computational resources. For the investigation of simple model geometries or structures, it is reasonable and feasible to consider alternatives in order to save computational time. A basic comparison of wave propagation modeled in 2-D and 3-D has been already performed by Bohlen et al. (2007). At that time, the 2.5-D modeling code has not been available. However, it first has to be investigated whether the TS-wave propagation along plane interfaces and a tunnel surface is comparable. Chapter 4 deals intensively with this topic. Since the computational effort for the 2-D and 2.5-D wave simulation measures in the same range, it is reasonable to also focus on the comparison of the seismic response in 2.5-D and 3-D. Besides, the rotational symmetry of the model can be easily exploited for modeling of wave propagation around a tunnel as an ideal tunnel is naturally symmetric with respect to the tunnel axis.

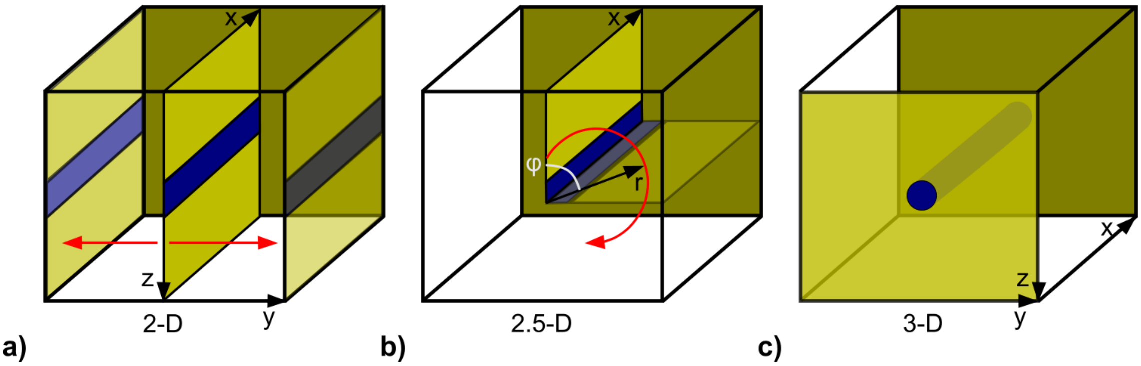

Figure 3.1.: Simplified tunnel model geometries according to different finite difference (FD) modeling codes. a) 2-D, fdveps: a vertical slice of a model is extended infinitely in the horizontal y-direction (red arrows). b) 2.5-D, fdbh: a vertical slice of a model is rotated with respect to the horizontal x-direction (red arrow). c) 3-D, fdmpi: a homogeneous full space model with a tunnel.

In previous wave field simulations of the TSST prediction, a single point force source applied to the tunnel wall has been used, which reflects the impact of a pneumatic hammer (see Chapter 2.3). Due to the rotational symmetry, there are no point sources off the symmetry axis available in the 2.5-D modeling code. A direct comparison has to employ both a ring source in 2.5-D and 3-D. Note that after rotation of the source in 2.5-D, the force source is always normal to the tunnel wall. In order to simulate such a force ring source using the 3-D code, a discrete number of sources has to be placed around the tunnel and each single point force has to have a different force orientation normal to the tunnel wall. Unfortunately, in the current version of fdmpi, the force direction cannot be set independently for each source location. Thus, we focus on a ring explosive source, since an explosive source emits waves omni-directional.

We use the hard rock material parameters, a homogeneous tunnel model and the acquisition geometry described in Chapter 2.1 and Table 2.1. The tunnel has been lengthened to 60 m, the tunnel face-to-fault zone distance is 20 m. The tunnel diameter remains at 10 m. The overall model size extends to 90 m in x-direction (the direction of the tunneling) and 60 m in each other dimension. The point and ring source is placed at x = 10 m, respectively. Its source center frequency f_c equals 500 Hz, the maximum frequency f_max occurring in the wave simulation is about twice the source center frequency. If not stated differently, the default spatial discretization is $dh = 0.2$ m. The time stepping dt is chosen to be close below the stability limit according to Equation 3.3. With the given shear wave velocity $v_\mathrm{s} = 3100\ \frac{\mathrm{m}}{\mathrm{s}}$ and $f_\mathrm{c} = 500$ Hz, the shortest dominant body wave wavelength λ_s equals about 6.2 m. This wavelength is represented by 31 grid points.

The receivers are lined up parallel to the tunnel axis and behind the tunnel wall. In the case of a single point force, the receiver line and the source are located at the same tunnel wall side. If not stated differently, the seismogram sections are limited to the offset range 0 - 80 m (source position to fault zone). For most of the following synthetic case studies, the model dimensions and measurement layout are kept constant. According to the formation simulated, the material properties switch to and from soft rock and hard rock parameters listed in Table 2.1.

First, we focus on the 3-D seismic response caused by a single point force source and a ring of explosive sources around the tunnel. The corresponding seismogram sections are displayed in Figure 3.2a and b. Since the source strength of an explosive source and a point force source are implemented differently in the fdmpi code, we scale the amplitudes in both seismograms independently in order to enable maximum visibility. The interpretation draws qualitative conclusions only. Even though different source types are used, the seismograms are almost identical. The direct P-wave arrivals are more pronounced with an explosive ring source, while there is circulating TS-wave (cTS) only visible in the seismogram with a point force excitation. Direct TS-wave and the TSST-wave, both relevant for the seismic prediction, are very similar in terms of relative amplitude, phase and arrival time. The normalized traces extracted from each seismogram reveal that the signal shape, the phase information as well as the relative amplitude decay from direct-TS-wave-to-TSST-wave is almost identical. Similar results can be observed when comparing an explosive ring source excitation using the 2.5-D and the 3-D simulation code. The common-shot gather (CSG) and an extracted trace from each seismogram are displayed in Figure 3.3. The only apparent difference is visible in the TSST-wave signal shape (Figure 3.3c). Even though the TSST-wave arrival time is constant, both TSST-wave signals are slightly drifting out of phase. This can be the result of different dispersion properties, possibly due to the different discretization of the tunnel geometry.

We can conclude that from the modeling point of view, there are no significant differences in a point force excitation in 3-D and an explosive ring excitation in 2.5-D for the look-ahead prediction. The only limitation is due to the inclination angle of a modeled fault zone relative to the tunnel axis. Other inclination angles beside 90° (orthogonal to the x-axis) ultimately deform the plane reflector to a circular cone. Furthermore, the circulating TS-wave (cTS) is neglected in the 2.5-D simulation data. The excitation of the direct TS-wave propagating along the tunnel wall is almost identical in both modeling codes in terms of signal shape and phase information. The direct TS-wave-to-TSST-wave amplitude decay can be considered as constant.

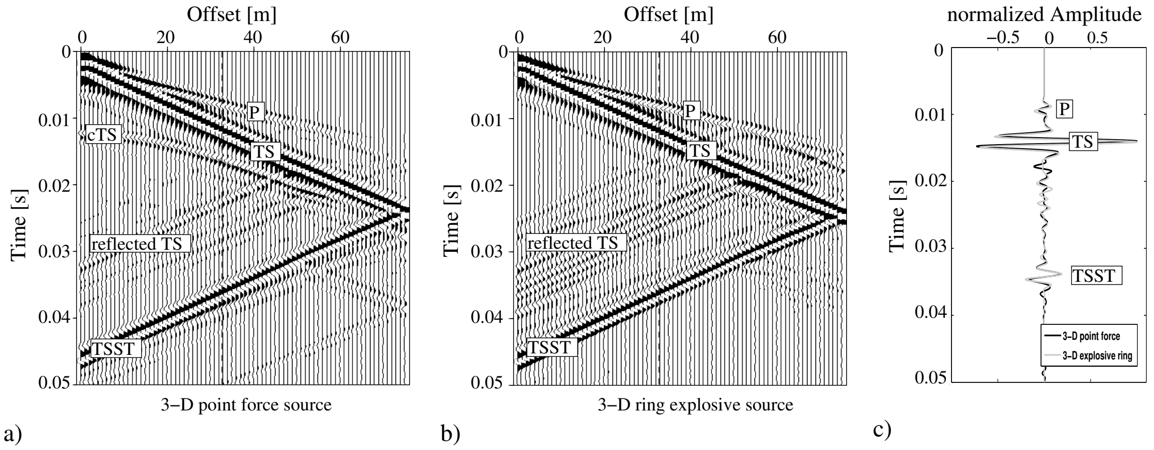

Figure 3.2.: Common-shot gather of a 3-D finite difference modeling according to a homogeneous full space with a) point force excitation (force normal to tunnel wall) and b) explosive ring source excitation. For each modeling, source and receivers are located at the same side of an evacuated tunnel and the receiver component is normal to the tunnel wall (y-component). Major wave types are labeled. c) Normalized traces have been extracted from each seismogram along the dashed line.

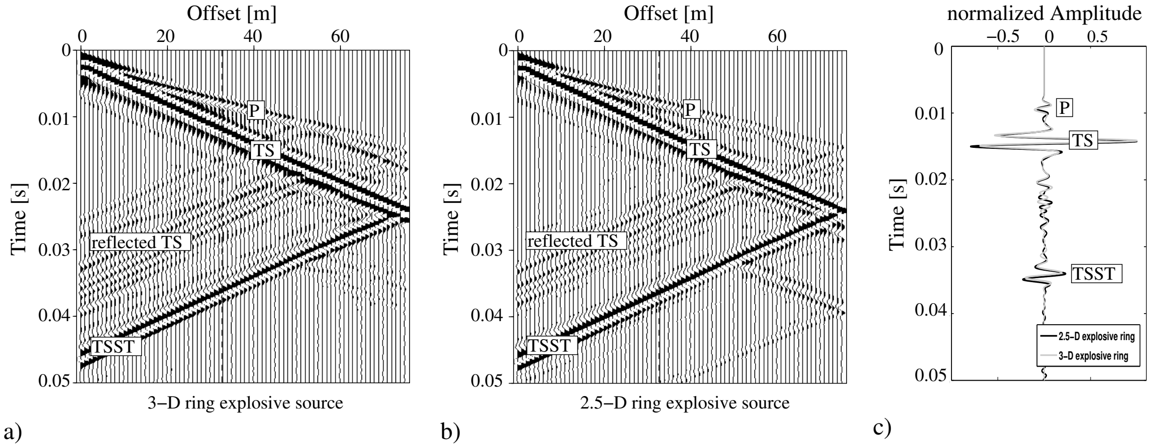

Figure 3.3.: Common-shot gather of a) a 3-D finite difference modeling according to a homogeneous full space with explosive ring source excitation and b) a 2.5-D finite difference modeling according to a homogeneous full space with explosive ring source excitation. For each modeling, source and receivers are located at the same side of an evacuated tunnel, the receiver component is normal to the tunnel wall (y-component and r-component, respectively). Major wave types are labeled. c) Normalized traces have been extracted from each seismogram along the dashed line.

3.2. Look-ahead prediction in soft rock and hard rock

Originally, the seismic look-ahead prediction using tunnel surface waves was developed to focus on hard rock tunneling rather than the commercial look-ahead prediction system Sonic Softground Probing (SSP), which is limited to prediction in soft rocks (see Chapter 1.5). With the availability of mostly construction sites tunneling through soft rock for field surveys, the TSST look-ahead method was tested in such environments, too. Previous modeling studies have been performed in hard rock only (Bohlen et al., 2007), thus, we further investigate the general applicability of the prediction approach in weaker rock formations. As previously mentioned in Chapter 1.1, soft rock and hard rock primarily differs with respect to their tunnel stand-up time. Soft rock comprises of sediments like clay, silt, sand, gravel or mud and is characterized by lower density and seismic velocities as well as higher attenuation. Table 2.1 lists parameters for a typical soft rock and hard rock used in the simulations.

Generally, we do not expect to observe fundamental differences in the propagation of TS-waves in soft rock and hard rock. The major difference is due to the resulting TS-wave wavelength, which can imply numerical or discretization artifacts. From the source center frequency $f_\mathrm{c} = 500$ Hz and the material parameters in Table 2.1 we can calculate the dominant TS-wave wavelength: $\lambda_\mathrm{hard} = \frac{v_\mathrm{ts} \approx 0.9 \cdot v_\mathrm{s}}{f_\mathrm{c}} = \frac{3060\ \frac{\mathrm{m}}{\mathrm{s}}}{500\ \mathrm{Hz}} \approx 6.1$ m and $\lambda_\mathrm{soft} \approx 1.4$ m. For a constant tunnel diameter $d = 10$ m, the TS-wave wavelength in hard rock environments is more than half the tunnel diameter, while in soft rock the ratio TS-wave wavelength-to-tunnel-diameter measures in the range of 0.14. Further implications concerning the wavelength-to-tunnel-diameter ratio are explained in Chapter 4. Moreover, the short TS-wave wavelength in soft rocks may be more sensitive to the discretization of the tunnel wall. The imperfect approximation of the tube by the Cartesian grid can ultimately result in scattering artifacts and are subject to further investigations in Chapter 3.3.

The synthetic seismogram sections in Figure 3.5 illustrate the wave simulation in soft rock and hard rock. Early modeling results in soft rock environments with the Cartesian 3-D code showed significant amount of artifacts in terms of signal broadening and large oscillatory tails similar to dispersion effects (Figure 3.4). In order to avoid these artifacts and to safe computational time, the 2.5-D modeling code has been employed. The origin of these artifacts is subject to further investigation in Chapter 3.3. Except of the travel time between the excitation of the direct TS-wave and the TSST-wave back-propagation along the tunnel wall, no significant differences are visible. On closer look, the amplitude ratio of the direct TS-wave and the reflected TSST-wave is larger in the soft rock simulations ($\frac{A_\mathrm{ts-soft}}{A_\mathrm{tsst-soft}} \approx 6.3 > \frac{A_\mathrm{ts-hard}}{A_\mathrm{tsst-hard}} \approx 3.3$). This is due to the smaller Q factor of the model (see parameters in Table 2.1), which implies greater damping of the simulated waves. Thus, in real soft rock formations with similar elastic properties, the observed back-converted TSST-wave amplitude can be expected to be lower than in tunnels through hard rocks. At a constant noise level, the signal-to-noise ratio is consequently lower, too.

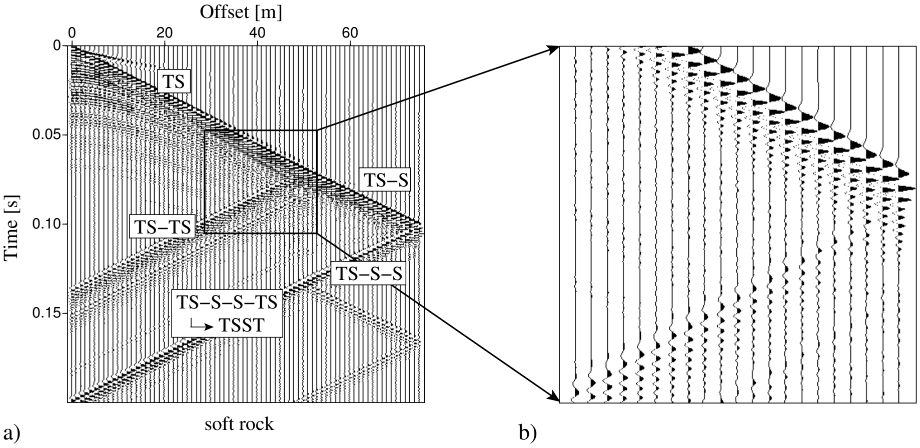

Figure 3.4.: 3-D TSST-wave simulation in a homogeneous soft rock formation illustrating artifacts due to the coarse grid spacing of $dh = 0.1$ m. a) Full seismogram section of receivers close behind the wall of an evacuated tunnel with major wave types labeled. b) Tracewise normalized zoom section of a) scaled with the square of the travel time.

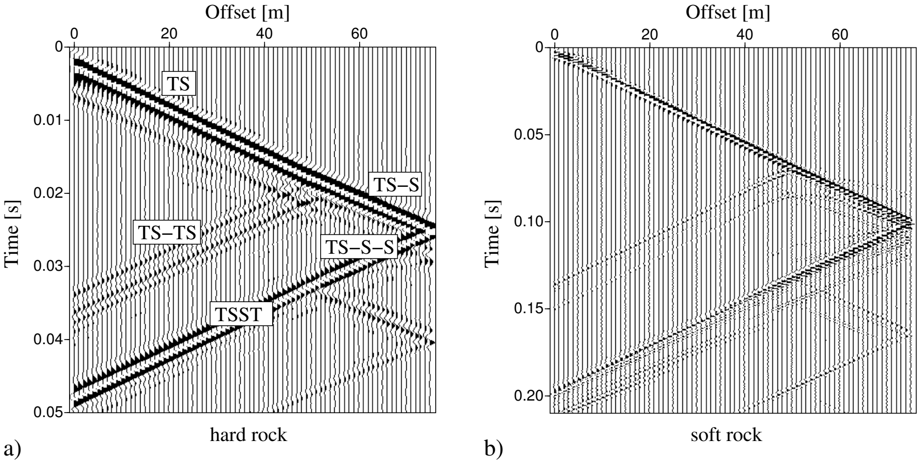

Figure 3.5.: 2.5-D TSST-wave simulation in a homogeneous hard rock (a) and homogeneous soft rock formation (b). Major wave types are labeled. For both models, source and receivers are located at the same side of an evacuated tunnel.

3.3. Spatial discretization of the tunnel

Motivated by the TSST-wave phase drift (Chapter 3.1) and dispersion artifacts observed while modeling the TSST-wave propagation in soft rock, we now investigate the influence of the spatial discretization of the model and especially of the tunnel wall. We therefore focus on the 3-D modeling code *fdmpi* and the excitation and propagation of the TS-wave in a soft rock formation. Model parameters and measurement geometry are kept constant (see Chapter 3.1), only the distance dh between two neighboring grid points and consequently the overall number of grid points is varied. Nevertheless, the absolute model dimensions in terms of meter (e.g., length of tunnel, distance tunnel to reflector) are constant. With the increasing or decreasing grid spacing dh, the discrete time stepping for updating the elastic parameters is adapted to keep the Courant ratio $\frac{dt}{dh}$ constant, too.

Two possible effects arise from the varying dh (under the assumption of a stable FD simulation): grid dispersion and scattering artifacts due to the Cartesian tunnel wall discretization. This is illustrated by a basic discretization comparison in Figure 3.6. At $dh = 0.1$ m spatial discretization, the cross section of the tunnel diameter $d = 10$ m is represented by a grid of 100×100 points. Its cylindrical hull consists of approximately 200 grid points. In other words, there are potentially 200 small edges per circumference that reflect and diffract seismic waves. At a grid spacing of $dh = 0.05$ m, there are 400 edges. At first sight, the seismogram section corresponding to the tunnel models exhibit scattering artifacts due to these tunnel wall edges (e.g., oscillatory tails), which vanish by decreasing the grid distance (increasing the number of grid points per tunnel diameter). Considering the dominant TS-wave wavelength of $\lambda = 1.4$ m (see Chapter 3.2) and the dimension of edges of the tunnel wall at $dh = 0.1$ m, we can introduce the product $k \cdot dh = \frac{2\pi}{\lambda} \cdot dh \approx 0.45$. For $dh = 0.05$ m, $k \cdot dh$ equals approximately 0.22. According to Wu and Aki (1988) the criteria for heterogeneities being to small to interfere with the wave propagation is $k \cdot dh < 0.01$. In our case, we can theoretically expect to observe Rayleigh or Mie scattering ($0.1 < k \cdot dh < 1$) due to the discretization of the tunnel wall. Wijk (2003) showed in both numerical simulations and measurement data that such multiple scattering at small structures along the surface results in similar seismogram sections.

However, in case of a large grid spacing dh in comparison to the occurring wavelength, the coarse grid for the FDTD simulation can cause seismic signals to show properties characteristic of dispersion: delayed, broadened signals and an oscillatory tail (Alford et al., 1974; Virieux, 1986). In contrast to *medium related dispersion* due to model inhomogeneities, which mainly affects surface waves, both surface and body waves can exhibit *grid dispersion*. In order to avoid such dispersion, the shortest dominant body wave wavelength is recommended to be discretized by at least 20 grid points for second order accuracy in space used in the modeling (see Equation 3.2). The spatial discretization $dh = 0.05$ m chosen for the wave simulation according to Figure 3.6 fulfill this discretization criterion (28 grid points per dominant TS-wave wavelength) and still exhibit strong dispersion artifacts. At $dh = 0.01$ m (14 grid points per dominant TS-wave wavelength), the criterion is marginally violated. Bohlen and Saenger (2006) investigated the influence of grid spacing with respect to the correct modeling of surface waves along a plane free surface. It could be shown that surface waves need special discretization care beyond the 20 grid points per wavelength. Even more than 30 grid points are needed (according to the minimum surface wave wavelength, more than 15 grid points are required).

A common way to distinguish grid dispersion from scattering is the comparison of FD data with analytic seismogram sections, which could not be obtained. Therefore, we additionally simulate the wave field using the cylindrical 2.5-D code *fdbh*. With its rotational symmetry regarding the x-axis, the fdbh code does not suffer from any discretization effects along the tunnel wall. It shows dispersion due to the coarse grid spacing, though. Therefore, we can simultaneously vary the grid spacing in both the fdmpi and the fdbh code while keeping the model and acquisition parameters constant. If the scattering caused by the Cartesian tunnel wall discretization is an issue, only the fdmpi seismograms show this effect. In contrast, grid dispersion is traceable in the synthetic seismograms generated by the fdmpi as well as the fdbh code.

The modeled direct TS-waves as a function of the grid spacing are shown in Figure 3.7a (fdmpi) and 3.7b (fdbh). For all chosen discretization dh, the arrival of the tunnel surface wave is constant. However, with larger dh, the signal phases are more delayed, broadened and show an oscillatory tail. The synthetic seismograms from both the 3-D and the 2.5-D code show the same kind of dispersion effects, the oscillatory tail for a constant dh (e.g., $dh = 0.15$ m) is even larger in the fdbh trace. As a quantitative measure for the dispersion effect, we calculate the root mean square (RMS) of the chosen time window, which is the square of the mean surface of a time series. The larger the oscillatory tail, the larger is the RMS. To balance for any scaling with the grid spacing implemented in the modeling codes, we first normalize the seismogram traces to its maximum particle velocity. The RMS calculated from the fdmpi and fdbh seismograms are displayed in Figure 3.7c, and again show the dispersion effect as a function of the spatial discretization. With the decreasing grid distance dh, the RMS decreases as well. In the case of the RMS calculated from the synthetic fdmpi traces, a grid spacing below $dh < 0.05$ m eliminates the dispersion almost completely. As a consequence, refining of dh does not further decrease the RMS value. It is particularly noticeable that according to the RMS as a measure for grid dispersion, the fdmpi code is producing less artifacts. The grid spacing dh_{fdmpi} can be chosen at least 20% larger than dh_{fdbh} to gain a comparable RMS value.

Since both modeling results exhibit the same kind of effect, we can conclude that the dispersion effect is originated by the coarse grid spacing instead of the scattering along the tunnel wall. As it is shown for surface waves along a plane surface, tunnel surface waves modeled by the fdmpi code have to be discretized by at least 28 grid points per dominant TS-wave wavelength ($dh = 0.05$ m at $\lambda_{\mathrm{ts}} = 1.4$ m). The underlying FD scheme implemented in the fdbh code apparently produces stronger numerical dispersion artifacts. The fdbh limit for a stagnating RMS value is about 46 grid points per dominant TS-wave wavelength. The general discretization issue is especially critical for the wave simulations in soft rocks, since the TS-wave wavelength is less than one third of the TS-wave wavelength in hard rock formations. In other words, the spatial discretization has to be chosen to be more than three times smaller for modeling in soft rock formations, which implies additional computational effort. Nevertheless, for our chosen model size of 90×60×60 m used in fdmpi, the minimum grid spacing, which allows a wave simulation on a 64 CPU cluster computer that finishes in a reasonable time (less than a week) is 0.05 m, resulting in a grid of 1800×1200×1200 points. Refining of the model grid in fdbh is less problematic due to its modeling performance considering only two dimensions.

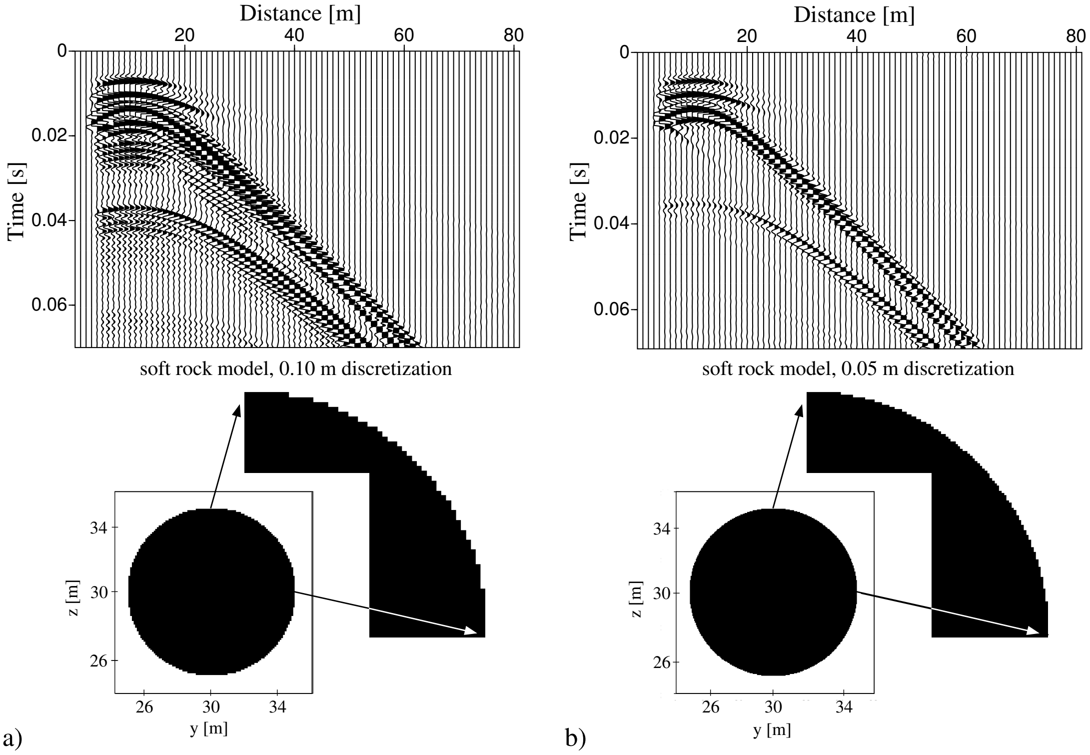

Figure 3.6.: Common-shot gather of a 3-D finite difference modeling according to a soft rock tunnel model below with a spatial discretization of a) 0.1 m (approximately 14 grid points per dominant TS-wave wavelength) and b) 0.05 m (approximately 28 grid points per dominant TS-wave wavelength). Source type, receiver position and component as well as model dimensions are kept constant.

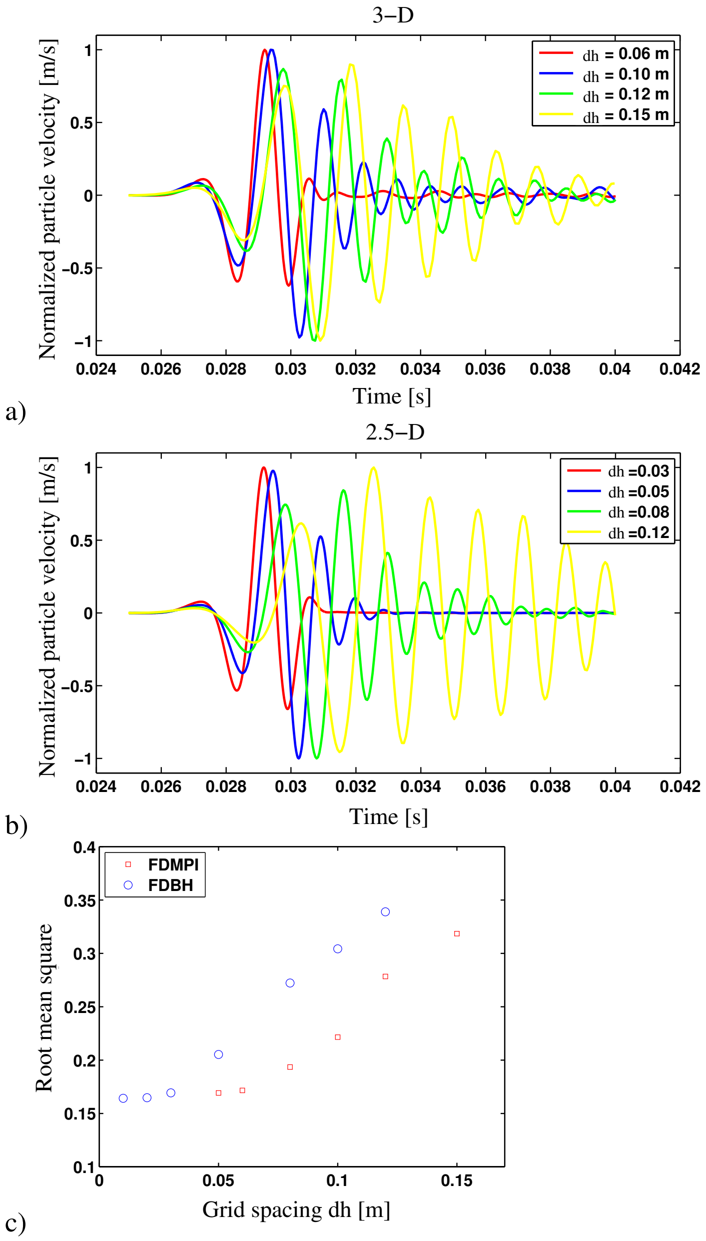

Figure 3.7.: TS-wave dispersion due to the grid spacing dh. The direct TS-wave is plotted for different spatial discretization dh derived from wave simulations by a) the Cartesian 3-D code fdmpi and b) the cylindrical 2.5-D code fdbh. The calculated root mean square (RMS) for all these direct TS-wave signals is shown in c). An explosive ring source behind the tunnel wall is used for all FD modelings.

3.4. Excavation damage zone

In previous chapters, we already introduced numerical *grid dispersion* and quickly referenced *medium related dispersion* due to rock inhomogeneities mostly affecting surface waves. Starting from a free surface, the body wave velocity usually increases gradually. Surface wave contents at higher frequencies have shorter wavelength that do not penetrate much into the formation (off the surface) and therefore travel at the velocity determined by the elastic properties close to the surface. In contrast, wave contents at lower frequencies are characterized by longer wavelength, which penetrate deeper into formation and travel at an integral velocity that is higher than the velocities at the surface. Surface wave propagation in a gradient medium therefore causes different phase velocities as a function of the excitation frequency. In recorded or modeled seismogram sections, we can observe the signal phases drifting apart with its propagation through the gradient medium. Signal broadenings, phases delays and an oscillatory tail are visible, too, which already have been shown in Figure 3.7 for the reason of grid dispersion.

During the tunnel construction, the rock environment around the tunnel is significantly altered. As a consequence, a zone of shattered rock is formed around the excavated tunnel, which is known as the excavation damage zone (EDZ). In the following, we investigate the influence of this zone around the tunnel on the TS-wave propagation. In agreement with common assumptions on the dimension of the EDZ (Schuster et al., 2001; Borm et al., 2003b), the modeled EDZ extends twice the tunnel radius (in our model $r = 5$ m) into the surrounding formation and is approximated by a seismic velocity gradient (see Figure 3.8a). Since we only intend to investigate the wave propagation along the tunnel wall, the evacuated tube (tunnel) extends from both model boundaries. No tunnel face or reflector ahead of the tunnel has been included in the wave simulation model.

To enable comparability with acquired data from a hard rock tunneling site (Lüth et al., 2006), we again focus on a hard rock model with parameters listed in Table 2.1. In order to study the influence of both the P- and S-wave velocity, we apply different gradients to the P- and S-wave model and determine the dispersion curves of the TS-wave gained from the synthetic common-shot gather. All the dispersion curves in Figure 3.8b are plotted in the w vs. $\frac{v_{\mathrm{ts}}}{v_{\mathrm{s}}}$ domain with w is the ratio of wavelength-to-tunnel-diameter. This measure considers the curvature of the tunnel wall surface with respect to the wavelength of the TS-wave and is described in more detail in Chapter 4.1. The dispersion curves for the following scenarios are calculated from the cross power spectrum of two neighboring seismogram traces after transformation to the frequency domain (Rosenblad et al., 2006):

- no gradient in either the P- and S-wave velocity model (red circles),
- a gradient in the P-wave velocity model only (there is a linear velocity decrease of 20% of the formation P-wave velocity toward the tunnel surface), no gradient in the S-wave velocity model (red triangles),
- a gradient in the S-wave velocity model only (there is a linear velocity decrease of 20% of the formation S-wave velocity toward the tunnel surface), no gradient in the P-wave velocity model (blue triangles),
- gradient in both the P- and S-wave velocity model (there is a linear velocity decrease of 20% of the formation P- and S-wave velocity toward the tunnel surface) (blue circles),
- gradient in both the P- and S-wave velocity model (there is a linear velocity decrease of 6% of the formation P- and S-wave velocity toward the tunnel surface) (empty circles),

- Piora data section for future reference in Chapter 4.2 (crosses),
- additionally the analytic dispersion curve with $\nu = 0.4$ from Figure 4.3 is plotted for future reference (black line).

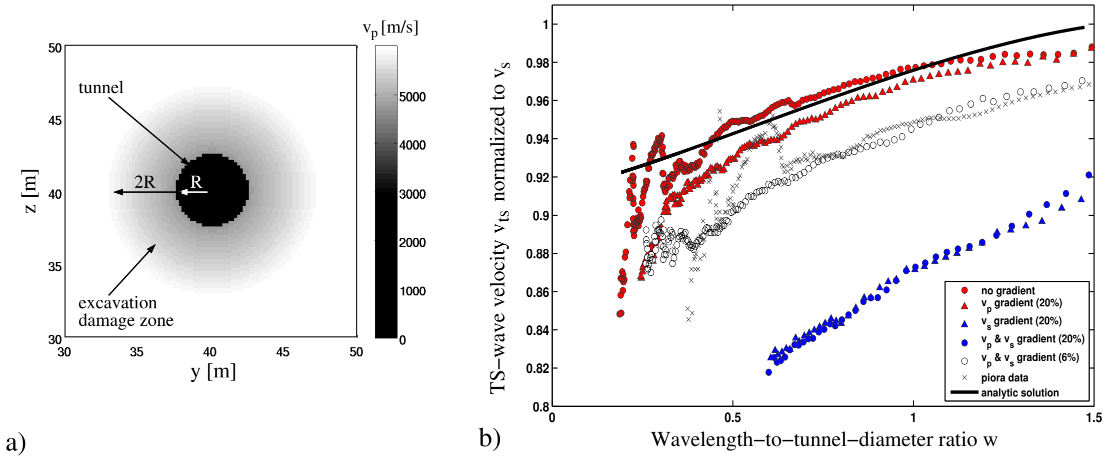

Figure 3.8.: a) Slice of an 3-D excavation damage zone model with a linear increase in the seismic velocities off the tunnel wall. The cross section of the tunnel and the dimension of the EDZ are illustrated. b) Fundamental modes of the dispersion spectrum is plotted for different excavation damage zone models, the Piora field data and the analytic solution. The Piora curve (crosses) and the analytic solution (black line) have been inserted for future reference in Chapter 4.1 and 4.2. All dispersion curves calculated from the FD data differ by the underlying gradient in the elastic properties away from the tunnel wall.

From Figure 3.8b we see that all gradient scenarios - even no gradient in the velocity field - cause the TS-waves to be dispersive. In addition to the gradient or medium related dispersion, there has to be another process that controls the wave dispersion, which is subject to further investigation in Chapter 4. On the other hand and even though TS-waves - like other surface - show characteristics of both shear and compressional waves, the disperse behavior is dominated by the gradient in the shear wave velocity. There is no significant difference according to the dispersion curve, if we model a strong gradient in only the v_p field and no gradient at all (Figure 3.8b: red circles vs. red triangles). Obviously, the dispersion characteristics scale only with the shear wave gradient. However, we should keep in mind that a gradient in the P-wave velocity field usually goes along with a gradient in the S-wave velocity model. Our case is basically of theoretical nature. A tomographic survey conducted in the Piora adit close to Gotthard Base Tunnel, Switzerland (Borm et al., 2003b), indicates a gradient in both the v_p and v_s field. Most other investigations on the properties of an EDZ are limited to first arrival (P-wave) measurements.

3.5. Lining of the tunnel wall

The tunneling trough hard rock formations has significant advantages for the prediction ahead of the tunnel using tunnel surface waves. First, the tunnel wall is stable by itself and does not need immediate support in terms of shotcrete or lining (see Chapter 1.1). A direct geological mapping of the tunnel wall is therefore possible and enables an in-situ confirmation of predicted structures or rock formations. Second, mounting the source and receiver to the tunnel wall is fairly simple. The pneumatic hammer source can be directly applied to the tunnel wall, which can improve the coupling conditions. The receivers are mounted on rock anchors up to two meters behind the tunnel wall in order to avoid scattering artifacts due to small cracks as a product of the tunneling. At the same time, the influence of the excavation damage zone as described in the previous chapter is reduced.

However, in soft rock environments, the tunnel face as well as the tunnel wall requires immediate stabilization. The TBM's drivetrain is thus surrounded by a steel tube (shield) that provides support for brittle or unstable rocks. Following the shielding, the lining is assembled by pre-casted concrete rings and tubing segments, respectively. Mortar is squeezed in the gap between tunnel wall and tubing as a backfilling, which seals the tunnel wall from any formation water leakage. Both the tubing and the mortar acts as a protecting shell for the tunnel tube. Altering its integrity by drilling a hole through the tubing for placing the receiver anchors or applying the hammer source on top of the tubing ring surface may cause instabilities or future pathways for water leakage. Fortunately, the concrete tubing segments bear small maintenance holes, which do not pass through the segment completely. With a modification of the receiver housing, the seismic sensors can be screwed in these holes. Additional measurements of the concrete integrity after hammer impacts have been conducted and reveal no significant damage even after 10 or more hammer blows. Nevertheless, both the coupling conditions and the seismic wave propagation in general change due to the altered measurement layout.

Under the assumption of the complete filling of the gap between tunnel wall and tubing, we can expect to observe following effects with its implications:.

- Instead of the direct excitation of body and tunnel surface waves into the rock formation, the wave energy excited by the hammer impact is split at each material boundary (concrete - mortar, mortar - rock). Especially at short wavelength, reflection and wave conversion occurs.
- With its seismic properties listed in Table 3.1, both the mortar and the tubing layer act as a high velocity layer. In conjunction with a simulated EDZ gradient, there is even a low velocity zone framed by higher seismic velocities of the lining and the EDZ. At small wavelength, additional seismic waves are generated (both body and additional surface waves) that propagate within the fast concrete ring.
- Finally, the internal structure of the tubing segments (the grid of the steel reinforcement within the concrete) scatters waves that pass through or propagate along the tunnel wall. The mortar shell can be treated as a homogeneous layer. In the case of imperfect backfilling (open cracks, air pockets), the coupling conditions for both the seismic source and receiver decrease. Coupling is a serious issue, if ultimately, only little wave energy passes the lining. Scattering and wave field splitting may only affect the high frequency wave content (short wavelengths).

parameter	tunnel	soft rock	lining (concrete\steel)	mortar
ρ [kg/m^3]	1.25	1200.0	2300.0\7700.0	2000.0
v_p [m/s]	0.0	2000.0	4000.0\5800.0	3000.0
v_s [m/s]	10^{-6}	800.0	2300.0\3300.0	1700.0
Q_p	∞	100.0	500.0\500.0	500.0
Q_s	∞	100.0	500.0\500.0	500.0
thickness	5 m (radius)	∞	0.5 m	0.3 m

Table 3.1.: Material properties used in the simulation of the TSST-wave look-ahead prediction in soft rock in the presence of a lining with steel re-enforced concrete rings and a mortar backfilling: Given are the values of density ρ, the seismic velocities v_p and v_s, and the quality factors Q_p and Q_s for compressional waves (P-waves) and shear waves (S-waves), respectively.

Since the source position is slowly moving at TBM speed, there is no option beside applying the hammer source on top of the tubing segment. In contrast, it is theoretically possible to drill through the tubing, place the receiver anchor and seal the hole afterwards. If modeling results suggest a significant improve in the TS-wave recording behind the concrete lining, field measurements might consider this option. Our common model for the wave simulation (evacuated tunnel within a homogeneous full space) is extended by a concrete and mortar between the lining and the soft rock formation. The material parameters are listed in Table 3.1. As an example, the 1-D P-wave velocity (v_p) profiles for the model scenarios considered are drawn in Figure 3.9. The receiver line is always placed on top of the tubing. A point force normal to the surface is used to excite the dispersion spectrum.

The modeling of the seismic response in presence of the lining elements turns out to be difficult due to the construction of the model. Especially the discretization of the steel re-inforcement inside the concrete tubing segments meets computational limits. From Chapter 3.3 it follows that the minimum grid spacing for a soft rock model characterized by material parameters listed in Table 3.1 should be at least 0.05 m. Furthermore, a steel beam as part of the armor mesh has to consist of at least two grid points for numerical reasons. This sums up to a minimum reinforcement structure size of 10 cm, which is not realistic. However, we have also shown that numerical dispersion is rather an issue than wave scattering caused by sharp material edges due to the Cartesian discretization. We therefore neglect the steel reinforcement and focus on the additional layers of concrete and mortar on the inside of the tunnel.

In Chapter 3.4, we have investigated the influence of the excavation damaging zone (EDZ) by applying a gradient in the formation properties away from the tunnel wall. From the modeled seismogram sections we calculated the dispersion curves, which showed the tunnel surface wave velocity against its frequency. Since we can assume the additional concrete and mortar layers to influence the effective dispersion properties of the TS-waves, we may as well calculate the dispersion curves directly. This can be performed by, e.g., a wave number integration algorithm that computes Greens functions according to a 1-D model with variable layers. After convolution with the source signal, we can obtain the system response of the specified model, i.e., the dispersion spectrum. This semi-analytical method has been introduced by

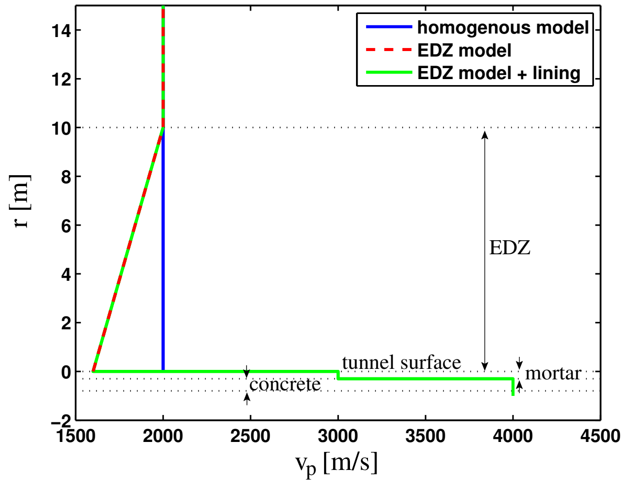

Figure 3.9.: The 1-D v_p profile illustrates the compressional wave velocities listed in Table 3.1 for three different tunnel model scenarios: a homogeneous formation (blue line), an excavation damage zone surrounding the tunnel (red, dashed line) and a tunnel wall covered by lining and an excavation damage zone surrounding the tunnel (green line).

Wang (1999) and is implemented in a program called *qseisfk*. If we are mainly interested in the dispersion spectrum and a 1-D model response approximates our 3-D tunnel surface wave excitation, it is then reasonable to use qseisfk instead of fdmpi and saves computational time. A qseisfk run takes less than a minute on a single CPU, a similar finite difference modeling consumes at least a day of computational time on a 64 CPU cluster!

In order to compare the TS-wave dispersion properties in 1-D (qseisfk) and 3-D (fdmpi), we first calculate the phase velocity against the frequency from a 3-D FD seismogram section according to a homogeneous soft rock model with a spatial discretization of $dh = 0.05$ m. We simply reuse the fdmpi wave simulation results from Chapter 3.3 using an explosive ring source excitation where we extracted only a single trace to estimate the grid dispersion with respect to grid spacing (Figure 3.7). Again, the TS-wave dispersion curve is calculated from the cross power spectrum of two neighboring seismogram traces after transformation to the frequency domain (Rosenblad et al., 2006). We now plot this curve on top of the dispersion spectrum calculated by qseisfk according to a homogeneous model (see Figure 3.9, blue line). As we can see from Figure 3.10a, both dispersion curves follow a straight line more or less parallel to the frequency axis, i.e., the phase velocity does not depend significantly on the excitation frequency, which is natural for surface wave excited in a homogeneous medium. However, the 3-D TS-wave (red triangles) is slightly dispersive, which has been shown in Chapter 3.4, Figure 3.8b. For an explanation of this *tunnel related dispersion*, we refer to Chapter 4. Nevertheless, except for the small differences in phase velocity at low frequency, we can suppose that the main dispersion properties are sufficiently described by both the 1-D modeling by qseisfk and the 3-D results gained from finite difference modeling. We therefore proceed investigating the influence of the lining elements by dispersion spectra gained from qseisfk. Please note that with the neglect of the curvature of the tunnel in the 1-D model, we now - strictly speaking - model surface waves rather than tunnel surface waves. Still, we use the term TS-wave in the following, since we can assume that, except for the tunnel related dispersion, the TS-wave dispersion properties are very similar to the surface wave dispersion.

In order to show the transition of the model response from the homogeneous model to the more complicated system covering the lining and an EDZ gradient, we introduce an intermediate step. We first run a qseisfk model with only an EDZ gradient in formation velocities as described in Chapter 3.4 - with the difference of a soft rock formation (see Figure 3.9, red dashed line). The corresponding dispersion spectrum is displayed in 3.10b. Similar to Figure 3.8b and the dispersion spectrum in Bohlen et al. (2007) we observe TS-wave fundamental mode velocities close to the S-wave velocity at long wavelength and low frequencies, respectively. With the increasing excitation frequency and thus smaller wavelength, the TS-wave velocity approaches the surface wave velocity of approximately 0.94 times the S-wave velocity, which is typical for surface waves (Ingard, 1988). Also, higher modes are visible. As done for the homogeneous soft rock model, we additionally plot the dispersion curve computed from synthetic FD seismograms. We again use the same model size, source and receiver geometry and excitation frequency as described in Chapter 3.1 with an additional gradient in the seismic velocity and the density field of 20%. The dispersion curve calculated by the 3-D FD simulation matches well with the qseisfk dispersion spectrum.

Finally, we can have a look at the dispersion response in Figure 3.10c according to a soft rock model including an EDZ gradient and both a concrete and mortar layer covering the surface (see Figure 3.9, green line). Clearly, the dispersion properties are quite different to the previous model responses. The fundamental mode is traceable in only a small frequency range. In contrast, at least one of the higher modes span a wide frequency range with phase velocities above the formation S-wave velocity. Obviously, the TS-wave fundamental mode is strongly limited by the system of lining and excavation damage zone. Only long wavelengths are excited that penetrate into the undisturbed formation and travel with velocities ranging from the typical surface wave velocity to formation S-wave velocity. At higher excitation frequencies only weaker higher modes are excited, which travel with a phase velocity dominated by the concrete and mortar layer. For wavelength smaller than 1 m (source frequencies above approximately 2000 Hz), the excited surface waves propagate within the lining only. In between, a transition of phase velocity from formation S-wave to an integral lining S-wave velocity of roughly $2000\ \frac{\mathrm{m}}{\mathrm{s}} \approx \frac{0.5\ \mathrm{m}}{0.8\ \mathrm{m}} \cdot 2300\ \frac{\mathrm{m}}{\mathrm{s}} + \frac{0.3\ \mathrm{m}}{0.8\ \mathrm{m}} \cdot 1700\ \frac{\mathrm{m}}{\mathrm{s}}$ can be observed. In both cases, the excited TS-wave energy is low. The system of lining and EDZ can be thus treated as an effective low pass filter. It selects wave frequencies significantly below the chosen source center frequency (in our case $f_c = 500$ Hz).

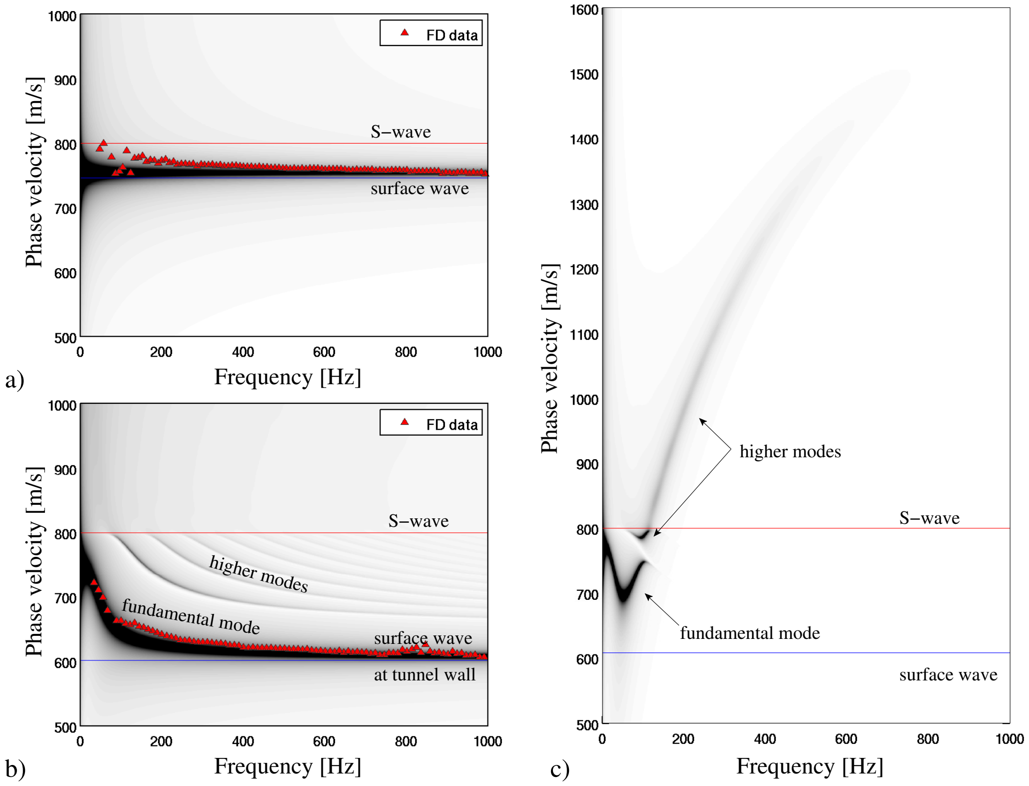

Figure 3.10.: Surface wave dispersion spectra (by qseisfk, 1-D layer model) and dispersion curves (by fdmpi, 3-D tunnel model, red triangles) according to a) a homogeneous soft rock half space model with properties listed in Table 3.1; b) a soft rock half space model with a simulated EDZ gradient similar to 3.8a (the elastic properties ranges from 80% at the tunnel wall to 100% of the values listed in Table 3.1); c) soft rock half space model with a simulated EDZ gradient and steel reinforced lining covering the tunnel wall. The remaining space between the lining and the tunnel wall is filled with mortar. The material properties are again listed in Table 3.1. In all subplots, the S-wave (red line) and surface wave velocity of approximately 0.94 times the S-wave velocity (blue line) are highlighted. The 1-D v_p profiles for all three models are displayed in Figure 3.9

3.6. Chapter conclusions

The numerical simulation of tunnel surface waves is a powerful tool to understand the TS-wave characteristics under various conditions around the tunnel. This way, we can run tests and study synthetic cases before going underground and acquire field data. Beforehand of such costly field measurements, we can optimize our acquisition parameters and geometry, and can focus on desired effects. On the other hand, as we have seen from the previous chapters, the modeling of wave propagation effects is not trivial either. Naturally, the overall goal of modeling is to safe computational time without trading off for too many neglected propagation effects. Hence, the method of choice for seismic wave simulation is always the modeling with the fewest degrees in the model space. If the simplest modeling scheme does not consider the properties or dimensions essential for the modeling of the desired problem, we have to move on by employing a more sophisticated modeling approach.

Based on the previous chapters on the modeling of tunnel effects, we separate the following implications. We first draw conclusions derived from synthetic case studies independently of the chosen modeling code and approach, respectively:

- By simulating a discrete number of point sources applied at the tunnel wall we can create a sufficiently accurate ring source. Thus, we can directly compare the modeling results gained from the 2.5-D and the 3-D modeling code. However, the total excited wave energy scales with the number of sources, which consequently has to be normalized.
- A coarse spatial discretization (large grid spacing) can cause significant numerical artifacts (numerical dispersion). Similar to Rayleigh surface waves, the dominant wavelength of tunnel surface waves occurring in a finite difference wave simulation by fdmpi has to be discretized by at least 28 grid points. This implies large computational effort when modeling the TS-wave propagation in complex models. For this reason, the FD modeling of the TS-wave is more consuming in soft rock formations because of a shorter wavelength.
- If the grid spacing is small enough to avoid numerical dispersion, the scattering due to Cartesian tunnel wall discretization can be neglected. That means, the structure size of potential scatters is then small in comparison to the TS-wave wavelength.
- Every kind of tunneling (both mechanical and conventional tunneling) changes the surrounding rock properties due to the physical impact of the driving. The so called excavation damage zone (EDZ) can be described by a decrease in the seismic velocities and density of up to 20% at the tunnel wall. Gradually, the formation properties approach the undisturbed rock properties after approximately two times the tunnel radius. This causes the TS-wave to exhibit medium related dispersion. Nevertheless, the tunnel surface wave dispersion is dominated by the gradient in the shear wave velocity field. If for some reason, the compressional velocity field is mainly altered by the tunneling, the TS-waves are less effected.
- In addition to the medium related dispersion caused by the EDZ, tunnel related dispersion can be observed, which is investigated in detail in Chapter 4.
- The lining of the tunnel wall in soft rock formations represents a low pass filter and seriously limits the excited frequency range. As a consequence, the system of the concrete elements, mortar and the EDZ gradient effectively damps shorter wavelength. Mostly long wavelength are excited when applying the source on top of the lining element. Since the system response is determined by the lining and the EDZ and the source position is

on top of the lining, varying the receiver position will not considerably change the excited TS-wave spectrum. Relocating the receivers behind the tunnel wall (by receiver anchors) will suppress the recording of the high frequency content. The narrow frequency band of TS-waves traveling in the formation remains.

Depending on the specific problems that have been investigated, we can now give some recommendation for modeling of tunnel surface waves with respect to model space dimensions considered and the corresponding modeling codes. Generally, 3-D wave simulation codes are superior with regard to flexibility facing various problems and model scenarios. Otherwise, the consumption of computational resources is severe, too. With unlimited computer power we could have simulated all previous studies with only the fdmpi code. However, in order to adapt for specific modeling aims and safe resources, we can briefly describe the following limitations regarding modeling codes used in this work with respect to the modeling of the tunnel surface wave propagation:

- 1-D qseis (outputs semi-analytical seismograms) and qseisfk (outputs semi-analytical dispersion spectra): Without taking lateral inhomogeneities along the tunnel wall into account, the model based on the 1-D velocity profile is sufficient to produce qualitatively correct dispersion curves of TS-waves. This way, we only neglect the geometrical spreading and the tunnel related dispersion. Since the medium related dispersion is overpowering the tunnel related dispersion in the presence of a significantly large EDZ gradient, this neglect appears to be reasonable.
- 2-D fdveps: Due to the modeling of plane layers, TS-waves simulated by fdveps do not exhibit tunnel related dispersion, too. Nor does the code account for the 3-D geometrical spreading. Nevertheless, with the availability of the 2.5-D code fdbh, the fdveps code is obsolete for the modeling of tunnel surface waves. At the same computational effort, fdbh produces a physically correct propagation of TS-waves around a tunnel tube in a 3-D volume.
- 2.5-D fdbh: If we are mainly interested in the simulation of tunnel surface wave in various media without an angular-dependency in the formation properties, fdbh is the ideal modeling code due to its low computational requirements. However, we have to respect its radial rotational symmetry. Especially point sources turn into ring sources, which implies the absence of circulating TS-waves around the tunnel. Also, the possibility of simulating the effect of time-delayed point sources on the radiation pattern at the tunnel face is difficult to realize. Furthermore, there are limitations concerning the design of the model because there are plane interfaces only orthogonal to the symmetry axis. Apart from this, the numerical dispersion in fdbh is stronger than for the 3-D modeling code fdmpi. In order to tolerate the same amount of grid dispersion in fdbh and fdmpi, we have to decrease the grid spacing by up to 60% in the 2.5-D modeling code. Nevertheless, the overall computational time of fdbh is still shorter by orders of magnitude.
- 3-D fdmpi: This simulation code suffers only from its computational costs and the Cartesian discretization that produces aliasing artifacts when we discretize non-planar, e.g., curved structures. However, for the tubing case, we have shown that we do not observe significant scattering or reflection due to the sawtooth surface of the tunnel wall. For a very fine model grid, we can most accurately model the propagation of waves in isotrop, viscoelastic media with respect to the presented look-ahead prediction scheme using tunnel surface waves.

Naturally, this chapter does not and cannot cover all available modeling methods to simulate the wave field around a tunnel. In this work, we mainly focus on finite difference (FD) methods. However, there are at least two other modeling approaches that have proven their ability to generate tunnel seismic data, which have not been tested within this thesis. First, the discontinuous Galerkin (DG) method was initially introduced by Reed and Hill (1973) to solve the neutron transport equation. Later on, this modeling scheme was applied to wave propagation problems, too (de la Puente et al., 2008). The main advantages of this method are the unstructured grid and the locally independency of the resulting equations, i.e., the solution within each element does not depend on neighboring elements (Qiu et al., 2006). Therefore, grid boundaries and discontinuous interfaces within the model do not need special treatment. Also, DG schemes can be parallelized reasonably well. Second, the spectral finite element modeling (SFEM) method is a special (high order) case of the FEM method that combines the generality of the finite element method (unstructured grid) with the accuracy of spectral techniques (excellent error properties, fastest convergence) (Patera, 1984; Gopalakrishnan et al., 2008). A recent study showed this potential modeling method to simulate seismic waves around a tunnel (Lamprecht, 2010). Nevertheless, the parallel SFEM implementation to cluster computer platforms is usually complex. In contrast, the finite difference modeling schemes are well established, researched over decades and comparatively easily to parallelize.

CHAPTER IV

Propagation characteristics of TSST-waves

Infrastructure construction in urban areas and larger traffic development projects more often involve tunnel drilling. Surface measurements provide general geological information about the ground, but often the acquired data resolution is not sufficient to identify lithological boundaries like weak or water bearing zones or other geological features like erratic blocks, hampering failure-free tunnel construction operation. Even if perturbing geological formations are detected, there are uncertainties regarding the exact distance to the tunnel boring machine. This lack of geological knowledge can cause safety risks and downtimes of the tunnel boring machine, decreasing efficiency and increasing construction costs. To prevent financial and safety risk, geophysical exploration ahead of a tunnel can be a valuable tool.

Recently, we introduced a new seismic prediction strategy using tunnel surface waves (Bohlen et al., 2007). Figure 4.1 illustrates the wave paths. Tunnel surface waves (TS-waves) are excited by a vibrator or pneumatic hammer. They travel along and around the tunnel in the direction of the working front. There, TS-waves are converted into body waves (preferentially S-waves) at the tunnel edges. In the presence of a fault zone or other geological heterogeneities ahead of the tunnel, these body waves are reflected and couple back in as TS-waves when reaching the tunnel face. The reflected and back-converted TS-waves are then recorded by geophones along the tunnel wall. The determination of TS-wave travel time and continuous measurements during the drilling progresses provide information about the distance between the tunnel front and fault zone as well as the spatial location of lithological boundaries.

The essence of the seismic look-ahead prediction method for tunnel construction is the excitation of TS-waves and their conversion into body waves at the working front. This approach has considerable advantages, already described in Chapter 2 and eventually improves the signal-to-noise ratio of reflection events. Nevertheless, it has to be taken into account that the surface waves propagation is primarily considered to be at plane interfaces. In most geophysical applications, the wavelength of the excited surface waves is significantly smaller than the curvature of the surface, which then may not be perceived as such. However, at longer wavelength, the curvature of the surface can affect the propagation characteristics (Jin et al., 2005). A fairly simple comparison of finite difference (FD) modeling data illustrates the difference between surface waves excited at a planar interface and at a extremely curved surface: the tunnel wall. We use a homogeneous model with an evacuated tunnel and a model with an evacuated planar layer bisecting the homogeneous space. For both models, we kept the material parameters the

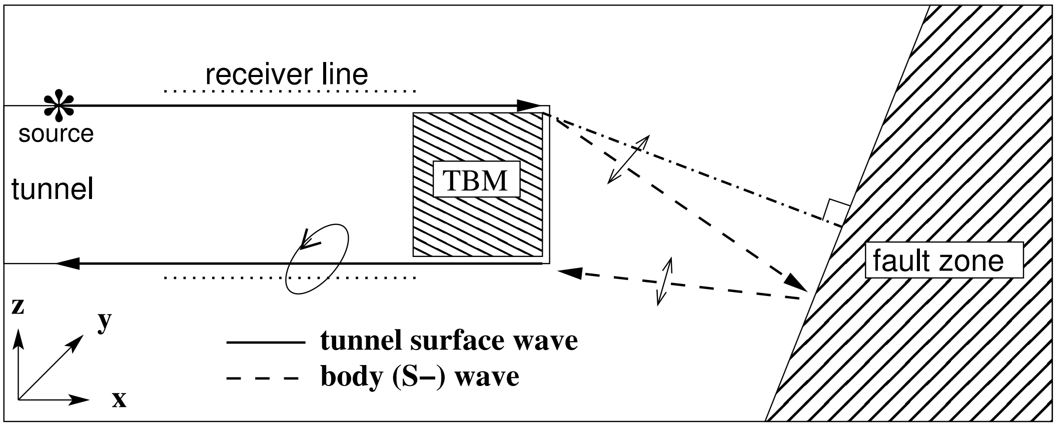

Figure 4.1.: Wavepath of the tunnel surface wave to S-wave conversion at the tunnel front, which acts as a secondary source emitting mainly S-waves. Being reflected at lithological boundaries, these S-waves are converted back into tunnel surface waves and can be recorded by receiver lines mounted at the tunnel wall (modified from Bohlen et al., 2007).

same and applied a low frequency single force source in z-direction (depth) at the bottom of the tunnel or layer, respectively. The common-source gathers (CSGs) are displayed in Figure 4.2 (S-wave component), dominant waves are labeled. Along the planar surface we observe an S-wave and a Rayleigh wave, which is significantly slower than the S-wave. In contrast, the common-source gather along the tunnel surface shows no clear S-wave but a direct TS-wave with a velocity larger than the Rayleigh wave and smaller than the S-wave velocity. At a higher source frequency, the wave field along a planar surface and a tunnel surface shows more similarities (Bohlen et al., 2007, Figure 9).

In the following, we investigate the influence of wavelength on the TS-wave propagation velocity (dispersion) and particle motion (polarization). This is performed by means of an analytic solution for an empty tube in a homogeneous host rock (Stielke, 1959) and by numerical simulations using the 3-D finite difference time domain (FDTD) method (Bohlen, 2002). Understanding these propagation characteristics is a prerequisite for developing efficient processing and imaging methods for seismic look-ahead prediction in a tunnel. First, we describe the analytical solutions and numerical modeling techniques used for analyzing the propagation characteristics of TS-waves. Later on, we compare the simulation results with field data acquired in the Piora adit (Gotthard Base Tunnel, Switzerland).

4.1. Modeling of tunnel surface waves

To investigate the propagation characteristics of tunnel surface waves (TS-waves) we use both an analytical solution on the basis of a Ph.D. thesis by Gerd Stielke (Stielke, 1959) and results of finite difference modeling calculations. The Ph.D. thesis of Stielke (1959) is only available in German language and of limited accessibility. We therefore describe the equations used here in Appendix A for convenience. Even though the underlying model and model-parameters for both methods are almost identical, there are considerable differences handling the analyt-

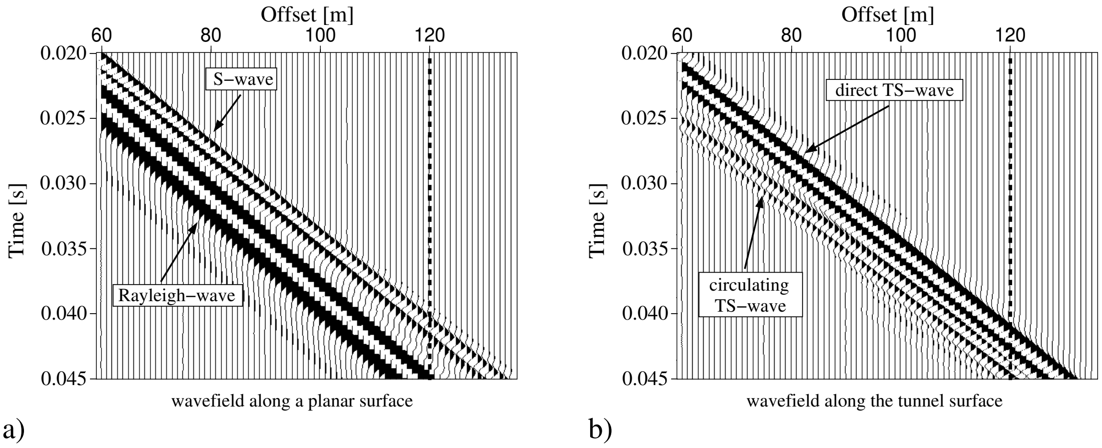

Figure 4.2.: Synthetic common-source gather (S-wave component) of a) a homogeneous model with an evacuated plane layer instead of a tunnel and b) a homogeneous model with an evacuated tunnel. Black arrows indicate the dominant wave types. The force source and receivers for both models are placed at the bottom of the evacuated layer, or tunnel, respectively.

ical solution and the finite difference modeling results. The analytical solution describes the surface wave propagation in cylindrical coordinates (see Figure 2.1b) around an empty tube within a homogeneous full space with different multipole source orders (e.g., monopole, dipole). Therefore, we can quickly calculate the velocity and amplitude vector of a circularly symmetric TS-wave at the point of excitation directly at the tunnel wall for specific source frequencies. In contrast, using the 3-D finite difference method, we can model the propagation of TS-waves excited by a single force source in Cartesian coordinates along the tunnel with arbitrary offsets and distance to the tunnel wall (Figure 2.1a). Because of the helical ray path, this excited TS-wave is therefore not circularly symmetric. Since the calculation effort for the finite difference simulation is significantly greater than for the analytical solution, we can analytically describe the TS-wave propagation for a broad range of source frequencies, while calculating the finite difference modeling response for only a few selected source center frequencies.

We used two basic models consisting of a homogeneous full space with a tunnel diameter of 5 m and differing in their seismic velocity ratios according to Table 2.1: $\frac{v_{\mathrm{p1}}}{v_{\mathrm{s1}}} = \frac{5100\,\frac{\mathrm{m}}{\mathrm{s}}}{3100\,\frac{\mathrm{m}}{\mathrm{s}}} = 1.6$ (Poisson‘s ratio $\nu = 0.2$) and $\frac{v_{\mathrm{p2}}}{v_{\mathrm{s2}}} = \frac{2000\,\frac{\mathrm{m}}{\mathrm{s}}}{800\,\frac{\mathrm{m}}{\mathrm{s}}} = 2.5$ (Poisson‘s ratio $\nu = 0.4$). First, we focus on the analytical modeling and the solution of dispersion relations using equation A1. We obtain the phase-velocity of the tunnel surface wave v_{ts} as a function of frequency and for the two basic velocity models. Instead of plotting the frequency f, we introduce the wavelength-to-tunnel-diameter ratio w, which is calculated by

$$w = \frac{\lambda}{d} = \frac{\lambda}{2\,r} = \frac{v_{\mathrm{ts}}}{2\,r\,f}\ , \tag{4.1}$$

where d denotes the tunnel diameter, r the tunnel radius and v_{ts} the TS-wave velocity. The variable w characterizes both the propagation velocity and the excitation of TS-waves as can be seen in Appendix A. The resulting dispersion curves of the TS-waves for both Poisson’s ratios are displayed in Figure 4.3 where the TS-wave phase velocity - normalized to S-wave velocity - is plotted against the wavelength-to-tunnel-diameter ratio w. Here, we use a circularly symmetric

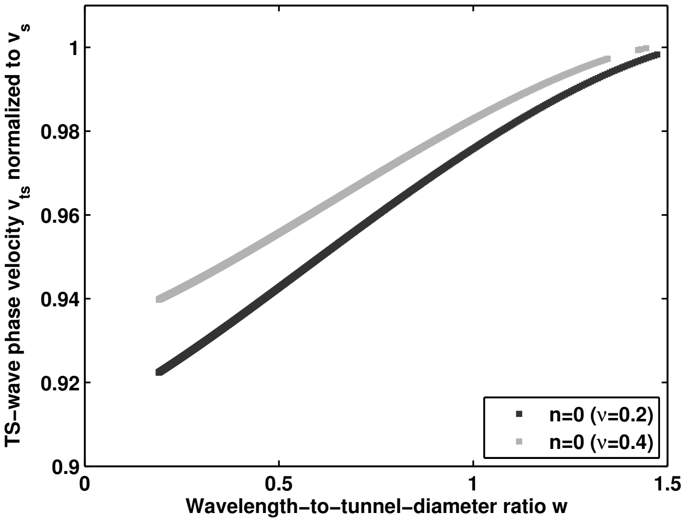

Figure 4.3.: Analytic dispersion curve of the tunnel surface wave for monopole excitation (Hankel order $n = 0$) and two different formation Poisson's ratios. The dispersion curves are plotted at the source location and directly at the gaseous-solid interface (tunnel wall).

force source excitation normal to the tunnel wall (monopole ring source). This is represented by the source, respectively, Hankel function of order zero (see derivation in Appendix A, equation A1-A3). Due to limitations of solving the nonlinear equation A1, the dispersion curve is only plotted in the range $0.2 < w < 1.5$. Also note that only the fundamental mode is displayed. No higher modes are described by the analytic solution because mostly the fundamental mode is observed in tunnel seismic data.

From Figure 4.3 we see that at a small wavelength-to-tunnel-diameter ratio $w < 0.6$ the tunnel surface wave phase velocity is below 0.95 and 0.96 times the S-wave velocity in the case of $\nu = 0.2$ and 0.4, respectively. This is typical for Rayleigh waves (Ingard, 1988; Sheriff and Geldart, 1983). However, with increasing w, the tunnel surface wave velocity converges to the formation S-wave velocity. To give a quantitative measure, an increase of $w = 1.0 \rightarrow 1.5$ results in a TS-wave velocity increase of about $2.5\% \approx 80\ \frac{\mathrm{m}}{\mathrm{s}}$. That means, for $w > 1.2$, TS-waves and S-waves have similar propagation velocities. In order to analyze the excitation of tunnel surface waves, the excitation amplitude A is calculated using equation A3 to determine whether surface waves bear significant amplitudes when their velocity is converging to S-wave velocity.

The TS-wave amplitudes for the radial (A_r) and longitudinal components (A_x) of the excitation vector A as a function of w are displayed in Figure 4.4. Since a ring source is used (see Figure 2.1), there is no ϕ-dependence and $A_\phi = 0$. At small w we observe high amplitudes for both components with $A_\mathrm{r} > A_\mathrm{x}$. This is characteristic for Rayleigh waves (Aki and Richards, 1980; Junge et al., 2006). Increasing w causes a decrease in the amplitude in radial and longitudinal direction with convergence to zero, e.g., the maximum radial component (A_r) at $w = 1.0$ is almost double the maximum radial component at $w = 1.5$. At the same time when $w > 1.2$, the TS-velocity approaches S-wave velocity (Figure 4.3) and the amplitude plots imply that

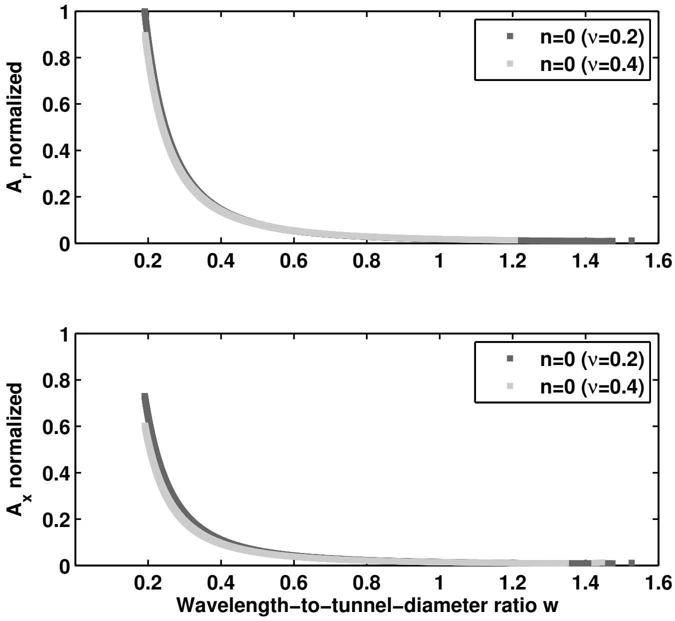

Figure 4.4.: Normalized amplitude vector A of the tunnel surface wave for monopole excitation (Hankel order $n = 0$) and two different formation Poisson's ratios. A_r and A_x denotes radial and longitudinal component, respectively (see Figure 2.1). The amplitude curves are plotted at the source location and directly at the gaseous-solid interface (tunnel wall).

$A_\mathrm{r} = A_\mathrm{x} \rightarrow 0$ and $A_\phi = 0$. Thus, the analytic solution predicts typical Rayleigh waves for small $w < 0.6$ and low amplitude surface waves with almost S-wave velocity for $w > 1.2$ that contribute to body S-wave generated by the force sources. In between, TS-waves are composed of Rayleigh waves and S-waves.

In order to study TS-waves generated by distinct point forces (Figure 2.1a), we use a parallel 3-D viscoelastic finite difference seismic modeling program (Bohlen, 2002). We analyze the propagation of TS-waves for a typical hard rock model with $\frac{v_{\mathrm{p1}}}{v_{\mathrm{s1}}} = \frac{5100\frac{\mathrm{m}}{\mathrm{s}}}{3100\frac{\mathrm{m}}{\mathrm{s}}} = 1.6$ (Poisson's ratio $\nu = 0.2$). Since we use a homogeneous full space (without an excavation damage zone, see Chapter 3.4), we do not observe *medium related dispersion* effects caused by the frequency dependent penetration. However, we have *tunnel related dispersion* due to the relation of tunnel diameter and wavelength of the TS-wave (see Chapter 3.4 and 3.5). With respect to the TS-wave velocity increase described above, tunnel related dispersion is less effective than medium related dispersion in most tunnel environments (Lüth et al., 2006; Malmgreen et al., 2007; Bohlen et al., 2007).

We model TS-waves excited by a single force source applied at one side of the tunnel wall and record the particle velocities (offset range 21-55 m) at the same side (identical azimuth). We thus simulate a straight line geometry. The broadband TS-waves are excited with a source center frequency $f_\mathrm{c} = 500$ Hz and the frequency range is subdivided by bandpass filtering. Instead of directly calculating the dispersion curve, we filtered the modeled data with a bandpass of 0-400 Hz and 400-800 Hz, obtaining two data sets with two different source frequency ranges. As a simplification, we define the source center frequency to be 200 Hz for the 0-400 Hz bandpass filtered section and 600 Hz for the 400-800 Hz bandpass. We find this more suitable to illustrate the main point. Dispersion curves according to this problem have been shown in Chapter 3.8 (red circles) and are discussed in more details in the following chapter. Next we apply a velocity reduction $v_{\mathrm{red}} = v_{\mathrm{s}} = 3100\ \frac{\mathrm{m}}{\mathrm{s}}$ to determine if the TS-waves excited at the two different frequencies ranges travel at different velocities. That means, we shift each seismogram trace by a time delay of $\frac{s}{v_{\mathrm{red}}}$, where s is the distance to the source. The common-source gathers are displayed in Figure 4.5b and 4.5d. A black line indicates if the TS-wave arrivals form a horizontal line, i.e., the wave travels with the applied reduction velocity v_{red}. As shown in the Figure, the TS-wave travels at almost S-wave velocity for the lower frequency range (0-400 Hz, $w > 3.0$). Increasing source frequency to $w \approx 1.0$ decreases the tunnel surface wave velocity by approximately 100 $\frac{\mathrm{m}}{\mathrm{s}}$. In addition to the velocity reduction, hodograms are extracted from the bandpass filtered synthetic seismogram sections at an offset of about 38 m. They are displayed in Figure 4.6b and 4.6d. For surface waves, we would expect an elliptical particle motion with a maximum amplitude normal to the tunnel wall (y-component in case of an excitation at the right or left tunnel wall side). In contrast, the dominant particle motion of the tunnel surface wave at lower source frequencies is linearly rather than elliptically polarized in the plane normal to the tunnel wall (x-y plane, Figure 4.6b), indicating an S-wave. Focusing on the receiver gather, which is bandpass filtered at higher frequencies, we see a clearer elliptical particle path (Figure 4.6c). The amplitude decay with increasing $w = 1.0 \rightarrow 3.1$ is about a factor of 2.1.

Even though we used two different modeling approaches to investigate the TS-wave velocity and the amplitude behavior in relation to the wavelength-to-tunnel-diameter ratio w, there is good agreement. At high w, both the analytic solution and the results of the finite difference modeling indicate that $v_{\mathrm{ts}} \rightarrow v_{\mathrm{s}}$. The hodogram gained from the finite difference modeling shows an almost linearly polarized particle motion typical for S-waves, which can be explained by the low amplitude of the TS-wave predicted by the analytic solution. Instead of TS-waves, S-waves are excited at high w. Decreasing w results in the excitation of typical surface wave ($v_{\mathrm{ts}} < v_{\mathrm{s}}$ and significant amplitude with elliptical polarization). Even the quantitative measures of amplitude and velocity decay with increasing w are almost identical.

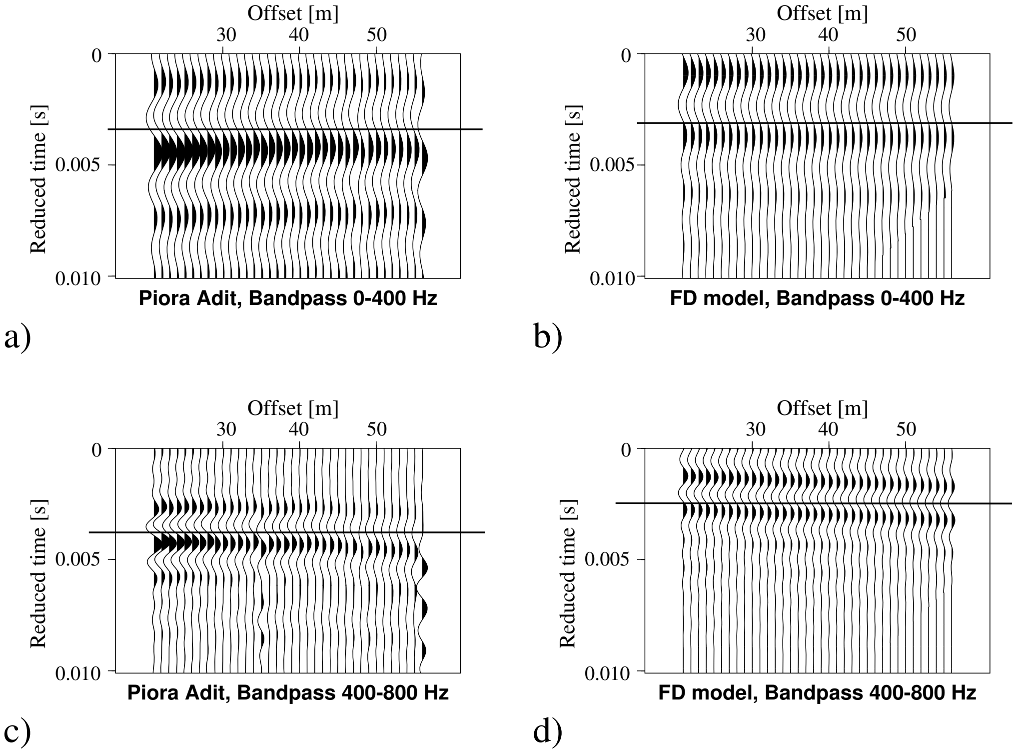

Figure 4.5.: Common-receiver gather of field data (left) and common-source gather of finite difference data (right) within the frequency ranges of 0-400 Hz (top) and 400-800 Hz (bottom). A reduction velocity $v_{\text{red}} = 3100\ \frac{\text{m}}{\text{s}}$ is applied (thick black line). In all seismogram sections, the y-component normal to the tunnel wall is displayed.

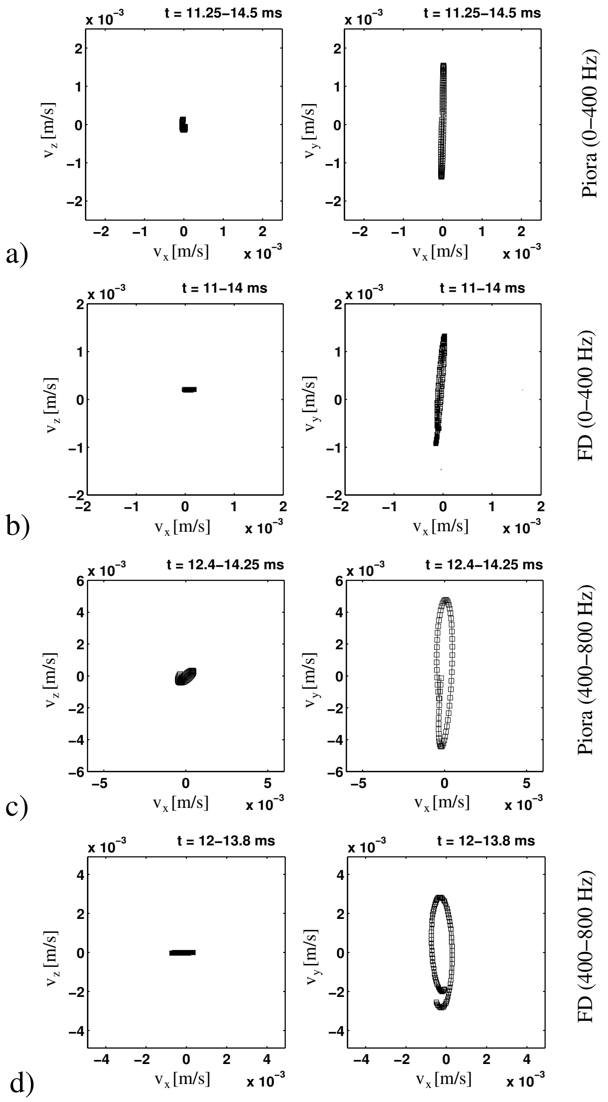

Figure 4.6.: Hodograms of particle velocity in the x-z (left) and x-y plane (right) of field data (extracted at the white dotted line in Figure 4.8) and synthetic data. Frequency ranges are 0-400 Hz (top, a and b) and 400-800 Hz (bottom, c and d). The offset is approximately 40 m.

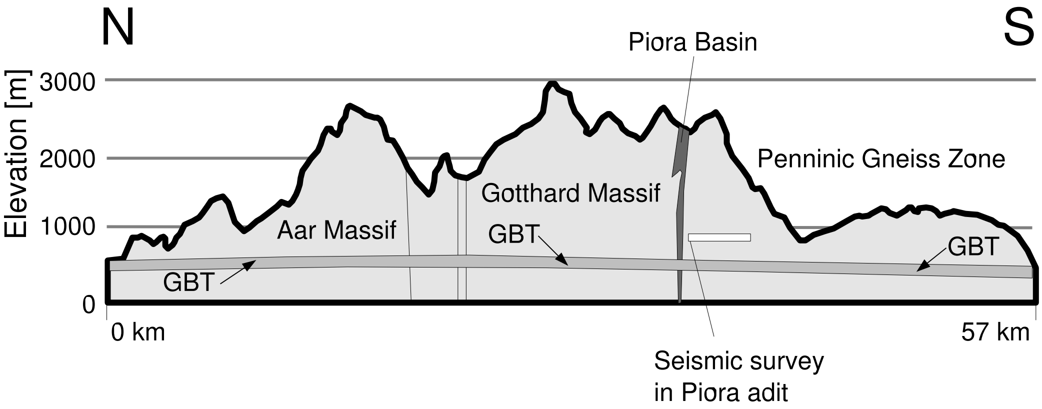

Figure 4.7.: Sketch of the geological cross section along the Gotthard Base Tunnel (GBT). The location of the Piora adit is indicated by a white rectangle south of the Piora Basin (taken from Lüth et al., 2006).

4.2. Field data observations

To test the applicability of the theoretical propagation characteristics of tunnel surface waves (TS-waves) discussed above, we directly compare them with field data. The field data were acquired in the *Piora adit* near the Gotthard Base Tunnel, Switzerland, which was drilled into the Penninic gneiss zone heading toward the Piora Basin and is consisting of stable carbonatic sulfatic sedimentary rocks (Figure 4.7). Within the past few years, the GFZ German Research Center for Geosciences, Potsdam, Germany, has acquired data sets within the Piora adit using several source and receiver geometries (Lüth et al., 2006). During a tomographic survey, the following acquisition geometry was used (Figure 2.1a and Figure 4.8a). 15 three-component receivers were fixed in 2 m deep boreholes on one side of the tunnel (black triangles). On the same side of the tunnel, 147 circles mark the source points where a pneumatic impact hammer with a source center frequency of about 500 Hz was applied. The common-receiver gather (CRG) for receiver 8 (rec8, y-component) is shown in Figure 4.8b. Clearly visible are the strong continuous arrivals (black dotted line), which were identified as tunnel surface waves and *tunnel wall waves*, respectively. P-wave arrivals are very weak, direct S-waves, which would be typical for a point force applied at a plane surface (Bohlen et al., 2003), can not be identified. In the distance range of 0-75 m (left side of the CRG), the formation is dominated by intact host rock. Here, the tunnel surface wave arrivals form a straight line and no clear dispersion effects are visible. In contrast, at distances larger than 75 m, the observed wave field is consistent with dispersive waves possibly caused by a fractured rock as observed by Borm et al. (2003b). To investigate the velocity and particle motion of the tunnel surface wave, we focus on the arrivals within the distance range 20-55 m, equaling an offset range 21-56 m. The receiver position is at 76 m (Figure 4.8b, data section).

A previous publication (Lüth et al., 2006) identifies the strong arrivals as a TS-wave because of its large amplitude and smaller amplitude decay in the far field. However, there are good reasons to doubt this interpretation. First, the Piora adit was drilled with a tunnel boring machine causing an excavation damage zone (EDZ) around the tunnel (Malmgreen et al., 2007;

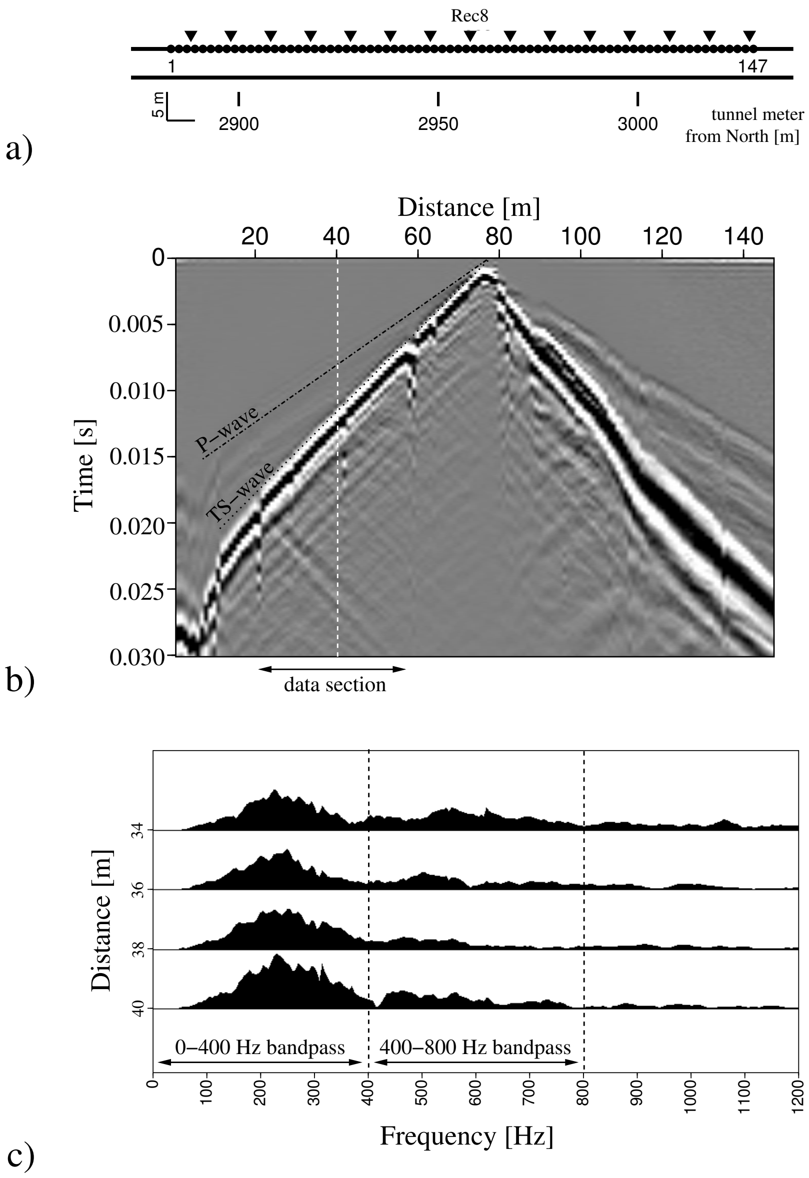

Figure 4.8.: a) Source and receiver geometry of the seismic survey in the Piora adit (top view). Receivers are marked by triangles, source points by circles. b) Common-receiver gather of Rec8 (y component). Assumed arrivals of the P-wave and the tunnel surface wave are indicated by dotted lines. The white dotted line marks the trace where hodograms are extracted to visualize wave polarization. Below the gather, a black double-arrowed line marks the offset range used for the velocity determination. c) Amplitude spectra of seismogram traces at 36 - 40 m distance, two black lines mark the range of the bandpass filters.

Schuster et al., 2001). Recent tunnel wall tomography measurements showed that the EDZ can be considered as a gradient medium where compressional wave velocities increase from the tunnel wall to a depth of a tunnel radius by up to 20 % and more (Giese et al., 2005, also see Chapter 3.4). In the frequency range considered, this causes surface waves to show *medium* *related dispersion* effects (Bohlen et al., 2007), which are not clearly visible in the field data. Second, the picked surface wave velocity is close to the expected formation S-wave velocity of about 3100 $\frac{\text{m}}{\text{s}}$ (Lüth et al., 2006) while no S-wave are traceable.

Since the medium related dispersion in the presence of an EDZ is expected to be much larger than the tunnel related dispersion, we ran several finite difference models with varying EDZ properties, which have been presented in Chapter 3.4. From these synthetic dispersion curves in Figure 3.8b we can draw three conclusions. First, in the absence of an EDZ there is still a decrease in the TS-wave velocity with increasing frequency, which is due to the tunnel related dispersion. The shape of both the dispersion curve determined by finite difference modeling and the analytic solution correspond well. Second, the medium related dispersion is effectively caused by the presence of a gradient in the S-wave velocity model. In case of only a gradient in the P-wave velocity, the dispersion curve follows the dispersion curve gained from the model without any gradient. In contrast, the dispersion curves for a gradient in only the S-wave velocity model and for both a gradient in P- and S-wave velocities are almost identical. Finally, the dispersion curve for a low velocity gradient of only 6% decrease in both the P- and S-wave velocity toward the tunnel surface fits the Piora dispersion curve very well. Therefore, the shape of the Piora dispersion curve and the low dispersion properties of the TS-wave in the field data can be explained in the following way. Either a smaller damage of the formation rock has occurred resulting in a lower P- and S-wave velocity gradient, or the S-wave velocity field around the tunnel is less influenced by the tunnel construction, while there is still a significant gradient in the P-wave velocity. In any way, the Piora field data show little to no medium related dispersion.

Considering the analytic solution and the results of the finite difference modeling for a homogeneous model without an EDZ, we can now try to analyze the influence of tunnel related dispersion in real data in detail. Since a single force hammer source was applied, we primarily compare the finite difference model response with the field data seismogram sections. Even though the source center frequency of the pneumatic hammer is about 500 Hz, there is still enough energy excited at lower and higher frequencies (see Figure 4.8c). Therefore, we can again apply the bandpass filters and the linear reduction velocity in the same way. The velocity reduced common-receiver gathers are displayed in Figure 4.5a and 4.5c. Additionally, along the white dashed line in Figure 4.8 at an offset of about 38 m, hodograms are extracted for both bandpass filtered sections, which are displayed in Figure 4.6a and 4.6c. From Figure 4.5 and Figure 4.6 we can conclude that the Piora field data corresponds very well to the finite difference data, proving the model assumption to be comparable. In both data sets, the tunnel surface wave travels at approximately 3100 $\frac{\text{m}}{\text{s}}$ and the particle motion is mostly linearly polarized at low frequencies. At higher frequencies the surface wave velocity decreases by about 100 $\frac{\text{m}}{\text{s}}$ and an elliptical particle motion is observable, while the maximum particle velocity (v_y) decreases by a factor of about two (finite difference model) to three (Piora data).

To sum up so far, there are several arguments (greatest amplitudes, less amplitude decay) for identifying the strong arrivals as surface waves as well as reasons to doubt this (missing dispersion properties, hodograms). Obviously, it is a matter of source frequency. With a tunnel surface wave velocity picked from the seismogram of roughly $v_{\text{ts}} = 3100\ \frac{\text{m}}{\text{s}}$ and a bandpass filtered hammer source frequency of approximately 200 Hz, the tunnel-wave wavelength is about 15.5 m ($w = 3.1$) and hence large enough to sense the tunnel curvature. This is supported by the tunnel surface wave showing properties of an S-wave. A higher source frequency of 600 Hz results in a smaller tunnel surface wave wavelength of about 5 m ($w = 1.0$). This is selected by the bandpass 400-800 Hz and emphasizes the surface wave character. In particular the hodogram indicates a more elliptical particle motion, which is typical for Rayleigh surface waves. Both the Piora field data and the corresponding modeled receiver sections fit well to the analytic tunnel surface wave propagation characteristics in terms of velocity and particle motion.

4.3. Chapter discussion

Combining both the surface wave propagation calculated by the analytic solution and the observations from the measurements taken by the GFZ German Research Center for Geosciences (Potdam, Germany) at the Piora adit, an almost consistent picture is drawn. First, we focus on the impact hammer source, bandpass filtered in the range of 0-400 Hz. With a surface wave velocity of roughly 3100 $\frac{\mathrm{m}}{\mathrm{s}}$ calculated from the seismograms, the tunnel diameter of 5 m and the source center frequency of approximately 200 Hz, the wavelength-to-tunnel-diameter ratio w is about 3.1. At this large w the analytical solution predicts a surface wave with S-wave properties. Indeed, this can be reproduced by the Piora adit measurements. The absent S-wave arrivals in both the Piora and the simulated data can be explained either by their low amplitude or by the fact that the theoretical surface wave has similar velocity and polarization. Another supporting argument is provided by the calculated hodogram. Figure 4.6a shows elliptical particle motion, which is deformed to an almost linear polarization. This can be explained by a surface wave with mostly S-wave properties. The fact that the tunnel surface wave exhibits no clear medium related dispersion is possibly due to a low S-wave velocity gradient within a distance of one dominant wavelength of about $\frac{3100\ \frac{\mathrm{m}}{\mathrm{s}}}{200\ \mathrm{Hz}} = 15.5$ m behind the tunnel wall.

Increasing the source center frequency to 600 Hz (400-800 Hz bandpass filtered section) and therefore decreasing w to 1.0 leads to an excitation of more Rayleigh wave like surface waves (Figure 4.3 and Figure 4.4). In this case, the hodogram shows a more elliptical particle motion. The decay of amplitude and particle velocity measures in the same range: factor 3.2 (Piora data), factor 2.1 (FD modeling) and factor 1.8 (analytic solution). Also, the propagation velocity along the tunnel is lowered by approximately 100 $\frac{\mathrm{m}}{\mathrm{s}}$. This velocity reduction can be reproduced by modeling and agrees nearly with the 80 $\frac{\mathrm{m}}{\mathrm{s}}$ predicted by the analytic solution. Nevertheless, the wavelength is still large enough to prevent typical Rayleigh wave excitation. To separate S-wave and Rayleigh wave excitation while considering the analytic solution, we propose the wavelength-to-tunnel-diameter ratio $0.6 < w < 1.2$. Below $w < 0.6$, excited waves show significant Rayleigh wave characteristics. In the case of $w > 1.2$, mainly S-waves are propagating along the tunnel. In between, the tunnel surface waves show a mixture of S-wave and Rayleigh wave properties. Due to the limited excitation frequency range of the impact hammer, a further increase in the source center frequency by means of a bandpass with a higher frequency range (e.g., 800-1200 Hz) is not possible. We believe this would show pure Rayleigh wave excitation in the measurement data.

A still unanswered question deals with the analytical solution of the tunnel surface wave at high wavelength-to-tunnel-diameter ratios. Further research has to investigate the nature of S-wave characteristics beyond the tunnel wall. Snapshots of the S-wave field gained by finite difference modeling reveal an exponential amplitude decrease with the increasing distance from the tunnel wall (Bohlen et al., 2007). We therefore suggest the analytic solution of the surface wave to describe the boundary condition for S-wave propagation at free surfaces, which would explain the S-wave velocity and the low amplitude. However, Stielke's derivation of the wave equation in cylindrical coordinates does not cover body waves or any changes of surface wave properties with respect to the depth in the rock (Stielke, 1959). Future work will employ an analytic solution for body waves in cylindrical coordinates for an empty tube within a homogeneous full space.

4.4. Chapter conclusions

Measurements at the Piora adit, corresponding finite difference modeling results and analytical solutions around an empty tube in a full space were used to investigate the propagation characteristics of tunnel surface waves. We confirmed the theoretical prediction that the excitation of tunnel surface waves in a homogeneous medium depends on the ratio of surface wave wavelength-to-tunnel-diameter w. At low values of $w < 0.6$, Rayleigh surface waves can be observed. In contrast, we claim to excite only body S-waves at large wavelength-to-tunnel-diameter ratios of $w > 1.2$, i.e., when the wavelength is large enough to sense the curvature of the tunnel. In between $0.6 < w < 1.2$, a transition between Rayleigh surface wave and S-wave can be observed. Note that this range of w is a proposed range and might be subject to change by ±0.1 or more by future investigation on other field data sets.

Especially for the exploration ahead of the tunnel using the tunnel-surface-to-S-wave conversion at the tunnel front, it is important to consider the influence of source center frequency. As shown by the measurements at the Piora adit, prediction ahead of the tunnel is working with S-wave excitation, too. However, pure Rayleigh wave excitation and conversion into S-waves can improve detection of lithological boundaries because, e.g., Rayleigh waves are easy to excite and have a high signal-to-noise ratio (Forbriger, 2003).

CHAPTER V

Prediction of geological structures using TSST-waves

Tunneling all over the world often utilizes tunnel boring machines (TBMs). This way of tunnel excavation limits disturbances to the surrounding host rock, which is especially important in urban areas. Also, it increases the overall tunnel construction performance and reduces the cost of an additional tunnel lining by providing a smooth tunnel wall (Petronio and Poletto, 2002). TBMs are capable of drilling through almost all kind of rocks and the geological situation along the tunnel profile is usually well known (Lüth et al., 2006). However, geological mapping based on surface measurements and geophysical data lack resolution with the increasing depth. Hence, there can be uncertainties regarding the location or even the existence of geological structures ahead of the tunnel construction. Look-ahead prediction methods can help to decrease these uncertainties by correlating assumed geological features with their actual spatial location. Thereby, expensive TBM downtimes and safety risks can be minimized, too.

We recently introduced a seismic tunnel look-ahead prediction method using tunnel surface waves (Bohlen et al., 2007; Jetschny et al., 2010). Without interference in the tunnel construction, tunnel surface waves (TS-waves) are excited behind the TBM and travel along the tunnel wall in drilling direction. At the tunnel face, these TS-waves are mainly converted into body S-waves, which can be reflected at geological heterogeneities ahead of the tunnel. After back-conversion at the tunnel face as TS-waves, these seismic signals can be recorded by receivers placed behind the TBM along the tunnel wall and provide information on the distance and the spatial location of the reflector. According to its wave path, as a direct TS-wave, converted S-wave, reflected S-wave as well as back-converted TS-wave, we call these signals TSST-waves, even though TS-S-S-TS-wave would be the more precise term. At different tunnel construction sites the look-ahead prediction using TSST-waves has proven its capability of predicting fault zones, lithological interfaces and other geological structures (Bohlen et al., 2007; Lüth et al., 2006, 2008b).

Regardless of the method, current interpretation of tunnel seismic data requires in most cases either an experienced geophysicist present on the TBM, or an upload of the data to an office away from the tunnel construction site. Both ways are either expensive or do not provide imaging results in real time. In addition, the basis for almost all prediction approaches is seismic migration (Ashida, 2001; Borm et al., 2003b; Dickmann, 2005; Kneib et al., 2000), which demands significant computational power and further interpretation. In the following, we focus on the development of a relatively simple but robust prediction technique with respect to the TSST-wave path. Goal of this study is to detect large scale geological structures ahead of the tunnel like fault zones, lithological boundaries, or large erratic blocks. No a priori information beside the measurement geometry shall be used. As a first step toward a reliable automatic interpretation of tunnel seismic data, we do not attempt to classify or differentiate the kind of reflector. Instead, we provide a stable and reliable distance estimate of the structure from the tunnel face. This can be the basis for further correlation with other information or the refinement toward a real 3-D imaging of the reflector.

5.1. Modeling of a tunnel seismic survey

The availability, usability and access to field data in order to study prediction methods is often problematic, especially when it comes to tunnel seismic data. First, the number of tunnel construction sites accessible to seismic measurements is limited due to restrictions by the building owners. Second, there are usually few chances of controlling the geological formation surrounding the tunnel or the tunnel construction progress itself. If there are no geological structures intersecting the tunnel trajectory - even if they are expected - or if prolonged downtime of the TBM occur, a field survey cannot provide useful data. Also, field surveys in tunnel environments require special equipment, are expensive and complex, especially when they cover long periods of drilling time. Therefore, it is natural to first employ wave simulations in order to study the prediction methods and processing steps.

Such a synthetic model has to ensure that both the simulation results are feasible and realistic and consider the computational modeling limitations. The basis for our model is a 3-D self-similar, random media volume (Hutchinson, 1979), which includes random variations in elastic properties (density, P- and S-wave velocity) and structures at different length scales (Figure 5.1a, b). In this way, we simulate a heterogeneous and irregular structured rock formation with elastic property variations of up to 5 %. These seismic formation properties base on a typical hard rock with values listed in Table 2.1. An essential part of the model is a low velocity wedge, which has to be passed by the simulated tunnel construction (Figure 5.1a, white dashed line). Hence, we have two impedance contrasts representing two plane lithological boundaries and faults, respectively. The dimensions of the wedge enables the tunnel construction and the measurement geometry, respectively, to near the first fault and pass it completely before approaching the second fault. This way, the independent detection of two sequenced lithological boundaries with different inclination angles φ can be tested (see Figure 5.2).

In our model, the excavated material is replaced with vacuum. Also, the tunnel is surrounded by a simulated excavation damage zone (EDZ). In agreement with common assumptions on the dimension of the EDZ (Schuster et al., 2001; Borm et al., 2003b), the modeled EDZ extends twice the tunnel radius into the surrounding formation and is approximated by a seismic velocity and density gradient. We applied a linear decrease of up to 20% of the original random media formation velocities and density toward the tunnel surface (see Chapter 3.4). This causes the TS-wave to exhibit *medium related dispersion*. A point force source is applied to one side of the tunnel wall and various 3-component receiver lines record the wave field along and ahead of the tunnel. In order to simulate the tunnel construction progress, both the tunnel working front and the source position is shifted by 2 m for each shot toward the wedge. The first simulation starts with a tunnel face-to-fault1 distance of 40 m. In the course of the

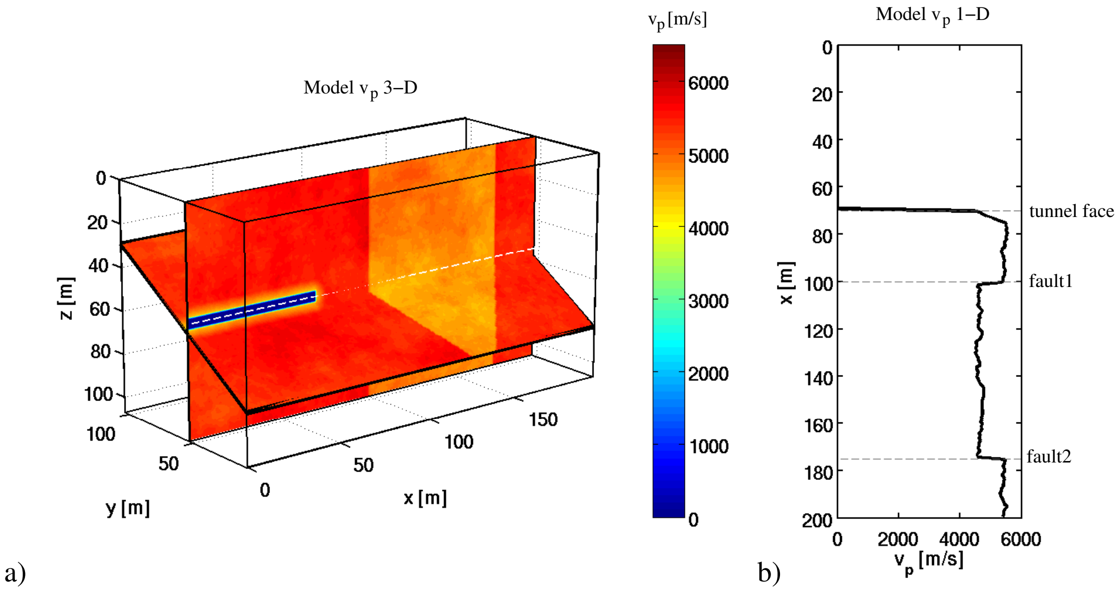

Figure 5.1.: Compressional wave velocity model used for the finite difference modeling of a tunnel look-ahead prediction survey. a) Slices of the v_p velocity model within the 3-D random medium volume. The evacuated tunnel (blue v_p values) is surrounded by an excavation damage zone (EDZ) and is approaching a wedge characterized by lower seismic velocities (yellow to orange values). The wedge's sides can be treated as two fault zones, which are tilted with respect to the tunnel axis. b) 1-D v_p velocity profile along the tunnel axis marked by a white dashed line in the 3-D volume.

simulated tunnel construction, the tunnel penetrates the first lithological boundary (fault1) and approaches the second fault. For each shot, we later extract a single receiver with a constant offset of 2 m and obtain a synthetic dataset of shot-receiver pairs moving with the tunnel face (Figure 5.2). The source-to-tunnel-face distance (40 m) and source-to-receiver distance (2 m) is therefore constant. Each wave field simulation is computed by a parallel 3-D finite difference (FD) modeling code (Bohlen, 2002) and takes more than 10 h on a 64 CPU cluster computer.

A synthetic seismogram section corresponding to the model in Figure 5.1 (source position at 30 m, tunnel face at 70 m) is displayed in Figure 5.3 and illustrates the dominant wave types. The excited tunnel surface wave (TS-wave) propagates along the tunnel until it arrives at the tunnel working front. There, the TS-wave is being both reflected and generates mainly body S-waves (TS-S-wave) propagating ahead of the tunnel. At both plane lithological boundaries (fault1 and fault2) these waves are reflected and travel back to the tunnel (TS-S-S1 and TS-S-S2). Once they approach the tunnel face, they are back-converted into tunnel surface waves and propagate along the tunnel (TSST1). Note that due to the inclination φ of the faults with respect to the tunnel axis (Figure 5.2), the apparent velocity of the reflected S-wave (TS-S-S1), which arrives at the receiver line parallel to the tunnel axis, is larger than the formation S-wave velocity. Another prominent feature in the seismogram is the dispersion of the reflected TS-wave due to the large dimension and velocity gradient of the EDZ. Isolating the TSST arrivals from the slow phases of the reflected TS-wave is difficult when the tunnel face is closer

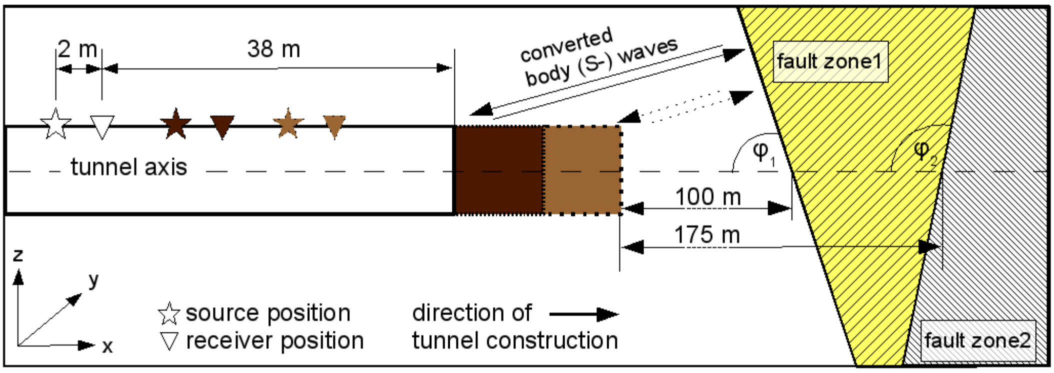

Figure 5.2.: Top view of the measurement geometry used for the finite difference modeling of a TSST look-ahead prediction survey. Sources and receivers are marked by stars and triangles, respectively. While the simulated tunnel construction is approaching the fault zone, the measurement geometry is moving, too. Therefore, the source-to-receiver distance and the source-to-tunnel-face distance is kept constant.

to the lithological boundary. Also, the simulated formation heterogeneities cause reflections superimposing late and weak TSST-wave arrivals.

The number of receivers during a tunnel seismic survey is very limited, hence we pick the worst case scenario of only one receiver per shot. After combining all the receivers with a constant offset of 2 m for all the 56 shots, we obtain the tunnel seismic data in Figure 5.4a. The direct TS-wave arrivals now line up on a straight line, as do the reflected TS-waves, before the tunnel penetrates the first fault. When advancing into the low-velocity zone, the overall formation velocity along the tunnel wall decreases and the time difference between the direct and reflected TS-wave increases. Beside the reflection signals from formation inhomogeneities, the TSST1 arrivals corresponding to the first lithological boundary are clearly visible. After penetrating the first fault zone, these reflection arrivals are recorded prior to the TS-wave reflected at the tunnel face. The processing of the tunnel seismic data does not have to focus on isolating these early TSST-wave arrivals, since in this case, the tunnel construction has already encountered the geological structure. In contrast to the TSST1 arrivals, the reflection signals from fault2 (TSST2 arrivals) are less clearly visible, especially for large distances to the second fault.

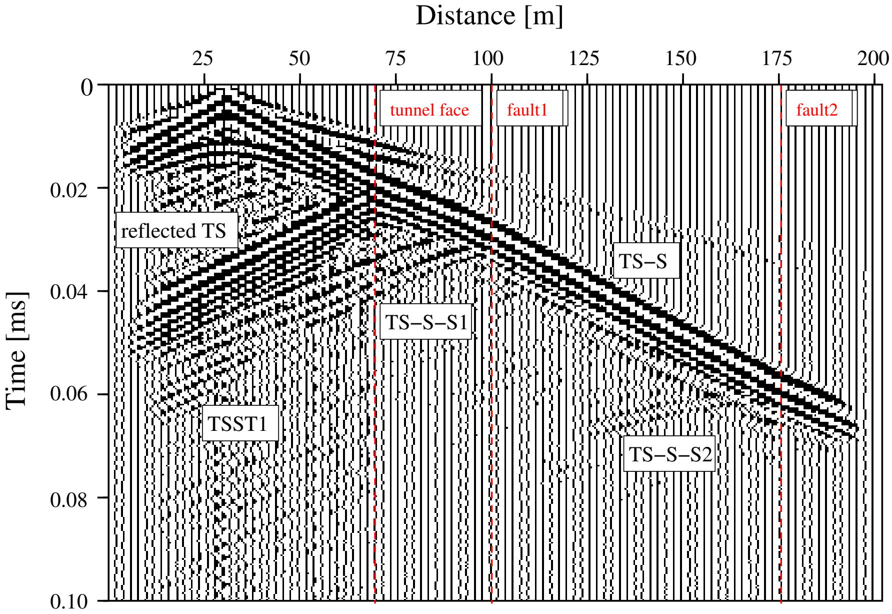

Figure 5.3.: Synthetic common-source gather (y-component) according to the model displayed in Figure 5.1. Shot position is at a distance of 30 m with a tunnel face position of 70 m. The relevant structures within the model and the corresponding wave types are labeled. Only the receiver position at a distance of 32 m is used for the further processing of tunnel seismic data.

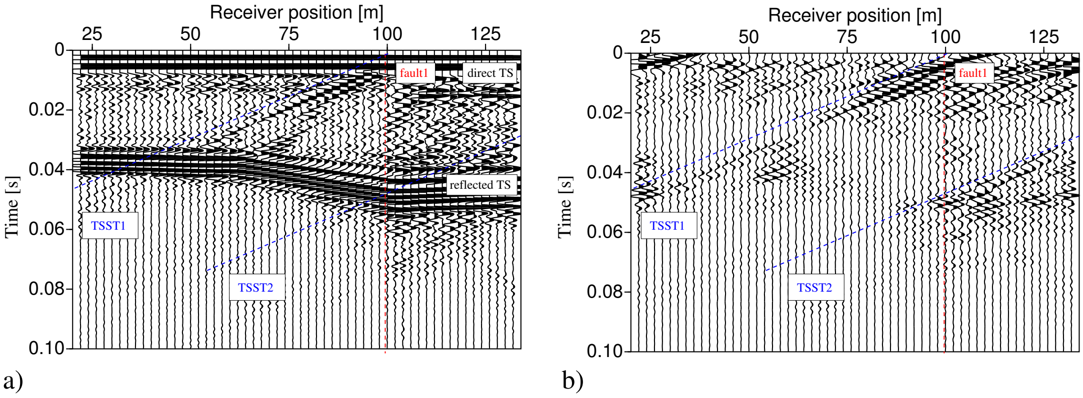

Figure 5.4.: Synthetic tunnel seismic data. For each shot position in the range of 20 m : 2 m : 130 m, the receiver position with an offset of 2 m has been selected: a) unprocessed data, relevant structures within the model and corresponding wave types are labeled; b) dip-filtered data, the TSST-waves are emphasized.

5.2. Prediction processing steps

With a low constant offset of only 2 m, Figure 5.4a can be treated as a zero offset section ready for seismic migration. Unfortunately, none of the common migration algorithms take the TSST-wave path into account. Both the TS-to-S-wave conversion and the TS-wave propagation time along the tunnel and its velocity v_{ts} different from the formation S-wave velocity v_{s} is neglected. From Chapter 4 it follows the velocity ratio $\frac{v_{\mathrm{ts}}}{v_{\mathrm{s}}}$ can range from 0.9 to 1.0 depending on the wavelength-to-tunnel-diameter ratio w. Also, there are only a few seismic receivers mounted on opposite sides of tunnel wall causing imaging ambiguities. Therefore, standard migration methods fail to correctly image structures ahead of the tunnel using TS-waves. In addition, migration algorithms can require considerable computational power and a migrated section has to be further interpreted in order to produce a simple result. As described in the introduction to Chapter 5, we aim to obtain robust information on the tunnel face to fault distance $s_{\mathrm{tf-f}}$ with as little a priori information as possible. For this reason, we introduce an prediction concept that combines common processing steps in order to solve the simple TSST-wave travel time relation in equation 5.1.

$$\begin{aligned} t_{\mathrm{tsst}} &= t_{\mathrm{s-tf}} + 2\,t_{\mathrm{tf-f}} + t_{\mathrm{tf-r}} \\ &= \frac{s_{\mathrm{s-tf}}}{v_{\mathrm{ts}}} + 2\,\frac{s_{\mathrm{tf-f}}}{v_{\mathrm{s}}} + \frac{s_{\mathrm{tf-r}}}{v_{\mathrm{ts}}} \end{aligned} \tag{5.1}$$

where

t_{tsst} = total travel time of the TSST-wave,
$t_{\mathrm{s-tf}}$ = travel time of the TSST-wave from the source to the tunnel face,
$t_{\mathrm{tf-f}}$ = travel time of the TSST-wave from the tunnel face to the fault,
$t_{\mathrm{tf-s}}$ = travel time of the TSST-wave from the tunnel face to the receiver,
$s_{\mathrm{s-tf}}$ = source-to-tunnel face distance,
$s_{\mathrm{tf-f}}$ = tunnel-face-to-fault distance,
$s_{\mathrm{tf-s}}$ = tunnel-face-to-receiver distance,
v_{s} = formation S-wave velocity,
v_{ts} = tunnel surface wave velocity.

The travel time t_{tsst} can be picked from Figure 5.4a and both $s_{\mathrm{s-tf}}$ and $s_{\mathrm{tf-r}}$ are known, which leaves only v_{ts} and v_{s} to determine $s_{\mathrm{tf-f}}$. The TS-wave velocity can be obtained either by the first arrival time of the TS-wave at the receiver with the known offset or by the time difference between the direct and reflected TS-wave with a known travel distance ($s_{\mathrm{s-tf}}+s_{\mathrm{tf-r}}$). The latter method is preferred because the source-to-receiver offset is small and picking the first break can be problematic in the presence of noise. For geometrical reasons, the formation S-wave velocity v_{s} is twice the apparent TSST-wave velocity v_{a} in Figure 5.4a. In the following, we present a step-by-step procedure of how to obtain the travel time and velocity of the TSST-wave as well as the S-wave velocity from the tunnel seismic data. The according flowchart is displayed in Figure 5.5.

First of all, we introduce a sliding window of a constant number of traces. Thereby, we simulate the prediction process advancing with the tunnel construction progress. After initial

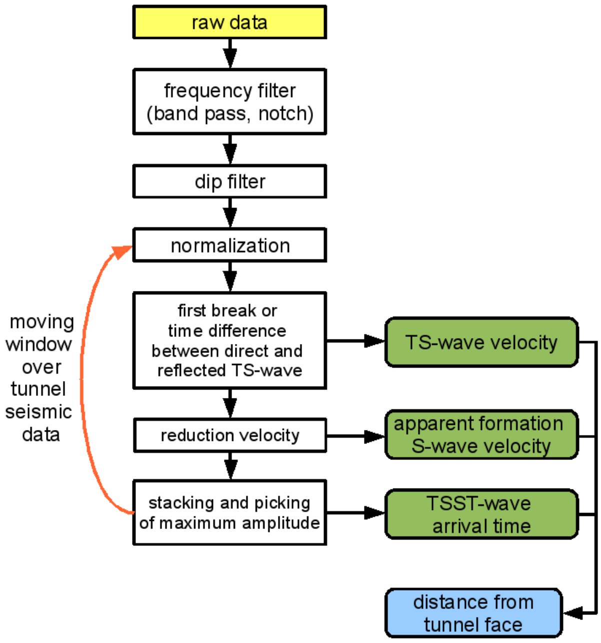

Figure 5.5.: Flowchart of processing steps to detect geological structures ahead of the tunnel face using the TSST look-ahead approach.

data collection, every new shot data is processed together with a number of previous shots to improve the signal-to-noise ratio. We found a window of 10 traces to be optimal, which accounts for a tunneling progress of 20 m.

Now we focus on the TS-wave velocity determination. As is visible from Figure 5.6a, direct and reflected TS-waves are dominant. Also, the signal shape of the reflected TS-wave has changed due to the EDZ related dispersion. However, picking the time difference between the peak amplitude of both the direct and the reflected TS-wave with a known travel distance $(s_{\mathrm{s-tf}} + s_{\mathrm{tf-r}})$ provides a stable TS-wave velocity. Reduction of dispersion effects by cross correlation, picking the time difference in all traces in the window and averaging further improves the accuracy.

In order to provide a reliable determination of both the TSST-wave arrival time and velocity, we have to suppress the direct and reflected TS-wave. We found that the dip-filtering (also called slope, fan or pie-slice filtering) is most suitable for this purpose. A dip-filter is a two dimensional filter designed to weight information depending on its apparent velocity and dip, respectively, instead of the frequency content. After transformation into the f-k domain the filter passes a narrow wedge (pie-slice) corresponding to a range of apparent velocities $0 < v_{\mathrm{a}} < v_{\max}$ according to equation 5.2 (modified from Sheriff and Geldart, 1983).

$$F(f, k_{\mathrm{a}}) = \begin{cases} 0, & |k_{\mathrm{a}}| < \frac{\omega}{k_{\mathrm{a}}} = \frac{2\,\pi\,f}{v_{\max}} \\ 1, & |k_{\mathrm{a}}| > \frac{\omega}{k_{\mathrm{a}}} = \frac{2\,\pi\,f}{v_{\max}} \end{cases} \tag{5.2}$$

where f denotes the frequency, k_{a} the apparent wavenumber, ω the angular frequency and $v_{\max}$ the maximum apparent wave velocity. Since the direct and reflected TS-wave arrivals form a more or less straight line ($v_\mathrm{a} \rightarrow \infty$), we can reject velocities larger than $v_\mathrm{max} = 4000\ \frac{\mathrm{m}}{\mathrm{s}} > v_\mathrm{s}$. In this way, we can significantly emphasize the TSST-wave arrivals, especially in regions close to the dispersive reflected TS-wave (compare Figure 5.4a and b).

Prior to stacking of the traces to increase the signal-to-noise ratio, we have to correct for the apparent TSST-wave velocity v_a, which is unknown. We assume that the reflected signals from either one of the faults or from the formation heterogeneities ahead of the tunnel are the only signals that can constructively stack in the considered seismogram window (Figure 5.6c). Therefore, we apply reduction velocities in the range of $0 < v_\mathrm{red} < v_\mathrm{max}$ to the windowed data. That means, we shift each seismogram trace by a time delay proportional to the distance of the first trace (compare Figure 5.6c and d). If a correct v_red is applied, the reflected signals stack constructively and the sum of the absolute amplitudes is a maximum. In any other case, the amplitude destructively stack and the sum of the absolute amplitudes is smaller. By looping over the reduction velocity, we both obtain the formation S-wave velocity and prepare the window traces to achieve optimal stacking (Figure 5.6e). Note that when the simulated tunneling is advancing by, e.g., 2 m toward the reflector, the two-way travel distance is shortened by twice this distance. Therefore, the effective wave travel distance between two traces in Figure 5.4 is twice the difference in the receiver positions and the formation S-wave velocity v_s is twice the optimal reduction velocity $v_\mathrm{red} = v_\mathrm{a}$. Since v_ts and v_s are now known, we can convert the travel times of the stacked traces into distances and, finally, pick the absolute peak amplitude (Figure 5.6e, gray dot). This peak represents the distance to the strongest reflection ahead of the tunnel.

By repeating these processing steps for every window sliding over the tunnel seismic data, we can calculate distances between a reflector and the advancing tunnel face (Figure 5.6f). By plotting the sum of the absolute tunnel face position and the tunnel face-to-reflector distance we gain a stable reference point independent of the actual tunnel meter progress. Starting from a distance of 40 m until the tunnel face penetrates the first fault zone, the calculated distances (the tunnel face positions plus the tunnel face-to-reflector distances) are stable and within a range ±1 m at 100 m. This agrees precisely with the known position of the first lithological boundary. After penetrating the fault zone, the tunnel surface waves propagate both in the original formation and in the low velocity zone. Because the described processing cannot take a varying TS-wave velocity along the tunnel wall into account (within the same window), the calculated distance values are incorrect. While the tunnel construction advances in the low velocity zone, the detection locks into the second fault and with decreasing distance to fault2, the prediction converges to the known position of fault2 at 175 m. Altogether, both fault structures have been detected reliably, though the first fault more precisely, than the second one. In the following, we study whether the developed processing can be directly applied to field data as well.

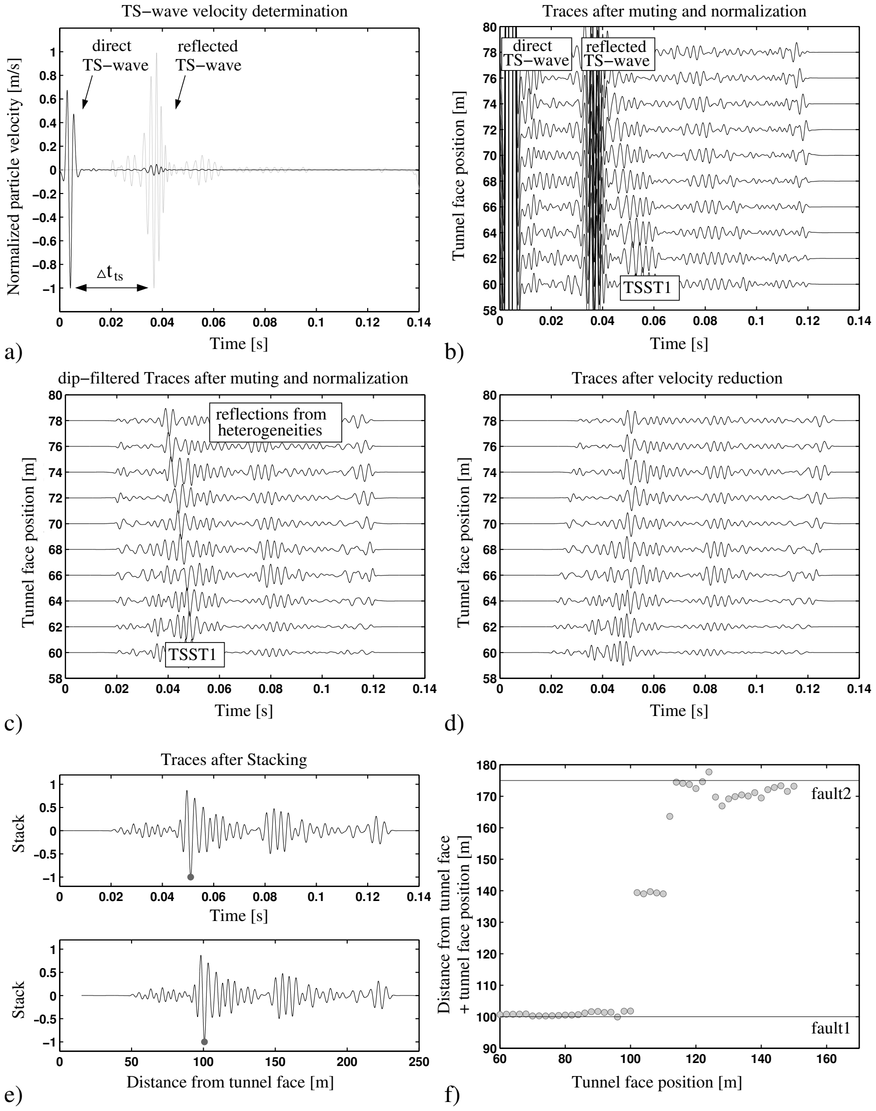

Figure 5.6.: Processing steps to detect geological structures ahead of the tunnel face using the simulated data. a) TS-wave velocity determination: first trace of the tunnel seismic data from Figure 5.4a (black line), first trace of tunnel seismic data after muting of direct TS-wave (gray line); b) window of 10 traces of non-processed synthetic tunnel seismic data illustrating the dominant direct TS-wave and the TS-wave reflected at the tunnel face; c) window of 10 traces of dip-filtered synthetic tunnel seismic data. The TSST-wave is emphasized; d) window of 10 traces of dip-filtered tunnel data after automatic formation S-wave velocity determination and correction; e) window of 10 traces of dip-filtered tunnel data after stacking, the absolute maximum amplitude is marked; f) processing results of a moving window of 10 traces over the synthetic tunnel seismic data, the position of the absolute peak amplitude of each stacked section is plotted.

5.3. Field data observations

In order to test the applicability of the developed processing sequence, we directly apply it to tunnel seismic field data. The first field data were acquired in the *Piora adit* near the Gotthard Base Tunnel, Switzerland, after the tunnel was drilled. A second data set was recorded at the *Neuer Schlüchterner Tunnel* construction site close to Fulda, Germany, accompanying the tunnel drilling.

The Piora adit was drilled into the Penninic gneiss zone heading toward the Piora Basin and consisting of stable carbonatic sulfatic sedimentary rocks (Lüth et al., 2006). After completion of the tunnel, a receiver was anchored into the tunnel wall and a pneumatic hammer source was applied at various offsets along the same tunnel wall side (Figure 5.7a). The common-receiver gather is displayed in Figure 5.7b. The direct TS-wave is the dominant wave and, apparently, formation heterogeneities south of the receiver cause reflections, which are visible parallel to the direct TS-wave as well. In comparison, the reflected TS-wave is weak, however, stronger than the TSST arrivals marked by a black dashed line. Again, a dip-filter is applied to the field data (Figure 5.7c). While significantly suppressing the disturbing reflections originated south of the receiver, the direct TS-wave could not be removed completely. Therefore, it has been muted separately. Considering that both the tunnel working front and the receiver are at a constant position, minor modifications had to be made to the processing sequence in order to handle the different measurement geometry. Since the reflected TS-wave is weak and the separation of the direct and reflect TS-wave is difficult, we now automatically pick the first TS-wave arrivals before muting in order to obtain the TS-wave velocity. Also, the apparent TSST-wave velocity from the common-receiver gather equals directly the formation S-wave velocity ($v_{\mathrm{a}} = v_{\mathrm{s}}$).

The results of the automated prediction are displayed in Figure 5.8a. In addition to the calculated distances from the tunnel face, we also plotted the determined formation S-wave velocity. The distance between the tunnel face and the Piora Basin is stable at about 50 m for each window and corresponds very well with both the rock quality index (RQD, Figure 5.8b) and prediction results from a previous publication (Bohlen et al., 2007). Also, the formation S-wave velocities of $v_{\mathrm{s}} \approx 3100 \ \frac{\mathrm{m}}{\mathrm{s}}$ obtained from each processing loop agree with results from previous surveys (Lüth et al., 2006; Borm et al., 2003b).

We now focus on a real tunnel look-ahead prediction survey at the Neuer Schlüchterner Tunnel construction site. The future railroad path has been partially tunneled through soft rock in closed mode, i.e., concrete tubing segmens stabilize the tunnel wall (see Chapter 1.3). The simplified geological cross section is displayed in Figure 5.9. The survey was performed in a tertiary mould with the tunnel construction approaching a major lithological boundary. While the TBM was advancing into the host rock, a pneumatic source mounted on the TBM was applied at the tunnel wall. The seismic signals were recorded by receivers screwed into the tubing segments, only one receiver per shot has been considered.

With this tunnel seismic measurement layout, we can eventually validate the modeling results from Chapter 3.5 (excitation and recording of TS-waves on top of the lining elements). Synthetic dispersion curves showed that the EDZ in combination with the lining (tubing and mortar backfilling) effectively damps the high frequency content of a point force source. Only long TS-wave wavelength and low source frequencies, respectively, propagate along the tunnel wall with significant energy. We now separate the frequency band of a few selected traces

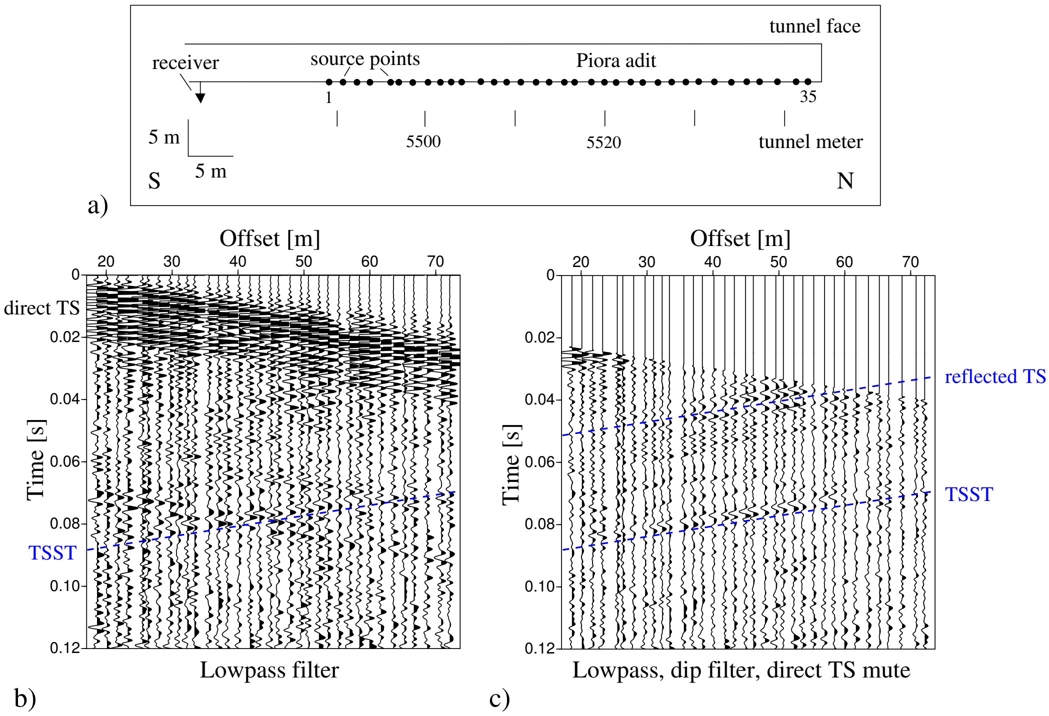

Figure 5.7.: a) Source and receiver geometry of a seismic survey in the Piora adit (top view): The receiver is marked by a triangle, the source points marked by circles are advancing toward the tunnel face. b) Common-receiver gather (y-component) after applying a band pass filter (20-500 Hz), the amplitudes are gained linearly with time. Major wave types are labeled. c) Common-receiver gather (y-component) after applying a band pass filter (20-500 Hz), dip-filter and muting of the direct TS-wave, the amplitudes are gained linearly with time.

from the Schlüchtern survey by means of applying a lowpass and highpass frequency filter. From the shape of a the frequency spectra displayed in Figure 5.10a, we have chosen a limit of 150 Hz and filtered the recorded seismogram sections accordingly. From the comparison of Figure 5.10b and Figure 5.10c we see that most of the TS-wave energy is focused in the lowpass seismogram section even though the pneumatic hammer source can excite waves up to 2000 Hz (see Chapter 2.3). Above 150 Hz mostly high frequency noise possibly originated from the TBM equipment remains in the highpass seismogram section in Figure 5.10c. Hereby, we can confirm the modeling results that the EDZ and the lining in soft rock formation significantly narrows the excited frequency band to frequencies below the actual source center frequency.

In contrast to the measurement at the Piora adit, the Schlüchtern survey geometry is almost identical to that used for the synthetic data described in the previous chapter (Figure 5.2). Beside the TS-wave velocity determination, no changes had to be made to the processing sequence. From the tunnel seismic data in Figure 5.11a (section I) we can identify the direct and reflected TS-wave as well as the TSST-wave (Lüth et al., 2008b). However, picking the TS-wave velocity from the travel time difference of direct to reflected TS-wave does not produce reliable results. Instead, we again pick the first break of the direct TS-wave. Obviously, the coupling conditions of sources and receivers on top of the concrete rings vary along the track,

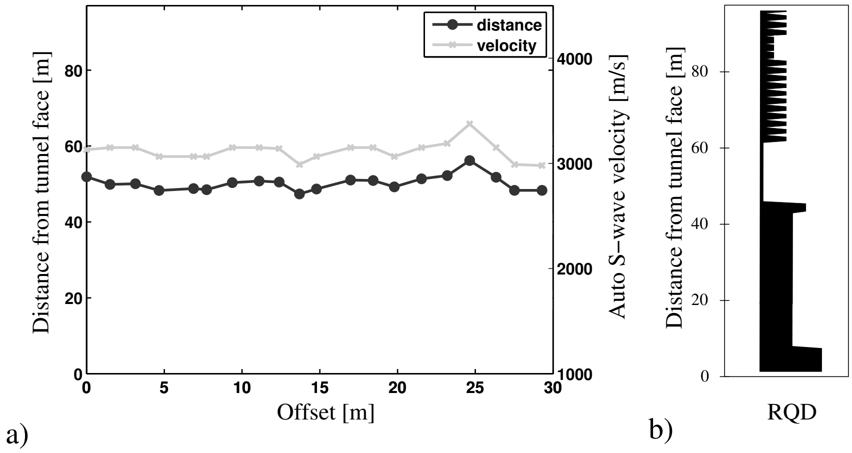

Figure 5.8.: a) Prediction results from the Piora adit field data (Figure 5.7). The automatically determined distance to the Piora Basin from the tunnel face and the corresponding formation S-wave velocity are plotted. b) Rock quality index (RQD) profile ahead of the Piora adit (in direction of drilling), acquired from core samples (modified from Bohlen et al., 2007).

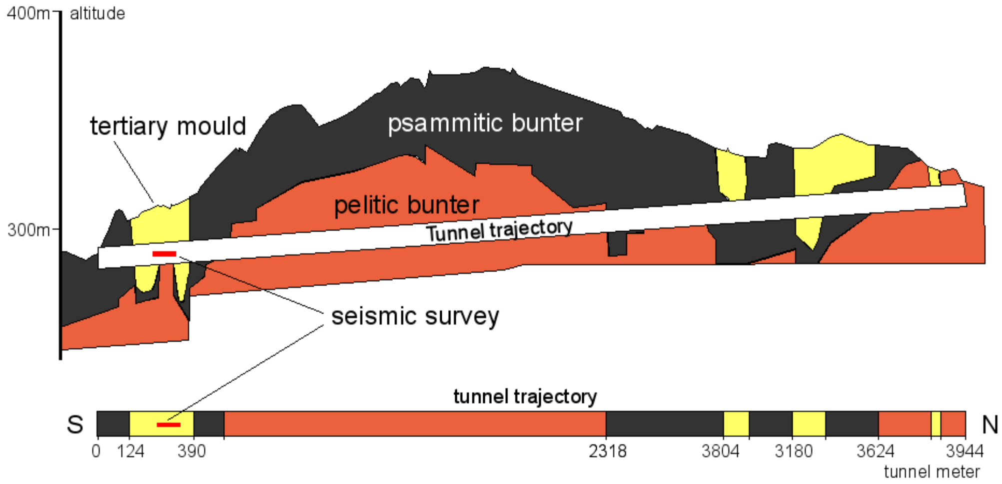

Figure 5.9.: Simplified geological cross section and tunnel trajectory of the Neuer Schlüchterner Tunnel construction site (modified from Lüth et al., 2008a).

possibly due to different filling conditions behind the lining. In the tunnel face position range 315 m - 350 m (section II), all seismic signals are very weak. Beyond 350 m the TSST-wave arrivals are not clearly traceable (section III). Tracewise normalization did not reveal additional information.

After applying the loop of processing steps, we again obtain distances to a reflector from the tunnel face (Figure 5.11b). Up to a tunnel face position of about 300 m, the determined

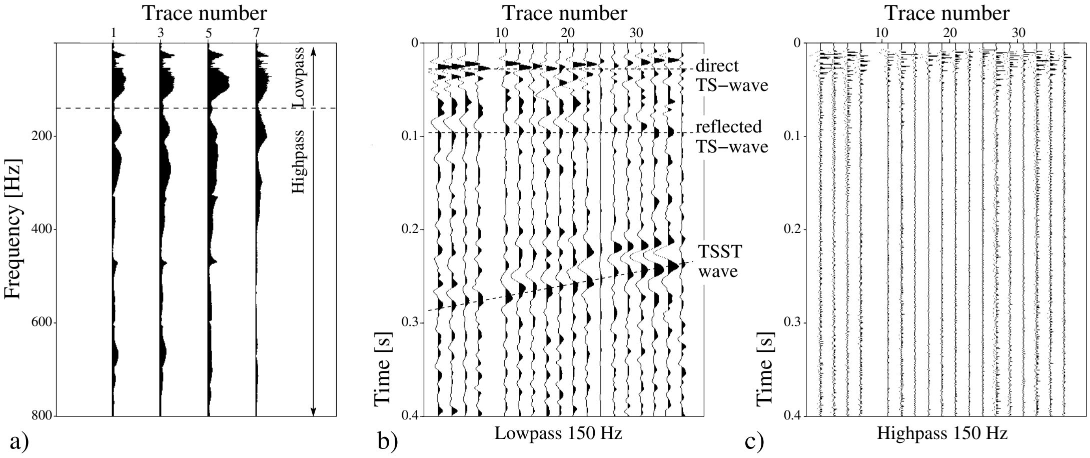

Figure 5.10.: Field data acquired at the Neuer Schlüchterner Tunnel construction site: a) Frequency spectrum of the first data traces (y-component), the limit for the lowpass and highpass frequency filtering is plotted as a dashed line. b) 150 Hz lowpass filtered tunnel seismic data (y-component). The direct and reflected TS-wave as well as the TSST-wave are labeled. c) 150 Hz highpass filtered tunnel seismic data (y-component). No clear arrivals are visible, apparently the TS-wave content has been filtered.

distances (the tunnel face positions plus the tunnel face-to-reflector distances) are stable at about 390 m (section I), which agree well with the lithological boundary between the tertiary and the psammitic bunter (see Figure 5.9). Beyond 300 m (section II), the distances jump to more than 600 m, which do not correlate with any mapped geological structure ahead of the tunnel. From the plot of the TSST-wave arrival time and the S-wave formation velocity in Figure 5.11c, we find that the TSST arrivals still line up linearly beyond the tunnel face position at 300 m. The arrival time values are thus not obviously unreasonable. However, the determined S-wave velocity is approaching the upper limit $v_{\max}$ of the velocity reduction processing step (see Figure 5.6d). This indicates that the stack of the absolute amplitudes does not have a maximum in the reduction velocity range $0 < v_{\text{red}} < v_{\max}$. Therefore, the calculated distances are to be rejected. Beyond a tunnel face position of 350 m (section III), the S-wave velocity drops to reasonable velocities but does not reach a stable value. Only at a tunnel face position of about 360 m a few velocities are again stable below 2000 $\frac{m}{s}$. Nevertheless, the determined arrival times are obviously picked below the assumed TSST line in Figure 5.11a. Hence, the calculated distances are stable but larger than 390 m and do not match a mapped lithological boundary. After all, the processing loop produces reasonable and precise distances if the TSST-wave is traceable in the tunnel seismic data. Otherwise, either the automatically picked travel time or the S-wave velocity is incorrect resulting in unstable and false reflector distances.

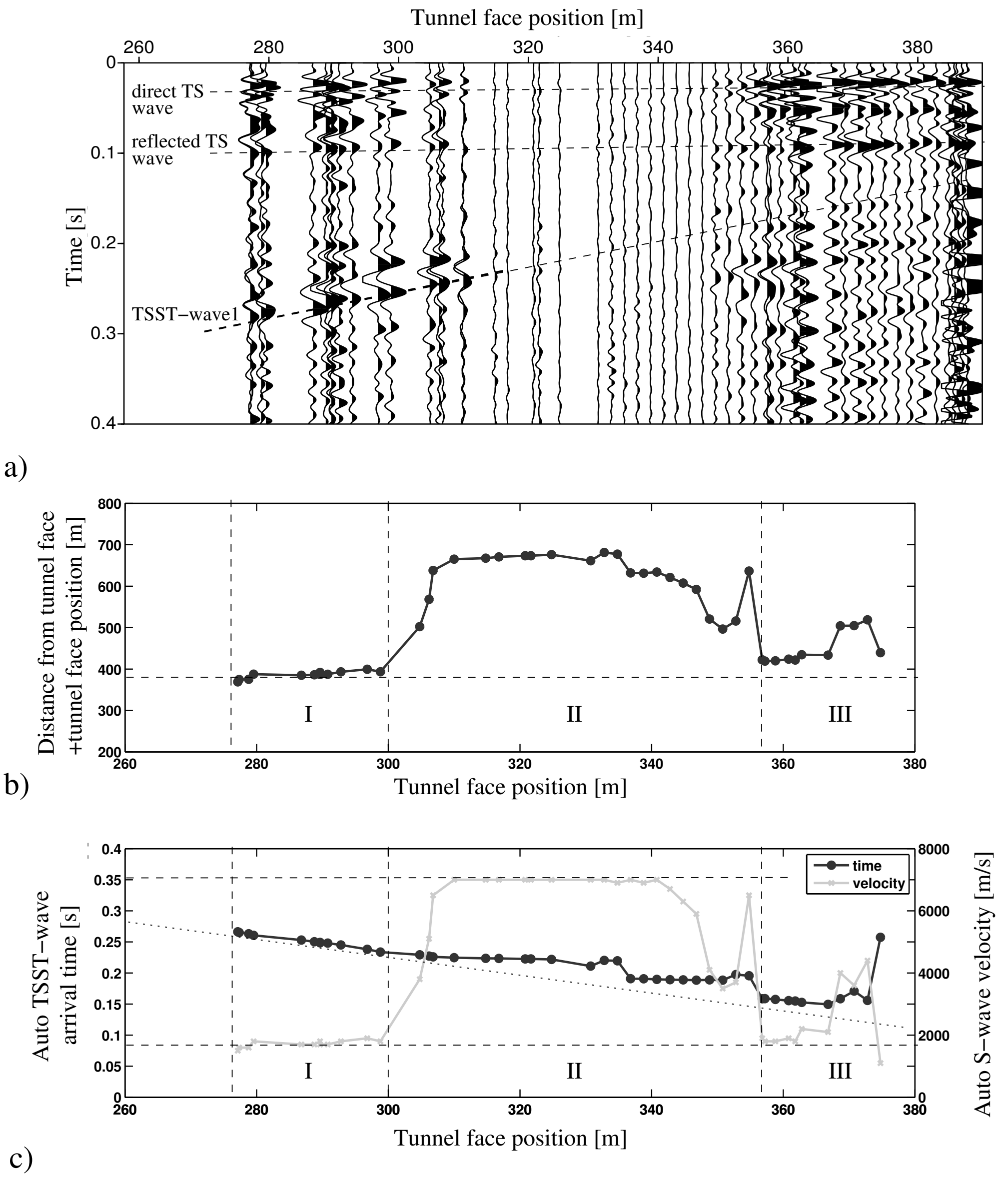

Figure 5.11.: a) 0 - 150 Hz low pass filtered field data acquired during the construction of the Neuer Schlüchterner Tunnel; b) Automatically determined distance of a lithological boundary from the tunnel face; c) Automatically picked TSST-wave arrival time and formation S-wave velocity of each processing loop.

5.4. Chapter discussion

By finite difference modeling we have created a large and valuable synthetic tunnel seismic data set. Only a fraction of its testing potential has been used in this study. With its known structure and flexible survey geometry, the data can be the starting point for future research on imaging methods and general seismic studies during the tunnel construction. On the basis of this synthetic tunnel seismic data set, we have developed processing steps capable of predicting geological structures like fault zones or lithological boundaries (Figure 5.5). The sequence focuses on the isolation and characterization of TSST-wave arrivals in terms of the apparent velocity and travel time. Together with the TS-wave velocity a distance to the reflector from the tunnel face is calculated. All the processing steps can operate with parameters in a default range. This does not allow fine tuning but enables stable detection, presumably, in most environments. Output for each processing loop is a distance corresponding to the most dominant reflection signal, which is usually the TSST-wave (Bohlen et al., 2007). The location of a reflector is validated by constant distances (the tunnel face positions plus the tunnel face-to-reflector distances), i.e., the distances line up as is visible in Figure 5.8a. When no reflected signal is present in the data, no reasonable reduction velocity can be determined and the calculated distances either do not line up or have to be canceled out.

As the developed processing sequence extracts the dominant reflected signal, the reflecting structure does not necessarily have to be large in dimension, or show a strong impedance contrast. The algorithm is capable of detecting reflections originated by both smaller objects, if they significantly reflect the converted S-waves, and lithological boundaries characterized by low impedance contrast in very homogeneous host rocks. Future research on other field data sets can enable differentiation of reflector types by researching different reflection signatures or correlation with additional non-seismic data. With the automatic compensation for different formation S-wave velocities, the influence of dipping structures with respect to the tunnel axis is neglected. Due to geometrical reasons, when a plane wave is striking the tunnel wall at an angle, the apparent velocity of the recorded TSST-wave arrivals is first larger and then converges to the formation S-wave velocity with decreasing distance to the reflector. Previous studies (Bohlen et al., 2007; De Nil et al., 2009) have already shown this potential method for deriving additional information on the spatial location of a reflector.

The prediction sequence has been successfully applied to both simulated data and to two different field data sets. If the TSST-wave is traceable in the data, the distance to a reflector from the tunnel face can be stably and automatically calculated without a priori information. From the simulated tunnel survey and the Piora field data (Figure 5.6f, first fault and 5.8a), we see that a lithological interface can be accurately detected if the TSST-waves travel in reasonably homogeneous host rock. If the TSST-wave encounters other heterogeneities on its way, the prediction results become less stable. This is the case for the simulated tunnel construction passing the first fault and advancing toward the second interface.

The detection of a major lithological boundary in the Schlüchtern data has been challenging because the TSST arrivals are not even consistently visible in the field data (Figure 5.11a). Also, the TSST-wave form is not uniform in every trace. Future work will include research on additional wave form unification techniques like cross correlation with the source signal in order to improve stacking results and thereby the formation S-wave velocity determination. From both processed field data sets we can conclude that the determination of the apparent TSST-wave and the formation S-wave velocity, respectively, is the crucial and possibly the weak element of the prediction sequence. First, the calculated distances clearly correlate with the obtained S-wave velocity (Figure 5.8a and 5.11b,c). Second, even if the TSST arrival time picks are reasonable, false formation S-wave velocity can prevent the computation of accurate distances. This can happen, if the TSST-wave signals fade with the advancing tunnel face (Figure 5.11a, tunnel face position >310 m). The arrival time picks are still dominated by the strong TSST signals in the window. However, there is no well-defined maximum in the sum of the stacked traces in the reduction velocity range $0 < v_{\mathrm{red}} < v_{\mathrm{max}}$. Eventually, the picked formation S-wave velocity equals v_{max} and has to be rejected. Nevertheless, in the case that the TSST-wave signals fade in again, the prediction method will again lock in the correct distance. If, only a few receiver traces within the window do not exhibit the reflected signal, the prediction processing can compensate for that and continuously map a reflector. Note that the picking of the peak amplitude of the stacked section instead of the first break involves a constant error in the distance estimate. Nevertheless, the introduced error is small and can be traded in for a stable travel time determination.

5.5. Chapter conclusions

Based on the concept of the look-ahead prediction in tunnel construction using tunnel surface waves, we have designed a large synthetic data set. Typical features encountered in a tunnel construction like rock heterogeneities, an excavation damage zone and lithological interfaces have been included in the model to develop and test a robust detection method. The main focus is the automatic prediction of larger structures like faults or lithological boundaries, which can be correlated later with a priori information on the expected geological situation ahead of the tunnel. The prediction sequence basically focuses on the isolation and characterization (apparent velocity, arrival time) of TSST-waves. In both a synthetic and in two field data examples, a sequence of frequency filter, dip-filter, velocity reduction and stacking within a moving window over the tunnel seismic data has shown the capability of determining the reflector distance from the tunnel face. This estimate requires neither intensive processing and computational power, nor any a priori information and can be performed automatically. Future work will focus on the characterization of the reflector and its spatial location with respect to the tunnel axis, e.g., the angle of inclination φ (see Figure 5.2). Since the tunnel look-ahead prediction concept using tunnel surface waves is not limited to either hard rock or soft rock formation (Lüth et al., 2008c), the introduced prediction concept can be applied to most seismic tunnel surveys. Also, with minor modifications, the prediction concept is expected to work for other seismic tunnel look-ahead approaches.

CHAPTER VI

Discussion

At the end of the previous chapters, we already discussed the implications gained through each topic. These preliminary conclusions were focusing on the main chapter content separately. Now we can take a wider view and establish connections between the nature of tunnel surface waves and its application regarding the tunnel look-ahead prediction. We review the properties of TS-wave in relation to Rayleigh wave features, and show the possiblities and limitations of controlling its characteristics. Finally, we interpret the impact on acquired field data.

6.1. Tunnel surface waves vs. Rayleigh surface waves

The propagation of surface waves beneath the earth's surface and behind the wall of a tunnel in the underground differs basically by the scale of the curvature of the surface and whether the wave propagation occurs inside or outside the curvature. We would therefore expect to find general similarities in the wave propagation. First, we briefly recall a few characteristics of earth's surface waves.

Depending on the nature of the source, there can be a predominant excitation of Rayleigh and Love surface waves. In this work, we focused on explosive sources or vertical force sources (normal to the surface), which mainly excite Rayleigh waves. In the following, when using the term surface wave, we merely address the Rayleigh surface wave. By definition, this wave travels at gaseous-solid interfaces at a velocity v_r slightly below the formation S-wave velocity v_s. Usually, the ratio $\frac{v_\mathrm{r}}{v_\mathrm{s}}$ ranges from 0.87 to 0.96 (Ingard, 1988). The disturbance caused by the Rayleigh wave is an elliptical motion, which consists of both a compressional and a shear component. As a result, the affected particles move along an elliptical path normal to the surface. The Rayleigh surface wave penetration depth is limited by the lowest frequency of the excited spectrum. The characteristic penetration depth where the original amplitude at the surface is attenuated to its friction of e^{-1}, is about 40% of the wavelength (Lowrie, 1997). Consequently, decreasing the source frequency results in a larger surface wave penetration depth.

For the frequency and wavelength range realized by geophysical and geotechnical applications, we can approximate the Rayleigh wave propagation along a plane surface. With the increasing wavelength the curvature of the earth influences the wave propagation. (Rulf, 1969; Jin et al., 2005). What might therefore happen if the Rayleigh wave wavelength is large enough to exceed the earth's diameter and circumference, respectively? Is there a maximum Rayleigh wave wavelength?

The waves with the longest wavelength are affiliated to the earth's natural oscillation as an interference of single waves excited by events like earthquakes or volcano eruptions. With both the shear and the compressional component associated to the wave motion, they can be treated as surface waves, too. The longest period of a natural oscillation amounts to 53 minutes and a wavelength of roughly half the earth's circumference (Stacey, 1969). Above a wavelength of about 20.000 km, no waves of any kind have been observed. Since the surface waves are bound to the earth's surface, a longer wavelength would destructively interfere with itself. The corresponding wavelength-to-earth-diameter ratio w_e is $\frac{20.000\ \mathrm{km}}{2\cdot 6371\ \mathrm{km}} \approx 1.6$.

On a much smaller scale, the surface waves propagation along the tunnel wall is limited in a quite similar way. Above a certain wavelength of the excited wave field, there are no surfaces-waves that can be observed along the tunnel wall. In contrast to the earth, the tunnel is embedded in an environment with larger dimensions that permits the seismic wave propagation: the surrounding host rock. Hence, if no surface waves are excited due to the wavelength-to-tunnel-size constraints, body waves are, as a substitute to preserve the excited wave energy. If the wavelength is small to sense the tunnel as a free surface, surface waves are generated. Otherwise, body waves with wavelength significantly larger than the tunnel size pass around the tunnel without much interference. In this case, the tunnel is treated as an anomaly rather than a free surface.

Depending on the ratio of the wavelength with respect to the dimensions of the tunnel cross section, we can observe Rayleigh surface waves bound to the tunnel wall as well as body S-waves spreading into the full space. In order to account for these observations, we describe surface waves around a tunnel as *tunnel surface waves* (TS-waves). At small wavelength, i.e., when the wavelength is small in comparison to the tunnel diameter, the TS-waves show properties of typical Rayleigh waves. The particle motion exhibits an elliptical polarization and the propagation velocity measures in the range typical for Rayleigh surface waves. At a long wavelength in comparison to the tunnel diameter, the tunnel surface wave exhibits S-wave characteristics. Its velocity is approaching the formation S-wave velocity and the hodograms of the particle motion show an almost linear polarization normal to the tunnel wall.

To give a quantitative measure, we introduced the wavelength-to-tunnel-diameter ratio w. This measure takes the given tunnel diameter, the formation properties as well as the resulting TS-wave wavelength with respect to the source center frequency f_c into account. We further propose the wavelength-to-tunnel-diameter ratio range $0.6 < w < 1.2$. Below $w < 0.6$, the excited waves show significant Rayleigh wave characteristics. In the case of $w > 1.2$, mainly S-waves are propagating along the tunnel. The limiting ratio w for the excitation of pure S-waves happens to be about 1.5 (compare to Figure 4.3), which is close to $w_\mathrm{e} \approx 1.6$ being the constraint for the surface wave along the earth's surface. In between $0.6 < w < 1.2$, the tunnel surface waves show a mixture of S-wave and Rayleigh wave properties. For reasons described in Chapter 2, we aim to excite TS-waves with mainly Rayleigh wave properties. Vice versa, for a given tunnel and measurement geometry, we can account for the w-dependency of the TS-wave velocity for the correct imaging of geological inhomogeneities ahead of the tunnel. Otherwise, we introduce additional errors in the estimate of the position of such structures.

6.2. Controlling of the tunnel surface wave properties

Since the diameter of a tunneling site is generally determined by its purpose, there is only the excitation frequency left to change w and consequently influences the TS-wave characteristics. Nevertheless, this applies only to an almost homogeneous host rock or formation properties that increase steadily away from the tunnel wall. We have shown that tunnel surface waves behave dispersive even in a homogeneous medium (we call it *tunnel related dispersion*), which marks the transition in properties from Rayleigh surface waves to S-waves. A gradient in the formation properties due to, e.g., an excavation damage zone enhances this dispersion effect by adding *medium related dispersion*. By designing the source center frequency f_c to the point of desired TS-wave properties, we can control its excitation and propagation behavior.

This fact has to be considered when investigating the tunnel surface wave propagation in soft rocks and hard rocks. With a given tunnel and measurement geometry as well as parameters, we can observe TS-waves traveling in soft rock environments. Keeping all parameters - especially f_c and the Poisson‘s ratio $\nu = \frac{v_\mathrm{p}}{v_\mathrm{s}}$ - constant, we can still fail to excite the same amount of tunnel surface wave energy in hard rock tunnels because of a longer TS-wave wavelength and thus a higher ratio w. In order to balance for the increase in the seismic formation properties (TS-wave velocity and wavelength), we have to increase the source center frequency in the same manner. Current seismic sources can meet their limits here. To give a reference value of the minimum source frequency f_min to excite TS-waves with Rayleigh wave properties, we can rewrite Equation 4.1 under the consideration of $w < 0.6$ to

$$f_\mathrm{min} > \frac{v_\mathrm{ts}}{2\,r\,w}\ . \tag{6.1}$$

With $v_\mathrm{ts} \approx 0.94 \cdot v_\mathrm{s}$ and the shear velocities v_s from Table 2.1, we can derive $f_\mathrm{min-soft} > 120$ Hz and $f_\mathrm{min-hard} > 450$ Hz as a recommended value for tunnel with a diameter of 10 m embedded in a homogeneous soft rock and hard rock formation, respectively. Note that the source center frequency f_c necessary for the excitation of a frequency spectrum with a lower limit f_min is usually a multiple of f_min.

In contrast, a discontinuous increase in the elastic properties away from the source point strongly limits any influence of f_c. In the presence of a high velocity layer (e.g., concrete tubing and mortar backfilling) followed by a drop and a gradual increase in the formation velocities (caused by, e.g., the EDZ), the system response narrows the excited frequency band to low frequencies only. Increasing the source center frequency does not change the system response but excites surface waves propagating within the lining, which may never couple into the rock formation. The lining of the tunnel wall and applying the source and receiver on top of the tubing segment ultimately results in the excitation of mainly S-waves. Only a small friction of the wave energy propagates as TS-waves along the tunnel wall. In this case, we can still utilize S-waves for the prediction of the geology but corrupt the advantages of high energy TS-waves.

6.3. Prediction with tunnel surfaces waves

The wave simulation regardless of the method is as a valuable tool to investigate single aspects of the propagation of TS-waves. In Chapter 3, we have described modeling tools and their capability of reproducing considerably realistic tunnel surface wave effects. Using the 3-D finite difference time domain (FDTD) method on a large CPU cluster, we can even model a comprehensive tunnel seismic survey under various formation properties. At discrete positions of the tunnel face, which is moving toward a defined geological structure, we can simulate a wave field excited by a source applied to the tunnel wall. We record the reflected wave field along arbitrary receiver lines. The number of receivers are basically limited by only the number of grid points of our model. We can therefore add numerous receiver positions and later extract single receiver positions to test different measurement layouts.

For a hard rock tunnel model with the dimensions of 200×108×108 m ($x \times y \times z$), we created such a synthetic tunnel data set. Small- and large-scale fluctuations in the seismic properties account for rock inhomogeneities. A radial gradient in the formation properties off the tunnel wall simulates the excavation damage zone. A wedge of lowered rock properties ahead of the first tunnel face position can be treated as a fault zone with two planar lithological changes. Along the virtual tunnel trajectory, we simulated 56 tunnel face and shot positions. The source-to-tunnel face distance is thus constant. The center frequency of a point force source is chosen to excite high energy TS-waves. The seismogram output is recorded by more than 20 receiver lines with varying depth and azimuthal position around the tunnel wall. Therefore, this synthetic tunnel data set can be of various use and is not limited to the seismic look-ahead prediction. By choosing different receivers from different lines per shot, we can perform a seismic tomography of the EDZ and inhomogeneities around the tunnel. Also, the receiver and shot point density is sufficient to apply seismic migration algorithms in future work.

In Chapter 5, we separated only a single receiver and its seismic model response from each wave simulation. On the basis of this synthetic subset of tunnel data we developed and tested an automatic prediction method of geological structures ahead of the tunnel face under hard rock conditions. If we can predict the location of a fault ahead of the tunnel face from a single receiver per shot, we can be optimistic to locate such a structure in real data with more available receivers, too. As a first step toward an automatic imaging technique of the geology ahead of the tunnel, we intend to reliably and automatically determine the distance of a fault from the tunnel face without any a priori information. We developed a simple processing scheme including the following main items:

- from the automatic picking of the time difference of direct and reflected TS-wave, we can calculate the tunnel surface wave velocity along the tunnel wall,
- by cross correlation we can correct for the TS-wave dispersion (e.g., medium and tunnel related dispersion),
- a velocity reduction routine together with a stacking of single traces can determine the apparent S-wave velocity ahead of the tunnel and enhance the dominant reflection signal,
- after the determination of the velocities above and the picking of the dominant reflection, we calculate the distance between the reflector and the tunnel face,
- by looping over a moving window of the tunnel data and thus covering a certain range of the tunneling process, we obtain a series of tunnel-face-to-reflector distances. After an initial phase of data collecting, we get an update of the estimated fault distance for every new shot,
- in the presence of a geological structure with a significant contrast in seismic properties, the calculated distances decrease linearly with the increase in the absolute position of the tunnel face.

By the help of this robust processing sequence, we can estimate the distance to a plane interface ahead of the tunnel. All necessary parameters are automatically extracted from the field data without any human input. After slight modification to the method, this has been successfully shown for two field data examples acquired in the *Piora adit*, close to the Gotthard base tunnel, Switzerland, and during the construction of the *Neuer Schlüchterner Tunnel*, a railroad tunnel close to Fulda, Germany. However, we cannot yet classify the kind of reflector nor can we describe the exact spatial location within a 3-D volume. Besides, we automatically calculate a reflector distance for every window of the tunnel data. We therefore assume the permanent presence of a reflector oriented normal to the tunnel axis. In case of a dipping reflector ahead, the algorithm corrects for that and can output inaccurate distances. While approaching the reflector, the geometrical influence of the dipping on the velocity determination decreases and the estimated distances converge to the true values. In fact, previous modeling studies suggest that we can use this convergence to reconstruct the reflector orientation. If there is no structure with a distinct seismic contrast ahead, the algorithm interprets the strongest coherent noise signal in the data as a reflector. Nevertheless, distances from noise signals scatter with the moving window and do not line up to indicate a stable reflector. This has been confirmed by applying the prediction sequence to a subset of field data acquired during the construction of the headrace tunnel for the *Glendoe hydro scheme*, Scotland. During the tunneling, no major geological structure has been encountered (Lüth et al., 2008c). Future research will deal with defining rules of how and when to automatically sort out determined distances that are not associated with reflectors ahead of the tunnel.

Considering both the theoretical investigations on the characteristics of the tunnel surface wave and the tunnel seismic data from surveys mentioned above, we must conclude that we could not yet demonstrate the full potential of the presented prediction method using TS-waves. The Piora field data lack of real tunneling conditions. The measurements were taken after the tunnel has been drilled. Thus, no TBM noise superimposes on the seismic recordings. Furthermore, the measurement layout comprising of fixed receivers and pneumatic hammer blows with various offsets does not represent the actual geometry of a tunneling survey.

In contrast, the seismic measurements taken parallel to the construction of the Neuer Schlüchterner Tunnel show all characteristics of a representative run. Nevertheless, the tunnel has been drilled through a soft rock in closed mode, i.e., the tunnel wall has been stabilized by tubing segments. The excited frequency range is thus very low (see Chapter 5.3) and prevent high energy TS-waves with mainly Rayleigh wave properties. From the actual excited source frequency range $0 < f < 150$ Hz and the considerations in Chapter 4.1, we can assume that we mainly excite S-waves. It is still fortunate that we can use the introduced processing scheme and S-waves instead of TS-waves for the seismic prediction ahead of the tunnel face, too. Nevertheless, reflections from geological interfaces in the Schlüchtern data are rare, even though reflectors have been encountered during the tunneling and mapped by a geological survey. This might be due to the bad coupling of the source and/or the receivers as well as the missing high energy tunnel surface waves.

Finally, geological mappings taken at the surface indicated a fault zone striking the Glendoe tunnel trajectory trough metamorphic hard rock. This fault zone has not been encountered underground, which proofs the necessity of an in-situ prediction method parallel to the tunneling. Unfortunately, this also means that no significant reflection signals from a major structure has been recorded in this survey to test the prediction using tunnel surface waves.

CHAPTER VII

Summary and outlook

A new seismic prediction approach has been presented using tunnel surface waves (TS-waves) and its converted and reflected waves (TSST-waves) to detect and image geological heterogeneities, e.g., faults, fractures and lithological interfaces. In order to optimize and correctly interpret the reflection signals, we have studied the basic characteristics of TS-waves by means of an analytical solution, modeling results and seismic tunnel data. Generally, the propagation of tunnel surface waves and Rayleigh surface surface is similar but depends on a proposed wavelength-to-tunnel-diameter ratio range $0.6 < w < 1.2$. In fact, for a certain wavelength range with respect to the tunnel diameter ($w < 0.6$), TS-wave behave exactly like Rayleigh waves. However, a significant decrease in the source frequency and thus an increase in the TS-wavelength ($w > 1.2$) results in the excitation of TS-waves with S-wave properties or pure S-waves, respectively.

We have further investigated the propagation of TS-waves along the tunnel wall in the presence of various tunnel related effects such as the excavation damage zone (EDZ). As the TSST-wave prediction is not limited to hard or softrock formation, we have to consider for the resulting wavelength to control the TS-wave behavior. Nevertheless, the lining of the tunnel wall with a concrete tubing narrows the excited frequency spectrum and thus prevents a high energy TS-wave excitation. Future work will include the research on alternative seismic source (e.g., vibrator sources) or new measurements geometries to overcome the low pass filter effect of the tubing.

The availability of tunnel seismic data and tunnel construction sites to acquire new data, respectively, are very limited. Hence, the full potential of predicting the geology ahead of the tunnel using TS-waves has not yet been shown in field data. We therefore strive to conduct a new seismic tunneling survey predominantly in a hard rock environment. We also plan to turn toward other field data that has not been sufficiently investigated in this work. Even though no major faults where encountered during the construction of the headrace tunnel for the Glendoe hydro scheme, Scotland, internal reflections from formation inhomogeneities were recorded. This field data set can be the basis for further analysis.

Based on the theoretical considerations on the nature of the TS-wave, we have developed a simple and robust processing scheme to interpret the TSST-wave reflections. The tunnel face-to-reflector distance is automatically estimated without any a priori information. Further improvements with regard to the interpretation will deal with the extraction of additional information on the spatial location and the kind of the reflector ahead of the tunnel face. Conducted modeling studies indicate a simple relation of the TS-wave polarization with the inclination of the reflector. Besides, we will also test alternative interpretation approaches. Among others, the full wave form inversion promises to reconstruct the true velocity model from the full recorded wave field of all receiver along the tunnel wall.

Bibliography

Aki, K. and P. Richards, (1980), Quantitative seismology, Theory and Methods, volume **1**: W.H. Freeman and Company.

Alford, R., K. Kelly, and D. Boore, (1974), Accuracy of finite-difference modeling of the acoustic wave equation: Geophysics, **39**, 834–842.

Ashida, Y., (2001), Seismic imaging ahead of a tunnel face with three-component geophones: International Journal of Mining Sciences, **38**, 823–831.

Blanch, J., J. Robertsson, and W. Symes, (1995), Modeling of a constant Q: Methodology and algorithm for an efficient and optimally inexpensive viscoelastic technique: Geophysics, **60**, 176–184.

Blümling, P., C. Cosma, and C. Gelbke, (1992), Prediction ahead of the tunnel face using geophysical methods: Swiss National Coop. for Storage of Radioactive Waste (NAGRA), Technical report NTB, 90–104.

Bohlen, T., (2002), Parallel 3-D viscoelastic finite-difference seismic modelling: Computers & Geosciences, **28**, 887–899.

Bohlen, T., R. Giese, C. Müller, and F. Landerer, (2003), Modeling of seismic waves around a tunnel with irregular wall: Presented at the 65th EAGE Conference & Exhibition, Stavanger, Norway, poster 242.

Bohlen, T., U. Lorang, W. Rabbel, G. Müller, R. Giese, S. Lüth, and S. Jetschny, (2007), Rayleigh-to-shear wave conversion at the tunnel face - from 3D-FD modeling to ahead-of-drill exploration: Geophysics, **72**, T67–T79.

Bohlen, T. and E. Saenger, (2006), Accuracy of heterogeneous staggered-grid finite-difference modeling of Rayleigh waves: Geophysics, **71**, T109–T115.

Borm, G., R. Giese, C. Klose, S. Mielitz, P. Otto, and T. Bohlen, (2003a), ISIS - integrated seismic imaging system for the geological prediciton ahead in underground construction: Presented at the 65th EAGE Conference & Exhibition, Stavanger, Norway.

Borm, G., R. Giese, P. Otto, F. Amberg, and T. Dickmann, (2003b), Integrated seismic imaging system for geological prediciton during tunnel construction. ISRM 2003 - Technology roadmap for rock mechanics, South African Institute of Mining and Metallurgy.

Bösch, H. J., (1998), Developments in conventional tunneling: Presented at the 5th International Symposium on Tunnel Construction, Munich.

Brückl, E., W. Chwatal, S. Mertl, and A. Radinger, (2008), Exploration Ahead of a Tunnel Face by TSWD - Tunnel Seismic While Drilling: Geomechanik und Tunnelbau, **5**, 460–465.

Curry, A., (2009), Archive collapse - disaster for historians, Spiegel online, www.spiegel.de/international/germany/0,1518,611311,00.html, viewed 17.06.2009.

de la Puente, J., M. Dumbser, M. Käser, and H. Igel, (2008), Discontinuous Galerkin Methods for Wave Propagation in Poroelastic Media: Geophysics, **73**, T77–T97.

De Nil, D., T. Bohlen, S. Jetschny, and D. Köhn, (2009), Seismic prediction ahead of tunnel construction sites using tunnel surface waves: Presented at the 69th annual DGG conference, Kiel, Germany.

Dickmann, T., (2005), Seismic prediction while tunneling in hard rock: Sonderband I/2005, DGG Kolloquium, Geophysik zur Vorerkundung von Tunneln (geophysics for the prediction ahead of the tunnel), **1**, 59 – 70.

Dickmann, T. and B. Sander, (1996), Drivage concurrent tunnel seismic prediction: Felsbau, **14**, 406 – 411.

Dougherty, M. and R. Stephen, (1988), Seismic energy partitioning and scattering in laterally heterogeneous ocean crust: Pure Applied Geophysics, **128**, 195 – 239.

Forbriger, T., (2003), Inversion of shallow-seismic wavefields: I. Wavefield transformation: Geophysical Journal International, **153**, 719–734.

Gehrig, M., A. Kassel, and P. Schütz, (2008), Seismic Pre-Exploration during Driving of Leipzig City Tunnel: Tunnel, **4**, 80–87.

Giese, R., C. Klose, and G. Borm, (2005), In situ seismic investigations of fault zones in the Leventina Gneiss Complex of the Swiss Central Alps: Geological Society Special Publication, **240**, 15–24.

Girmscheid, G., (2000), Baubetrieb und Bauverfahren im Tunnelbau: Verlag Ernst & Sohn.

Girmscheid, G. and C. Schexnayder, (2003), Tunnel Boring Machines: Practice Periodical on Structural Design and Construction, **8**, 150–163.

Gopalakrishnan, S., A. Chakraborty, and D. Roy Mahapatra, (2008), Spectral finite element method: Springer Verlag.

Harris, W., (2009), Tunnel Construction: Soft Ground and Hard Rock, www.howstuffworks.com/tunnel3.htm, viewed 12.06.2009.

Herrenknecht, M., (2003a), Hard Rock TBMs: Presented at the Soft Ground and Hard Rock Mechanical Tunneling Technology Seminar, Colorado School of Mines.

———, (2003b), Soft Ground TBMs - Earth Pressure Balance (EPB) Machines: Presented at the Soft Ground and Hard Rock Mechanical Tunneling Technology Seminar, Colorado School of Mines.

———, (2003c), Soft Ground TBMs - Slurry Shields: Presented at the Soft Ground and Hard Rock Mechanical Tunneling Technology Seminar, Colorado School of Mines.

Hiroshi, I. and Y. Naomitsu, (2004), System for Geological Prediction beyond a Tunnel Face for TBM Excavation by GPR-Electromagnetic Eye Looking through the Rock: Report of Taise Technology Center, 1–29.

Hustrulid, W. A., (1999), Blasting principles for open pit mining: Taylor & Francis.

Hutchinson, J., (1979), Fractals and Self Similarity: Indiana University Mathematics Journal, **30**, 713–747.

Inazaki, T., H. Isahai, S. Kawamura, T. Kuruhashi, and H. Hayashi, (1999), Stepwise application of horizontal seismic profiling for tunnel prediction ahead of the face: The Leading Edge, **18**, 1429–1431.

Ingard, K., (1988), Fundamentals of waves and oscillations: Cambridge University Press.

Jetschny, S., D. De Nil, and T. Bohlen, (2010), On the propagation characteristics of tunnel surface-waves for seismic prediction: Geophysical Prospecting, **2**, 245–256.

Jin, F., Z. Wang, and K. Kishimoto, (2005), Basic properties of Rayleigh surface wave propagation along curved surfaces: International Journal of Engineering Science, **43**, 250 – 261.

Junge, M., J. Qu, and L. Jacobs, (2006), Relationship between Rayleigh wave polarization and state of stress: Ultrasonics, **44**, 233–237.

Kneib, G., A. Kassel, and K. Lorenz, (2000), Automated seismic prediction ahead of the tunnel boring machine: First Break, **18**, 295 – 302.

Kolymbas, D., (1998), Geotechnik - Tunnelbau und Tunnelmechanik: Eine systematische Einführung mit besonderer Berücksichtigung mechanischer Probleme (Geotechnics - tunneling and tunnel mechanics: a methodical introduction with special consideration of mechanical problems): Springer Verlag.

Lamprecht, L., (2010), Simulation seismischer Wellen mit der Spektralen-Finite-Elemente-Methode in der Umgebung eines Tunnels (simulation of seismic waves around a tunnel using the spectral finite element method): Presented at the 70th annual DGG conference, Bochum, Germany.

Lowrie, W., (1997), Fudamentals of Geophysics: Cambridge University Press.

Lüth, S., S. Buske, R. Giese, and A. Goertz, (2005), Fresnel volume migration of multicomponent data: Geophysics, **70**, 121–129.

Lüth, S., R. Giese, P. Otto, K. Krüger, S. Mielitz, T. Bohlen, and T. Dickmann, (2006), Seismic investigation of the Piora Basin using S-wave conversions at the tunnel face of the Piora adit (Gotthard Base Tunnel): International Journal of Mining Sciences, **45**, 86–93.

Lüth, S., R. Giese, and A. Rechlin, (2008a), A seismic exploration system around and ahead of tunnel excavation - OnSITE: Presented at the World Tunnel Congress, 34th Ita-Aites General Assembly, Agra, India.

Lüth, S., A. Rechlin, R. Giese, R. Besser, and E. Fecker, (2008b), OnSITE - Tunnelseismik I: Seismische Vorauserkundung im Tunnelbau mit Lockergestein - Neuer Schlüchterner Tunnel (Hessen) (OnSITE - tunnel seismics I: seismic tunnel look-ahead prediction in soft rocks): Presented at the 68th annual DGG conference, Freiberg, Germany.

Lüth, S., A. J. Rechlin, R. Giese, J. Tzavaras, K. Gross, S. Buske, S. Jetschny, D. De Nil, and T. Bohlen, (2008c), Seismic prediction ahead of a tunnel face - Modeling, field surveys, geotechnical interpretation: International Journal of the Japanese Commitee for Rock Mechanics, **4**, 47–51.

Malmgreen, L., D. Saiang, J. Töyrä, and A. Bodare, (2007), The excavation disturbed zone (EDZ) at Kiirunavaara mine, Sweden - by seismic measurement: Journal of Applied Physics, **61**, 1–15.

Patera, A., (1984), A spectral element method for fluid dynamics - laminar flow in a channel expansion: Journal of Computational Physics, **54**, 468–488.

Petronio, L. and F. Poletto, (2002), Seismic-while-drilling by using tunnel boring machine noise: Geophysics, **67**, 1798–1809.

Qiu, J., B. C. Khoo, and C. W. Shu, (2006), A numerical study for the performance of the Runge-Kutta discontinuous Galerkin method based on different numerical fluxes: Journal of Computational Physics, **212**, 540–565.

Randall, C., (1991), Multipole acoustic waveforms in nonaxissymmetric boreholes and formations: J. Acoust. Soc. Am., **90**, 1620–1631.

Reed, W. and T. Hill, (1973), Triangular mesh methods for the neutron transport equation: Technical Report LA-UR-73-479, Los Alamos Scientific Laboratory, Los Alamos,.

Robertsson, J., J. Blanch, and W. Symes, (1994), Viscoelastic finite-difference modeling: Geophysics, **59**, 1444–1456.

Rogers, D., (2009), Gotta get through it: Halcrow builds the UAE's longest tunnel, www.building.co.uk/story.asp?sectioncode=583&storycode=3139636&c=0, viewed 21.07.2009.

Rosenblad, A., E. Rathje, and K. Stokoe II, (2006), Shear wave velocity profiling by the

SASW method at selected strong-motion stations in Turkey: Final Report for the Pacific Earthquake Engineering Research Center Lifelines Program.

Rulf, B., (1969), Rayleigh waves on curved surfaces: Journal of the Acoustical Society of America, **45**, 493–499.

Schuster, K., H. Alheid, and D. Boddener, (2001), Seismic investigation of the excavation damaged zone in opalinus clay: Engineering Geology, **61**, 189–197.

Sheriff, K. and L. Geldart, (1983), Exploration seismology: Cambridge University Press.

Singh, B. and R. K. Goel, (2006), Tunneling in weak rock, volume **5**: Elsevier Geo-Engineering Book Series.

Sommerfeld, A., (1947), Vorlesungen über theoretische Physik, Bd. II (lectures on theoretical physics, vol. II): Verlag Harri Deutsch.

Stacey, F., (1969), Physics of the Earth: John Wiley and Sons.

Stielke, G., (1959), Über seismische Oberflächenwellen an einem Hohlzylinder im Vollraum (on seismic surface waves around a hollow cylinder in a full space): PhD thesis, Technical University, Clausthal.

Virieux, J., (1986), P-SV wave propagation in heterogeneous media: velocity-stress finite-difference method: Geophysics, **51**, 889–901.

Wang, R., (1999), A simple orthonormalization method for stable and efficient computations of green's functions: Bulletin of the Seismological Society of America, **89**, 733–741.

Wijk, K., (2003), Multiple scattering of surface waves: Ph.D. thesis, Center for Wave Phenomena, Colorado School of Mines, Colorado.

Wu, R. and K. Aki, (1988), Introduction: Seismic Wave Scattering in Three-dimensionally Heterogenous Earth: Geophysics, **128**, 1–6.

www.bls.ch, (2009), Das Bauwerk: Der Bahntunnel - Vortrieb (the building: railroad tunnel - driving), www.bls.ch/d/infrastruktur/neat-bauwerk-bahntunnel.php, viewed 21.07.2009.

www.oyogeospace.com, (2009), Geospace Technologies, Specifications of the GS-14-L3 geophone, http://www.oyogeospace.com/technologies/index.php?id=211, viewed 21.07.2009.

www.pitsch.ch, (2009), Homepage Andrea Pitsch AG, Untertagebau (underground mining), www.pitsch.ch/bilderuntertagebau.htm, viewed 06.06.2009.

www.welterbe-erhalten.de, (2009), Waldschlösschenbrücke Dresden and the UNESCO World Heritage Title, www.welterbe-erhalten.de, viewed 16.06.2009.

Yang, L., Z. Qinghong, B. Leiying, and W. Xiucheng, (2007), Pure S-waves in land P-wave source VSP data: Journal of Applied Geophysics, **4**, 173–182.

APPENDIX A

Appendix

Starting with the vector field in cylindrical coordinates and considering the boundary conditions for waves along plane interfaces, we obtain the Bessel differential equation whose solutions are cylinder functions. A common solution includes *Hankel functions* of order n. The tunnel wall is a free surface and necessarily stress free. Therefore, some elements of the stress tensor are zero. The remaining elements are calculated from the displacement tensor. Combining cylinder functions and the derivation of the displacement tensor for cylindrical coordinates (Sommerfeld, 1947) leads to the equations for calculating the dispersion and the oscillation vector. They are listed in the following (equations A1) - (A3) (taken from Stielke, 1959).

Calculation of phase velocity of tunnel surface waves proceeds by solving the following equation for varying w:

$$\begin{aligned}
0 =\,& p^4 \left[4\,F^2\,E\,h_{\mathrm{n},1} - G^2\,F\,h_{\mathrm{n},2}\right] \\
&+ p^3 \left[2\,(4+\xi_2)\,E\,h_{\mathrm{n},1}\,F\,h_{\mathrm{n},2} - 2\,G^2\,h_{\mathrm{n},2}^2 - n\,\xi_2^2\right] \\
&+ 2\,p^2 \left[n\,(\xi_2 + 4\,n + 4)\;E\,h_{\mathrm{n},1} - 2\,n\,(n+1)\;G\,F\,h_{\mathrm{n},2}\right] \\
&+ 2\,p^2 \left[-n\,\xi_2\,\frac{1+\xi_2}{F}\,h_{\mathrm{n},2} - 2\,\left(n^2-1\right)\,\xi_2\,E\,h_{\mathrm{n},1}\,h_{\mathrm{n},2}^2\right] \\
&+ 4\,n\,(n+1)\,p\,\xi_2 \left[n - 2\,(n-1)\;E\,h_{\mathrm{n},1}\frac{1}{F}\,h_{\mathrm{n},2} - (n-1)\;h_{\mathrm{n},2}^2\right] \\
&+ 4\,n^2\left(n^2-1\right)\left[E\,h_{\mathrm{n},1} - (1+\xi_2)\,\frac{1}{F}\,h_{\mathrm{n},2}\right] \qquad \text{(A1)}
\end{aligned}$$

with

$$\begin{aligned} p &= \frac{2\,\pi\,r}{\lambda} = \frac{\pi}{w}, & w &= \frac{\lambda}{2r} \;\; \text{(equation4.1)} & & \\ E &= \sqrt{1-\xi_1}, & F &= \sqrt{1-\xi_2}, & G &= (2-\xi_2)\,, \\ \xi_1 &= \frac{v_{\mathrm{ts}}^2}{v_{\mathrm{p}}^2}, & \xi_2 &= \frac{v_{\mathrm{ts}}^2}{v_{\mathrm{s}}^2}, & & \\ h_{\mathrm{n},1} &= \frac{i\,H_{n-1}\,(1)}{-H_n\,(1)}, & h_{\mathrm{n},2} &= \frac{i\,H_{n-1}\,(2)}{-H_n\,(2)}, & & \\ H_n\,(1) &= H_n^1\,(k_1\,w)\,, & H_n\,(2) &= H_n^1\,(k_2\,w)\,, & & \\ k_1 &= i\,\pi\sqrt{1-\xi_1}, & k_2 &= i\,\pi\sqrt{1-\xi_2} & & \end{aligned} \tag{A2}$$

and r denotes the tunnel radius, λ the tunnel surface wave wavelength, v_{p} the formation P-wave velocity, v_{s} the formation S-wave velocity, v_{ts} the phase velocity of tunnel surface wave and H_{n} the Hankel function of order n where n describes the order of source excitation. A monopole source (circularly symmetric source) is defined by $n = 0$ and a dipole source by $n = 1$. Note that the nonlinear equation A1 was solved using the function *fsolve* from *Mathworks MATLAB*® (included in the *Optimization Toolbox*). If *fsolve* was not able to find a converging solution, the calculated v_{ts} has been neglected.

The calculation of the amplitude vector A of tunnel surface waves was performed by solving the following equation for varying w:

$$\begin{aligned} A_{\mathrm{r}} =& -\frac{1}{2}\,p^3\,E\,F^2\,\xi_2\,h_{\mathrm{n},1}\,h_{\mathrm{n},2} \\ &+ p^2\,F\,\xi_2\left[E\,h_{\mathrm{n},1}\,h_{\mathrm{n},2}^2 + \frac{1}{2}\,n\,E\,h_{\mathrm{n},1} + \frac{1}{2}\,n\,F\,h_{\mathrm{n},2}\right] \\ &+ n\,p\,\xi_2\left[2\,E\,h_{\mathrm{n},1}\,h_{\mathrm{n},2} + F\,h_{\mathrm{n},2}^2 + \frac{1}{2}\,n\,F\right] \\ &+ n^2\left[(1+\xi_2)\,h_{\mathrm{n},2} - E\,F\,h_{\mathrm{n},1}\right] \\ A_{\phi} =& n\,p^2\,F\left[E\,h_{\mathrm{n},1}\left(\xi_2\,h_{\mathrm{n},2}^2 - 1\right) + \frac{1}{2}\,F\,G\,h_{\mathrm{n},2}\right] \\ &+ n^2\,p\,\xi_2\left[F\,h_{\mathrm{n},2}^2 + 2\,E\,h_{\mathrm{n},1}\,h_{\mathrm{n},2} - \frac{1}{2}\,F\right] \\ &+ n^3\left[(1+\xi_2)\;h_{\mathrm{n},2} - E\,F\,h_{\mathrm{n},1}\right] \\ A_{\mathrm{x}} =& p^3\,F^2\left[\frac{1}{2}\,G\,h_{\mathrm{n},2} - E\,F\,h_{\mathrm{n},1}\right] \\ &+ p^2\,F\left[G\,h_{\mathrm{n},2}^2 - 2\,E\,F\,h_{\mathrm{n},1}\,h_{\mathrm{n},2} + \frac{1}{2}\,n\,\xi_2\right] \\ &+ n\,p\left[\left(n\,F^2+2\right)h_{\mathrm{n},2} - (n+2)\,E\,F\,h_{\mathrm{n},1}\right] \end{aligned} \tag{A3}$$

with p, E, F, G ,ξ_1, ξ_2, $h_{\mathrm{n},1}$, $h_{\mathrm{n},2}$ as defined above. A_{r}, A_{ϕ} and A_{x} denote the radial, azimuthal and the longitudinal components of the excitation amplitude (Figure 2.1).

Acknowledgment \ Danksagung

Kommen wir nun zum wohl schwierigsten, weil wohl auch meist gelesensten Kapitel dieser Arbeit. Den grössten Dank verdienen hier wohl meine lieben Eltern, Friederike und Wolfgang, meine Schwester Andrea und meine lieben Großeltern Ida & Heinz und Gertraut & Wenzel. Ihr habt mich in meinem bisherigen Leben und während des Studiums am längsten und intensivsten betreut! Eure aufmunternde Worte, kritische Fragen, offene Ohren, aber vor allem immer wieder eure Unterstützung in allen Lebenslagen und das Interesse an meiner Arbeit haben dazu beigetragen, dass ich jetzt soweit bin, diese Arbeit abzugeben. Stolz kann ich sagen, dass diese Arbeit genauso eure ist!

In den letzten, schönen Jahren hat sich die liebevolle Unterstützung meiner Freundin Anja dazu gesellt. Oft genug warst du der Grund, dass ich nicht auf Arbeit wollte, immer aber warst du der Anlass weiterzumachen, auch wenn numerische Instabilitäten den Tag grau erschienen ließen. Vielen Dank Anja, für deine Geduld zu Verstehen was ich eigentlich gerade mache, dein Lachen immer zur rechten Zeit und deine Liebe, die mich bisher begleitet hat.

Fast acht Jahre lang haben mich meine lieben Kollegen in Freiberg am Institut für Geophysik in wissenschaftlicher und auch sehr persönlicher Weise geprägt. Sicher, ich habe hin und wieder ein Kopfschütteln provoziert, wenn ich z.B. neue physikalische Größen wie die scheinbare Leitfähigkeit erfand. Ich dank euch - Antje, Klaus, Ralph-Uwe, Rolf, Christoph, Udo, Tino B. - daher für euren geduldigen Umgang mit mir und für euer Wissen um die Geophysik, das ihr mir während meines Studiums vermittelt habt! Besondere Erwähnung soll hier vor allem unsere gute Seele der Etage, Annett ("Holli"), finden. Oft genug in ihrer Arbeit für das Institut unterschätzt, hat sie mich mit Kaffee, Keksen und Gummibärchen während des Studiums vor dem Verhungern gerettet. Viel wichtiger aber ist, dass ich weiß, dass es einen Ort gibt wo ich auch nach Jahren immer ein herzliches Gespräche finden werde! Danke auch euch Maja, Tino M. und Holger für eure Geselligkeit, auch wenn ihr sicher Schuld tragt, dass ich nicht schon ein bisschen eher abgegeben habe. Auf keinen Fall aber möchte ich diese Zeit missen!

Projektseitig danke ich natürlich auch dem BMBF, der DFG, dem Programm GEOTECHNOLOGIEN und insbesondere den Personen, die schließlich den "genehmigt"-Stempel unter den OnSITE Projektantrag gedrückt haben. Noch wichtiger ist mir aber die Erwähnung meiner Kollegen vom GFZ Potsdam: Aissa, Rudi und Stefan. Die drei-jährige Projektlaufzeit und die Zusammenarbeit mit euch haben mir Spass gemacht! Auch wenn ihr immer viel zu tun hattet, eine Antwort auf alle Untertageprobleme dieser Welt war gewiss. Ohne euch würde ich sicher immer noch über die Orientierung der 3-C Geophone grübeln.

Gleich in diesem Zusammenhang möchte ich dir, Thomas, danken, dass du mir direkt nach dem Diplom die Chance gegeben hast, meine wissenschaftliche Tauglichkeit zu zeigen bzw. zu entwickeln. Neben der rein fachlichen Betreuung, empfand ich es immer als sehr angenehm, eine

offene Tür inklusive Ohr für all die kleinen und großen Tunneloberflächenwellenprobleme zu haben. Auch zu kleine Plaudereien warst du immer bereit. Diese Offenheit und der menschliche Umgang, der weit über das übliche Chef-Student-Verhältnis hinausgeht, habe ich zu schätzen gelernt.

Die halbwegs rechtzeitige Fertigstellung dieser Arbeit habe ich Bob zu verdanken, der mir für ein Jahr die Chance ermöglicht hat, meinen Schreibtisch in den schönen Evergreen-Sate zu verschieben. Dort hatte ich nicht nur die Gelegenheit den wohl weltbesten Moccha zu trinken, sondern auch die nötige Zeit und Ruhe, all das zu Papier zu bringen, was sich in den letzten Jahren angehäuft hatte. Danke auch an Tina, Ken, Tim, Keith, Larry, Andy, Jie und Ines, die dazu beigetragen habe, dieses Jahr unvergesslich zu machen!

Nicht unterschlagen werden sollen natürlich auch die tapferen Korrekturleser (wenn sie nicht schon bisher hier erwähnt wurden), die sich in den letzten Monaten durch die Arbeit gelesen, viele nützliche Verbesserungen angemahnt und mich daher mit halbwegs gutem Gewissen meine Arbeit abgeben lassen haben. Danke Steffi, André und Olaf. Mit euch und natürlich Stefan und Jörg verbinde ich zudem viele schöne Erinnerungen an die Zeit in Freiberg, danke für Wein und Spiele! Vielen Dank auch an meinen Zweitbetreuer Wolfgang Rabbel, der sich so ganz unkompliziert und spontan der Begutachtung meiner Arbeit angenommen hat.

Zum Schluss, aber nicht weniger herzlich danke ich meinen "neuen" Karlsruher Kollegen am Geophysikalischen Institut, allen voran Ines, Lisa und Anna, die mir nun einen Hut basteln müssen, obwohl ich erst seit kurzem hier bin. Ich weiß, ihr macht es dennoch gern und das finde ich toll! Danke auch an Petra, Claudia und Jürgen für all die kleinen, zum Teil so "unsichtbaren" Handgriffe, die meinen wissenschaftliche Umsiedlung und die Fertigstellung meiner Arbeit erleichtert haben.